

Resolving the chemical substructure of Orion-KL [★]

S. Feng¹, H. Beuther¹, Th. Henning¹, D. Semenov¹, Aina. Palau², E. A. C. Mills³

1. Max-Planck-Institut für Astronomie, Königstuhl 17, D-69117, Heidelberg, Germany. syfeng@mpia.de

2. Centro de Radioastronomía y Astrofísica, Universidad Nacional Autónoma de México, Morelia Michoacan, Mexico

3. National Radio Astronomy Observatory, 1003 Lopezville Road, Socorro, NM 87801

December 3, 2024

ABSTRACT

Context. The Kleinmann-Low nebula in Orion (Orion-KL) is the nearest example of a high-mass star-forming environment. Studying the resolved chemical substructures of this complex region provides important insight into the chemistry of high-mass star-forming regions (HMSFRs), as it relates to their evolutionary states.

Aims. The goal of this work is to resolve the molecular line emission from individual substructures of Orion-KL at high spectral and spatial resolution and to infer the chemical properties of the associated gas.

Methods. We present a line survey of Orion-KL obtained from combined Submillimeter Array (SMA) interferometric and IRAM 30 m single-dish observations. Covering a 4 GHz bandwidth in total, this survey contains over 160 emission lines from 20 species (25 isotopologues), including 11 complex organic molecules (COMs). Spectra are extracted from individual substructures and the intensity-integrated distribution map for each species is provided. We then estimate the rotation temperature for each substructure, along with their molecular column densities and abundances.

Results. For the first time, we complement 1.3 mm interferometric data with single-dish observations of the Orion-KL region and study small-scale chemical variations in this region. (1) We resolve continuum substructures on $\sim 3''$ angular scale. (2) We identify lines from the low-abundance COMs CH_3COCH_3 and $\text{CH}_3\text{CH}_2\text{OH}$, as well as tentatively detect CH_3CHO and long carbon-chain molecules C_6H and HC_7N . (3) We find that while most COMs are segregated by type, peaking either towards the hot core (e.g., nitrogen-bearing species) or the compact ridge (e.g., oxygen-bearing species like HCOOCH_3 and CH_3OCH_3), the distributions of others do not follow this segregated structure (e.g., $\text{CH}_3\text{CH}_2\text{OH}$, CH_3OH , CH_3COCH_3). (4) We find a second velocity component of HNCO , SO_2 , $^{34}\text{SO}_2$, and SO lines, which may be associated with a strong shock event in the low-velocity outflow. (5) Temperatures and molecular abundances show large gradients between central condensations and the outflow regions, illustrating a transition between hot molecular core and shock-chemistry dominated regimes.

Conclusions. Our observations of spatially resolved abundance variations in Orion-KL provide the nearest reference source for hot molecular core and outflow chemistry, which will be an important example for interpreting the chemistry of more distant HMSFRs.

Key words. Stars: formation; Stars: massive; ISM: lines and bands; ISM: molecules; ISM: abundance; Submillimeter: ISM

1. Introduction

The birth sites of high-mass star-forming regions (HMSFRs) are highly complex structures, consisting of different gas and dust cores, embedded in a less dense gas envelope. While the complexity of dynamic processes within these regions has been characterized well (e.g., Zinnecker & Yorke 2007; Beuther et al. 2007b; Tan et al. 2014), our knowledge of the chemical properties of these regions is still poor. Since specific molecules can act as tracers of physical processes (e.g., Schilke et al. 1997; Charnley et al. 1997; Bachiller et al. 2001; Viti et al. 2004; Garrod 2013), characterizing the chemistry of gas associated with the early stages of high-mass stars is crucial for understanding how these stars might form.

Line surveys of HMSFRs in mm/sub-mm atmospheric windows exhibit rich molecular emission spectra (see Herbst & van Dishoeck 2009 for a comprehensive review). The multitude of detected lines allow for an unbiased look at the chemical composition of a particular region, from which its physical properties can be inferred, including temperature and density. However, HMSFRs are typically distant (several kpc), so that

spatially disentangling the physical and chemical substructures is challenging with the resolution of most facilities. This makes the Becklin-Neugebauer and Kleinmann-Low Nebula in Orion (Orion BN/KL), at a distance of 414 ± 7 pc (Sandstrom et al. 2007; Menten et al. 2007), ideal for studies of the physical and chemical properties of HMSFRs. As the nearest HMSFR, it has been extensively studied at both far-infrared to (sub) millimetre wavelengths accessible from space (e.g., Olofsson et al. 2007; Bergin et al. 2010; Crockett et al. 2014) and at radio, millimetre, and submillimetre wavelengths accessible from the ground. A broad range of studies on this source have been conducted either with single-dish telescopes (e.g., Johansson et al. 1984; Sutton et al. 1985; Blake et al. 1987; Turner 1989; Greaves & White 1991; Schilke et al. 1997, 2001; Lee & Cho 2002; Comito et al. 2005; Remijan et al. 2008; Tercero et al. 2010) or interferometers (e.g., Wright et al. 1996; Blake et al. 1996; Beuther et al. 2005, 2006; Friedel & Snyder 2008; Guélin et al. 2008). Strong emission lines in these observations have revealed complex dynamics (e.g., Sutton et al. 1985; Blake et al. 1987; Turner 1989; Beuther & Nissen 2008; Beuther et al. 2010) and chemistry (e.g., Wright et al. 1996; Blake et al. 1996; Beuther et al. 2005, 2006; Friedel & Snyder 2008; Guélin et al. 2008; Widicus Weaver & Friedel 2012; Friedel & Widicus Weaver

Send offprint requests to: syfeng@mpia.de

2012).

Both single-dish-only and interferometer-only observations, however, have limitations. Single-dish observations have low spatial resolution, making it difficult to detect spatial variations of chemistry on small scales. In contrast, interferometric observations can probe spatial variations on small scales, but suffer from filtering-out to large scale structures (the “missing short spacing” problem; Bajaja & van Albada 1979), making measurements of the chemistry of more extended features unreliable. In this paper, we aim to study the chemistry of Orion-KL by obtaining a combined dataset from an interferometer (Submillimetre Array, SMA) and a single-dish (IRAM 30 m) telescope. These combined data, which resolve small-scale substructures and are sensitive to more extended components, allow us to accurately map the distribution of molecular species, determine their abundances, and ultimately analyse spatial variations in the chemistry.

One unique feature of HMSFRs is hot molecular cores, which are compact objects (≤ 0.05 pc) that exhibit high temperatures (≥ 100 K) and densities ($\geq 10^6$ cm $^{-3}$; Palau et al. 2011). Numerous spectral surveys (see, e.g., Turner 1989; Schilke et al. 2001; Belloche et al. 2009; Herbst & van Dishoeck 2009; Tercero et al. 2010) have revealed that hot molecular cores are characterized by a large abundance of simple organic molecules, including H₂CO (formaldehyde), HCOOH (formic acid), and complex organic molecules (COMs, organics containing ≥ 6 atoms), such as CH₃OH (methanol), HCOOCH₃ (methyl formate), and CH₃OCH₃ (dimethyl ether). Although some larger COMs have low abundances in hot molecular cores, e.g., CH₃CH₂OH (ethanol; Rizzo et al. 2001), CH₃COCH₃ (acetone; Snyder et al. 2002), CH₃CHO (acetaldehyde; Nummelin et al. 2000), (CH₂OH)₂ (ethylene glycol; Hollis et al. 2002), and CH₂OHCHO (glycolaldehyde; Hollis et al. 2000, 2004), they have been previously detected towards the Galactic-centre hot molecular core source SgrB2 (N-LMH). Because of their high degree of chemical and structural complexity, the precise origins and formation mechanisms of these COMs is still a subject of debate. Nevertheless, understanding these topics is particularly important for understanding the chemical evolution of the interstellar medium (ISM; e.g., Herbst & van Dishoeck 2009). Recently, a number of interferometric observations of COMs in Orion-KL (e.g., Friedel et al. 2005; Friedel & Snyder 2008; Guélin et al. 2008; Favre et al. 2011a,b; Widicus Weaver & Friedel 2012) have shown spatial-related chemical differentiation. However, the relatively low sensitivity of these observations means that the lowest-abundance COMs (e.g., CH₂OHCHO, CH₃CH₂OH, and CH₃CHO) are below the 3σ detection limit or are blended by strong neighbouring lines.

In addition to the hot molecular core chemistry, the shock chemistry driven by outflows is another important aspect of chemistry in HMSFRs. The region in Orion-KL that is most affected by outflow and shock events is called the “plateau” (Blake et al. 1987; Wright et al. 1996; Lerate et al. 2008; Esplugues et al. 2013) and is characterized by spectral lines with broad line wings. Two roughly perpendicular outflows are seen in Orion-KL, traced by the proper motion of H₂O masers at 22 GHz (Genzel et al. 1981). One is a high-velocity outflow (30–100 km s $^{-1}$, along the north-west–south-east (NW–SE) axis); this outflow is also detected in OH (hydroxyl) masers (Norris 1984; Cohen et al. 2006), broad bipolar CO line wings (Zuckerman et al. 1976; Kwan & Scoville 1976; Erickson et al.

1982; Masson et al. 1987; Chernin & Wright 1996; Beuther & Nissen 2008; Zapata et al. 2009), and lobes of poorly collimated shock-excited H₂ (Beckwith et al. 1978; Scoville et al. 1982; Taylor et al. 1984; Allen & Burton 1993; Sugai et al. 1994). Although the source responsible for driving the outflow is still uncertain, it has been suggested that the outflow is only about 500–700 years old (Lee & Burton 2000; Doi et al. 2002; Gómez et al. 2005; Nissen et al. 2007; Gómez et al. 2008; Beuther & Nissen 2008; Bally et al. 2011; Goddi et al. 2011b; Nissen et al. 2012). The other is a low-velocity outflow (~ 18 km s $^{-1}$, $\Delta V \sim 35$ km s $^{-1}$, along the north-east–south-west (NE–SW) axis; Genzel et al. 1981; Gaume et al. 1998), which is also detected in SO (Plambeck et al. 1982), SiO masers (Wright & Plambeck 1983; Plambeck et al. 2009; Greenhill et al. 2013) and H₂O maser (Greenhill et al. 2013). This outflow is believed to be closely associated with an expanding gas shell or torus around Source I, but whether its age is > 3000 years (Menten & Reid 1995; Greenhill et al. 1998; Doeleman et al. 1999; Reid et al. 2007) or much younger (Plambeck et al. 2009; Greenhill et al. 2013) is still not clear. Another goal of this study is to look for additional chemical signposts of these outflows, apart from the known masers, in order to better understand their physical and chemical properties.

In this paper, we present the first combined single-dish and interferometric line survey at 1.3 mm towards Orion-KL and study the chemical properties of this region at a linear resolution of ~ 1200 AU (at a distance of ~ 414 pc). In Section 2, we describe the observations and their combination. In Section 3, we present a continuum map and maps of the distribution of different molecules, including simple molecules and COMs, where the presences of COMs are identified by synthetic spectrum fittings. The spatial distributions, column densities, and abundances for all the detected species are derived in Section 4. A discussion of the chemistry in the hot molecular core and outflows of Orion-KL can be found in Section 5.

2. Observations and data reduction

2.1. Submillimetre Array (SMA)

We carried out observations of Orion-KL with the SMA on Feb. 15, 2005 and Feb. 19, 2005. At 1.3 mm (220/230 GHz) in the compact configuration with seven antennas, the baselines ranged between 16 and 69 m. The short baseline cutoff causes source structures $\geq 20''$ to be filtered out. The primary beam is $52''$, and the phase centre of the observations is $\alpha_{2000} = 05^{\text{h}}35^{\text{m}}14.5^{\text{s}}$ and $\delta_{2000} = -5^{\circ}22'30.45''$ with $V_{\text{LSR}} \sim 7$ km s $^{-1}$. Bandpass calibration was done with Callisto, and the flux calibration is estimated to be accurate within 15%, based on the SMA monitoring of quasars. Phase and amplitude calibration was performed via frequent observations of the quasar 0607-157. The zenith opacities, measured with the NRAO tipping radiometer located at the Caltech Submillimetre Observatory, were excellent during both tracks with $\tau(1.3 \text{ mm}) \sim 0.03 - 0.04$, allowing us to observe at both 1.3 mm and $440 \mu\text{m}$ simultaneously (Beuther et al. 2006). More technical descriptions of the SMA and its calibration schemes can be found in Ho et al. (2004). The receiver operated in a double-side band mode with an intermediate frequency of 4–6 GHz so that the upper and lower side bands were separated by 10 GHz. The correlator had a bandwidth of 2 GHz, and the channel separation was 0.8125 MHz, corresponding to a velocity resolution of ~ 1.2 km s $^{-1}$. Double-sided band system temperatures corrected for the atmosphere were be-

tween 150 and 300 K (depending on the elevation of the source).

The initial flagging and calibration was done with the IDL superset MIR, which is originally developed for the Owens Valley Radio Observatory and adapted for the SMA¹. The imaging and data analysis was conducted in MIRIAD (Sault et al. 1995) and CASA². Between the observations on two nights, the frequency setups were shifted by 0.4 GHz, yielding a slightly larger total bandwidth for the combined dataset (218.870 – 221.234 GHz for the lower sideband, and 228.870 – 231.234 GHz for the upper sideband). The synthesised beams of the combined data are $3.49'' \times 2.57''$ for the lower sideband and $3.68'' \times 2.69''$ for the upper sideband.

2.2. Single-dish observations with the IRAM 30 m telescope

In addition to the high spatial resolution data from the SMA, we mapped an area of $1' \times 1'$, with the IRAM 30 m telescope, to complement the short-spacing information missing from the interferometric observations. Observations were performed in the on-the-fly mode on Nov. 30, 2012, covering a broad bandpass (8 GHz bandwidth for each sideband) of EMIR at 220/230 GHz. Observations were conducted under good weather conditions ($T_{\text{sys}} = 266$ K, $\tau \sim 0.152$ at 220 GHz). The focus was on Uranus, and pointing was checked on Uranus and 0420-014. Using a forward efficiency of 92% and a main beam efficiency of 58%, we converted the data from antenna temperature (K) to flux (Jy) by using an efficiency³ of 7.8. The beam of the 30 m telescope at 1.3 mm is $\sim 11.3''$ in the upper sideband and $\sim 11.8''$ in the lower sideband. The observations cover frequencies 213.370–221.150 GHz and 229.051–236.831, with a velocity resolution of 0.255 km s^{-1} . We used the Gildas⁴ software for data reduction, and then converted the 30 m data to the MIRIAD data format.

2.3. Data merging

The 30 m single-dish spectral-line data were first converted to visibilities, and then combined with the SMA data using the MIRIAD package task UVMODEL⁵. To recover large-scale emission, while simultaneously maintaining high spatial resolutions for resolving small scale structure, we chose an intermediate weighting between natural and uniform (“robust” = -0.5 value in MIRIAD). However, as continuum information is not available from the 30 m observations, only the spectral-line data can be corrected in this way.

The combined data have a field of view of $52''$ and a beam of $5.55'' \times 4.35''$ with position angle P.A. = $+8^\circ$ in the lower sideband and $5.44'' \times 4.43''$ with P.A. = $+2^\circ$ in the upper sideband. The frequency overlap between the SMA and 30 m data results in the combined data having a frequency range 218.870–221.150 GHz and 229.051–231.234 GHz. Figure 1 presents an amplitude-versus-projected uv distance plot, showing the good combination of the single-dish and interferometer data. Missing projected baselines shortwards of 10 k λ from the

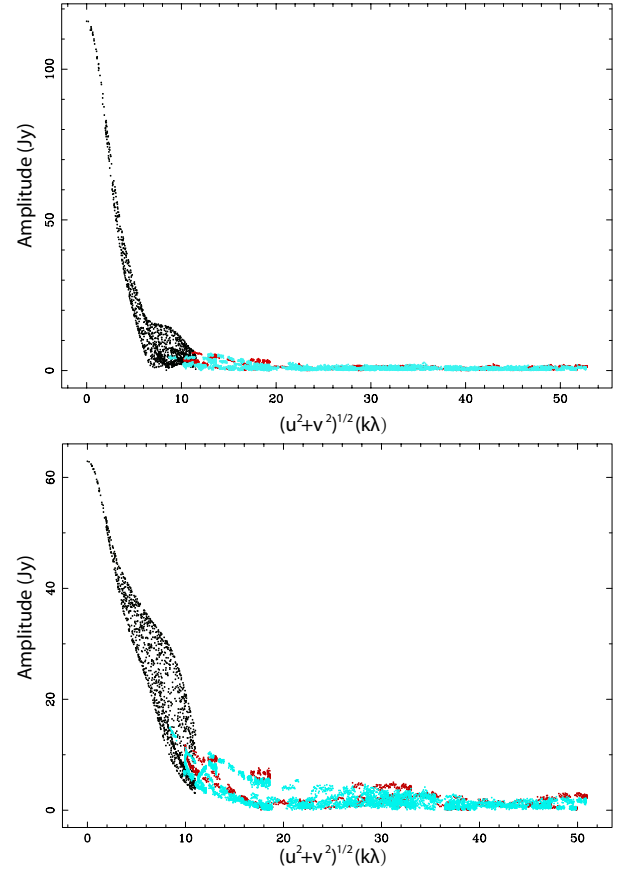


Fig. 1: Amplitude in Jy versus the projected baseline showing the combination of the interferometer and single-dish data, from the upper sideband (top) to lower sideband (bottom). Red and blue dots present data from the SMA on Feb. 15, 2005 and Feb. 19, 2005, respectively, showing the lack of baselines shorter than 10 k λ . Black dots are data converted from 30 m single-dish observations, which fill in the missing short spacing information.

SMA have been complemented by using the 30 m data. After combination, the 1σ rms per 1.2 km s^{-1} channel is measured to be 80 mJy beam^{-1} for the lower sideband and 70 mJy beam^{-1} for the upper sideband.

3. Observational results

3.1. Continuum emission

Orion-KL has a rich spectrum of molecular emission lines, so extracting the continuum requires some care. To construct our continuum map, we averaged the line-free parts of the upper and lower sidebands from the SMA-only data. In Figure 2, we present the resulting 1.3 mm continuum image as contours overlaid on a map of the outflow traced by shock-excited H_2 (Nissen et al. 2007). We detected the previously known compact continuum substructures of this region and moreover, resolved some of these substructures into multiple distinct condensations. We list the following resolved condensations in Table 1:

- The brightest hot core (HC): Located close to a well-studied infrared source IRC2 (Downes et al. 1981; Wynn-Williams et al. 1984), the brightest HC is the first clump in Orion-KL

¹ <http://cfa-www.harvard.edu/~cqi/mircook.html>.

² <http://casa.nrao.edu>

³ <http://www.iram.es/IRAMES/mainWiki/Iram30mEfficiencies>

⁴ <http://www.iram.fr/IRAMFR/GILDAS>

⁵ <https://www.cfa.harvard.edu/sma/miriad/manuals/SMAguide/mauserhtml/uvmodel.html>

detected by the high spatial resolution mm observations (Masson et al. 1985; Mundy et al. 1986; Woody et al. 1989; Wright et al. 1992), and it exhibits the highest peak specific intensity (Jy beam^{-1}) in the 1.3 mm SMA continuum map. With the temperature estimated to be 100–300 K (e.g., Wilner et al. 1994; Wilson et al. 2000; Beuther et al. 2005), this source has been found to be abundant in hydrogenated species and nitrogen- (N-) bearing molecules (Sutton et al. 1995; Blake et al. 1996; Wright et al. 1996; Wilson et al. 2000). With even higher resolution ($0.7''$, ~ 300 AU), observations from SMA at $865 \mu\text{m}/348$ GHz expose additional substructures within the HC (Beuther et al. 2004). Presented as black contours overlaid on the 1.3 mm colourmap in the inner panel of Figure 2, these $865 \mu\text{m}$ structures are: SMA1 (a high-mass protostellar source, suggested to be the driving source of the high-velocity outflow; Beuther & Nissen 2008), Source I (located at the centre of the SiO masers and believed to drive the bipolar low-velocity outflow; Menten & Reid 1995; Matthews et al. 2010), Source N (a Herbig Ae/Be or mid-B star with a luminosity of $\sim 2000 L_{\odot}$; Menten & Reid 1995; Greenhill et al. 2004; Gómez et al. 2005; Rodríguez et al. 2005; Goddi et al. 2011b; Nissen et al. 2012), and hotcore. Hereafter, we use “HC” to denote the whole region resolved by 1.3 mm continuum at a spatial resolution of ~ 1200 AU, the “hotcore” to denote the position resolved by $865 \mu\text{m}$ continuum at a spatial resolution of ~ 300 AU, and the “hot molecular core” to describe an evolutionary status.

- mm2: Located $\sim 7''$ west of the HC, and $\sim 5''$ south of the BN object. Coincident with infrared sources IRC3, IRC6, and IRC20 (Dougados et al. 1993), this condensation is also known as the western clump (WC; Wright et al. 1992), or the north-west clump (NWC; Blake et al. 1996; Tang et al. 2010; Favre et al. 2011a). The mass ($2\text{--}3 M_{\odot}$), H_2 column density, and high temperature (a few hundred K) in this source suggest that it may be the site of ongoing low-mass star formation (Schreyer & Henning 1999).
- mm3a and mm3b: These two condensations are located south-west of the HC. Coincident with infrared IRC5 (Dougados et al. 1993), they were previously considered to be a single clump called the south-west clump (SWC; Tang et al. 2010), or CntC (Murata et al. 1992), situated at the compact ridge (CR; Blake et al. 1996; Wright et al. 1996; Tang et al. 2010). Similar dual continuum peaks have been detected in other high spatial resolution observations of HMSFRs (Tang et al. 2010; Favre et al. 2011a; Friedel & Widicus Weaver 2011), so we consider them to be separated. The CR is known to have different kinematics and chemistry than in the HC: it is a vast region ($\sim 15''\text{--}25''$; Plume et al. 2012; Esplugues et al. 2013) with lower temperature (Genzel & Stutzki 1989), is dominated by oxygen- (O-) bearing molecules (Blake et al. 1987; Wright et al. 1996; Liu et al. 2002), and is believed to be the region where two outflows interact with the dense ambient material (Blake et al. 1987; Liu et al. 2002). Therefore, to ensure that we fully characterise its chemical properties, the following study focuses separately on mm3a and mm3b, instead of considering CR as a whole.
- The southern ridge (SR): the southernmost condensation detected in the 1.3 mm continuum map. Although it has been detected in other observations (Eisner et al. 2008; Favre

et al. 2011a), it has not been characterized in detail.

- The north-east clump (NE): a strong continuum emission peak which is adjacent the HC and the north extended ridge (ER; Sutton et al. 1985; Blake et al. 1987). This clump is usually filtered out in high spatial resolution observations, but can be clearly detected in interferometric observations made with large scale configurations (Murata et al. 1992; Tang et al. 2010). Comparison with the existing single-dish maps suggests it is part of a large-scale dusty filament along the NE–SW direction (e.g., detected by JCMT at $450 \mu\text{m}$, Wright et al. 1992; SCUBA at $450 \mu\text{m}$ and $850 \mu\text{m}$, Di Francesco et al. 2008). In addition, this clump is in the plateau of the low-velocity outflow, so its chemistry may be affected by shocks (Section 5.3).

Because of the limited UV coverage and field of view, the high-velocity outflow and the BN object are not detected above 5σ in the SMA-only continuum map. To study the chemistry in these regions from the combined data, we take the positions of the high-velocity plateau ($V_{\text{lsr}} \sim 11 \text{ km s}^{-1}$) and BN object from Beckwith et al. (1978) and denote them as OF1N, OF1S, and BN in Figure 2.

Table 1 lists the nominal absolute positions of these substructures, as well as the peak specific intensity (Jy beam^{-1}) for each continuum substructure, obtained from the SMA-only 1.3 mm continuum map (Figure 2, for more detail about this table, see Section 4.2.2). The HC is the brightest condensation; mm2, mm3a, and mm3b are fainter; while NE, SR, OF1N, and OF1S are even weaker.

3.2. Spectral line emission

3.2.1. Line identification

After imaging the whole SMA-30 m combined data cube, we extracted the double sideband spectrum from each substructure denoted in Figure 2 and show them in Figure 3. The majority of lines are strongest towards the HC, so we use the spectrum from the HC to identify lines. However, line identification may be ambiguous in a region such as the Orion-KL HC, because of a high density of lines (that can have different line widths according the species), also because the $\sim 1.2 \text{ km s}^{-1}$ spectral resolution of the observations does not allow us to separate all the blending. For strong lines, we first compare their rest frequencies with an existing single-dish survey catalogue of Orion-KL by Sutton et al. (1985). Next, we cross-check their rest frequencies with the molecular database at “Splatalogue”⁶ (a compilation of the Jet Propulsion Laboratory (JPL⁷, Pickett et al. 1998), Cologne Database for Molecular Spectroscopy catalogues (CDMS⁸, Müller et al. 2005), and Lovas/NIST catalogues, Lovas 2004), and confirm the identification if the

⁶ www.splatalogue.net

⁷ <http://spec.jpl.nasa.gov>

⁸ <http://www.astro.uni-koeln.de/cdms/catalog>

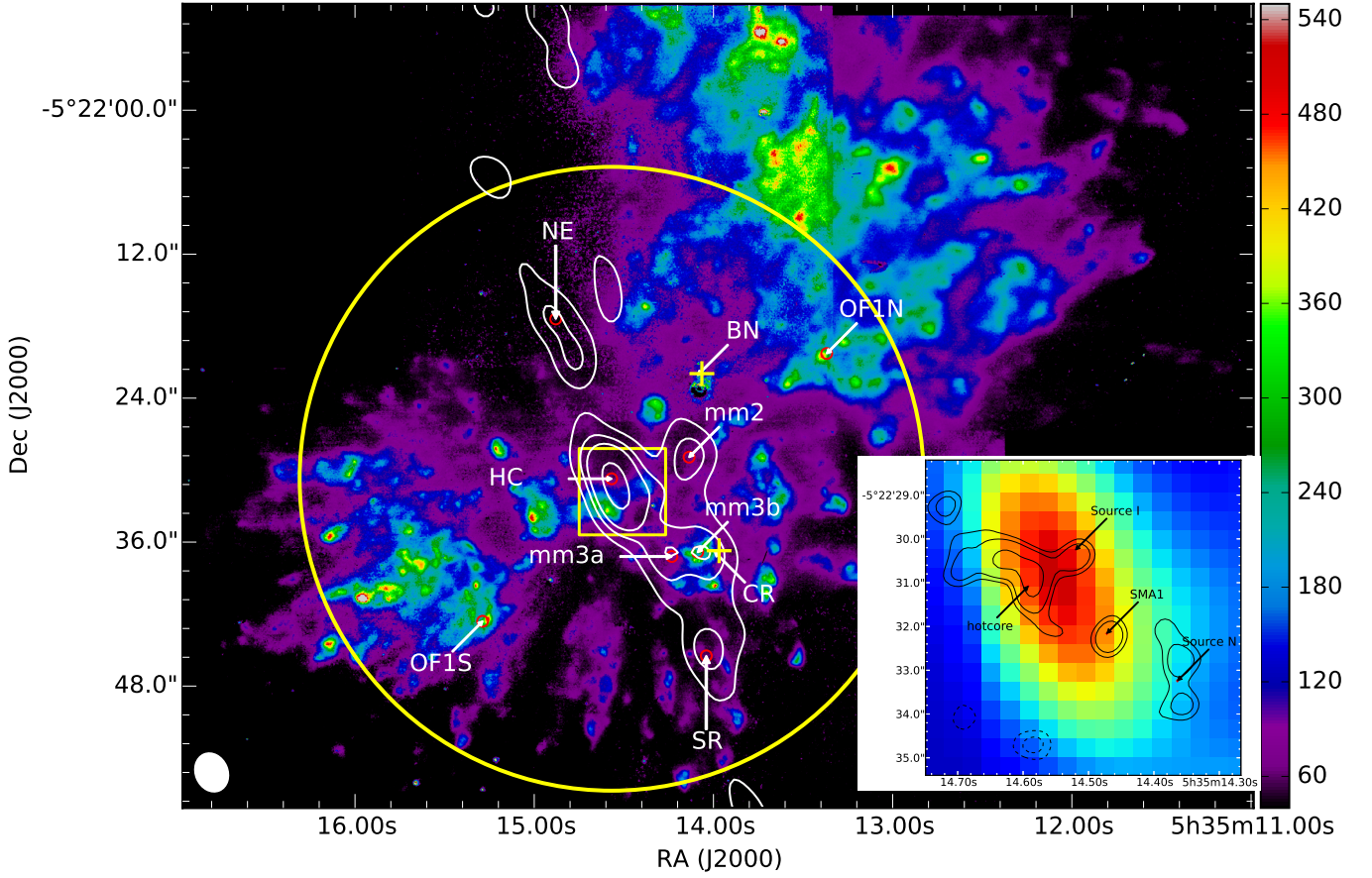


Fig. 2: Substructures resolved by SMA-only observations at a spatial resolution of ~ 1200 AU. White contours show the 1.3 mm continuum emission at -5σ , 5σ , 15σ , 25σ , and 60σ rms levels with the $\sigma = 0.04$ Jy beam $^{-1}$. The yellow circle denotes the primary beam of SMA at 1.3 mm. Red circles denote the peaks of hot core (HC), mm2, mm3a, mm3b, the southern region (SR), north-east clump (NE), the NW and SE parts of the high-velocity outflow (OF1N, OF1S). Yellow crosses denote the BN object and the compact ridge (CR). The beam in the bottom left corner is from the SMA-only data. Colourmap shows the brightness (in counts per 400 s) of shocked H₂ emission (Nissen et al. 2007). Corresponding to the yellow square, the insert panel shows the HC continuum from the SMA at 1.3 mm in detail as colourmap, with black contours of the 865 μ m continuum emission at a spatial resolution of ~ 300 AU from Beuther et al. (2004) overlaid.

CDMS/JPL intensity is $> 10^{-6}$ nm²MHz⁹.

⁹ This is a coarse cutoff for identifying the strong emission lines, corresponding to spontaneous emission rate $A_{ul} \sim 10^{-5.5 \sim -6}$. Taking the frequency resolution of our observations into consideration (~ 0.8 MHz), we found that 50% number possibility at certain rest frequency of a particular line has CDMS/JPL intensity $> 10^{-6}$.

Table 1: Properties of substructures, which are denoted on the continuum image obtained from SMA observations at 1.3 mm (Figure 2).

Source	R. A. (α) [J2000] 5h35m ~	Dec. (δ) [J2000] −5°22′ ~	I_ν^a (Jy/beam)	T_{rot} (K)	$N_{\text{H}_2,1}^d$ (10^{23}cm^{-2}) 3.49'' × 2.57''	$N_{\text{H}_2,2}^e$ (10^{23}cm^{-2}) 5.55'' × 4.35''	Alternative Designations
HC	14.6s	31.0''	2.75 ± 0.3	155 ± 16 ^{b₁}	23.7 ± 4.6	11.9 ± 0.7	Ca ^j , SMM3 ^l , CntB ^k
				121 ± 16 ^{b₂}	31.0 ± 6.7		
				126 ± 13 ^{b₃}	29.6 ± 5.8		
				225 ± 19 ^{b₄}	16.3 ± 2.9		
				199 ± 45 ^{b₅}	18.4 ± 5.1		
hotcore ^f	14.58s	30.97''					
SMA1 ^f	14.46s	32.36''					
Source I ^g	14.51s	30.53''					
Source N ^g	14.35s	33.49''					
mm2	14.1s	27.1''	0.87 ± 0.10	108 ± 4 ^{b₁}	11.0 ± 1.7	9.3 ± 0.1	NWC ^{h,i} , Cc ^j , SMM2 ^l , WC ⁿ , CntD ^k
				112 ± 7 ^{b₃}	10.5 ± 1.8		
				174 ± 14 ^{b₄}	6.7 ± 1.2		
				173 ± 40 ^{b₅}	6.7 ± 1.9		
CR ^l	14.0s	36.9''					SWC ⁱ , SMM1 ^l
mm3a	14.3s	37.9''	0.96 ± 0.09	103 ± 3 ^{b₁}	12.8 ± 1.6	6.2 ± 0.07	Cb1 ^j , CntC ^k
				101 ± 5 ^{b₃}	13.1 ± 1.8		
				159 ± 12 ^{b₄}	8.1 ± 1.3		
				101 ± 26 ^{b₅}	13.1 ± 3.7		
mm3b	14.1s	36.4''	1.01 ± 0.11	88 ± 6 ^{b₁}	15.9 ± 2.7	6.7 ± 0.05	Cb2 ^j , CntC ^k
				102 ± 5 ^{b₃}	13.5 ± 2.1		
				160 ± 17 ^{b₄}	8.5 ± 1.6		
				89 ± 24 ^{b₅}	15.6 ± 4.8		
NE	14.8s	19.1''	0.38 ± 0.09	43 ± 3 ^{b₁}	20.1 ± 4.2	3.3 ± 0.06	CntH ^k
SR	14.0s	45.4''	0.41 ± 0.06	43 ± 3 ^c	14.2 ± 2.9	1.0 ± 0.02	Cd ^j , MM23 ^m
OF1N	13.4s	20.5''	$\sigma = 0.04$	43 ± 3 ^c	< 4.2	~ 1.1	PK1 ^o
OF1S	15.3s	42.5''	$\sigma = 0.03$	43 ± 3 ^c	< 3.1	~ 0.6	PK2 ^o
BN ^o	14.11s	22.7''					

Notes. Positions with upper case are from the references listed in the footnotes, without are from 1.3 mm SMA continuum observations.

a. Peak specific intensity I_ν is obtained from each substructure of SMA-only continuum.

b₁. Excitation temperature is from CH₃CN rotation map fitting in Figure 8.

b₂. Excitation temperature is from CH₃¹³CN rotation map fitting in Figure 8.

b₃. Excitation temperature is from HCOOCH₃ rotation map fitting in Figure 9.

b₄. Excitation temperature is from CH₃OH rotation map fitting in Figure 9.

b₅. Excitation temperature is from ³⁴SO₂ rotation map fitting in Figure 9.

c. Excitation temperature is assumed the same as that in NE from CH₃CN.

d. H₂ column density is calculated from the SMA-only continuum at substructure peak using Eq. 11, performed in Section 4.2.2.

e. H₂ column density is calculated from the conversion of combined SMA-30 m C¹⁸O at temperatures derived from HCOOCH₃, performed in Section 4.2.2.

References. f. Beuther et al. (2004);

g. Menten & Reid (1995);

h. Blake et al. (1996);

i. Tang et al. (2010);

j. Favre et al. (2011a);

k. Murata et al. (1992);

l. Zapata et al. (2011);

m. Eisner et al. (2008);

n. Wright et al. (1992);

o. Beckwith et al. (1978)

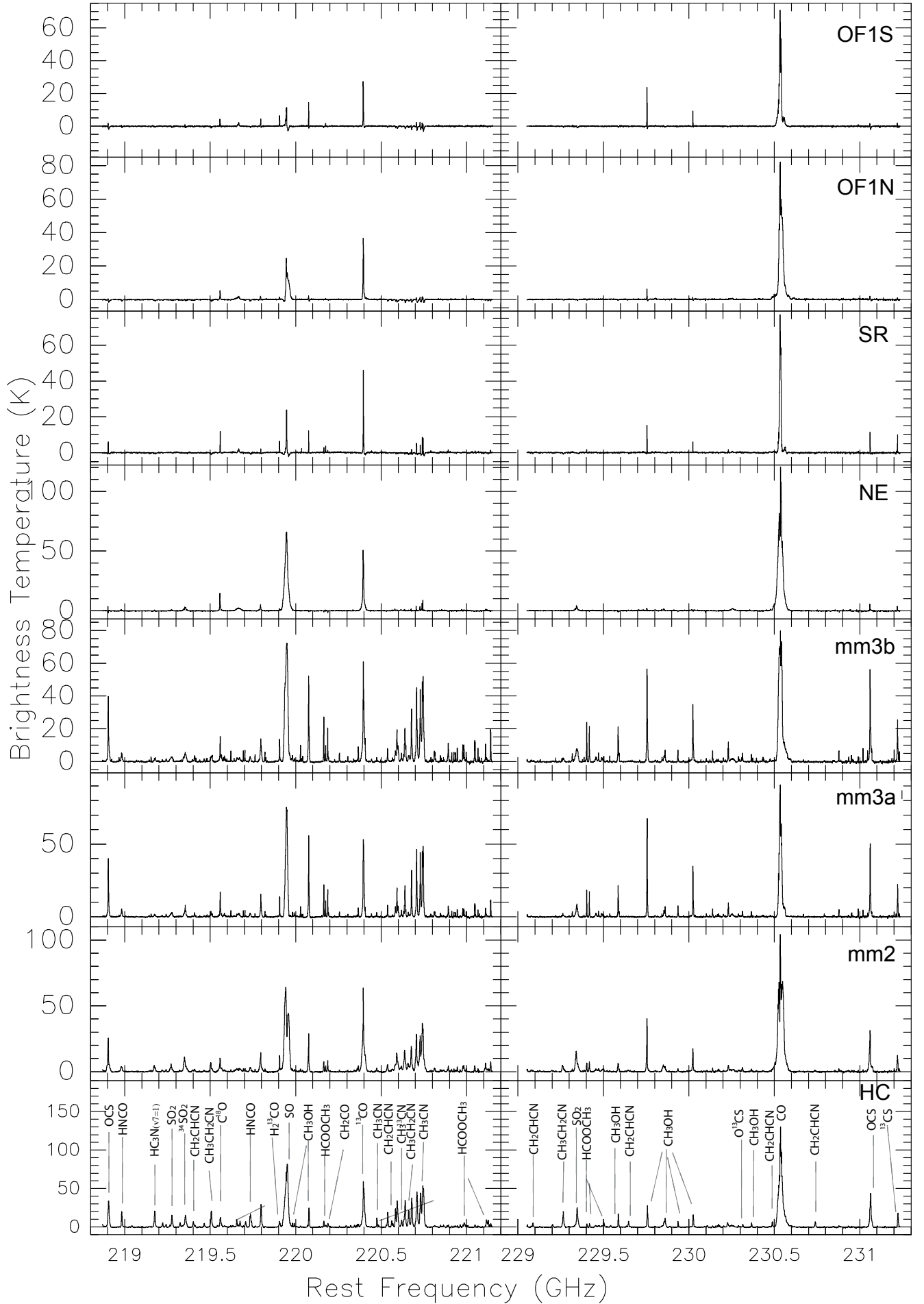


Fig. 3: Spectra taken towards selected positions (denoted by red circles in Figure 2) after imaging the whole data cube. The spectral resolution is smoothed to 1.2 km s^{-1} after the combination of SMA and 30 m data, and strong emission lines are labelled. A blow-up figure of the spectrum in the HC is Figure A1.

Using the above method, the detection of strong lines are shown in Figure A1. In addition, we can also detect multiple transitions of low-abundance COMs in Orion-KL, owing to the high sensitivity and recovering the full intensity for spatially extended molecular emission from the combined dataset. We use a synthetic spectrum fitting program (Sanchez-Monge 2011; Palau et al. 2011) in conjunction with molecular data from the JPL/CDMS catalogues, to simultaneously fit multiple COM lines under the assumption that all transitions are optically thin, are in local thermodynamic equilibrium (LTE), and have the same line width¹⁰. Given these assumptions, the fitted flux densities are not always a perfect match to the observed spectra. However, in many cases we are able to robustly identify multiple transitions of a COM (Figure A2). We discuss the properties of the identified COM species further in Section 3.2.2.

With these two approaches, we identified more than 160 lines that we assigned to 20 molecules (including 25 isotopologues) over the entire band; we labelled the unblended strong emissions in Figure 3, and list all the lines in Table A1. This table includes the rest frequency, quantum number, symmetry label, and upper state energy for each transition. Lines marked with “†” are from molecules containing less than six atoms as shown in Figure 4, and those marked with “‡” are from molecules we designated as COMs and carbon chains, which are shown in Figure 5. Our observations have a frequency resolution of 0.8125 MHz ($\sim 1.2 \text{ km s}^{-1}$ at 1.3 mm). Thus, some observed lines with broad linewidths can be attributed to multiple transitions, when compared to the laboratory-measured rest frequencies recorded in the “Splatalogue” database. If potentially blended transitions for one line are from different isotopologues but have similarly strong CDMS/JPL intensities, we compared the spatial distribution of this line to those of the known isotopologues. Then, we either confirm a match or indicate all possibilities with “*” in Table A1. If there are multiple possible transitions from the same isotopologue at this rest frequency, they are also marked with “*”.

3.2.2. Line imaging

In general, all the identified species show different spatial distributions, velocity widths (FWHM ΔV), and velocity at line centre (V_{peak}) in each substructure (see Figure A3, on average, $V_{\text{peak}} \sim 6\text{--}8 \text{ km s}^{-1}$ in the HC; $V_{\text{peak}} \sim 8\text{--}10 \text{ km s}^{-1}$ in mm2, mm3a, and mm3b; $V_{\text{peak}} \sim 10\text{--}12 \text{ km s}^{-1}$ in NE). However, transitions from a single isotopologue have the same spatial distribution (except for CH_3OH). In this paper, we have chosen one of the strongest unblended transitions from each isotopologue and produced their intensity distribution maps from the SMA-30m combined data. In avoiding contamination from other strong lines, we integrate the intensity of each line through 40%-60% of their profile range in Figure A3¹¹.

¹⁰ The synthetic fitting program we use here is for line detection, but not for finding the best fit of column density or temperature to the observations. Since the synthetic fitting is performed with optically thin assumption, minor lines of a particular species which cannot fit as well as the majority may be optically thick.

¹¹ The chosen velocity ranges are slightly larger than the FWHM of the lines, when accounting for the small variation in the peak velocity between different substructures.

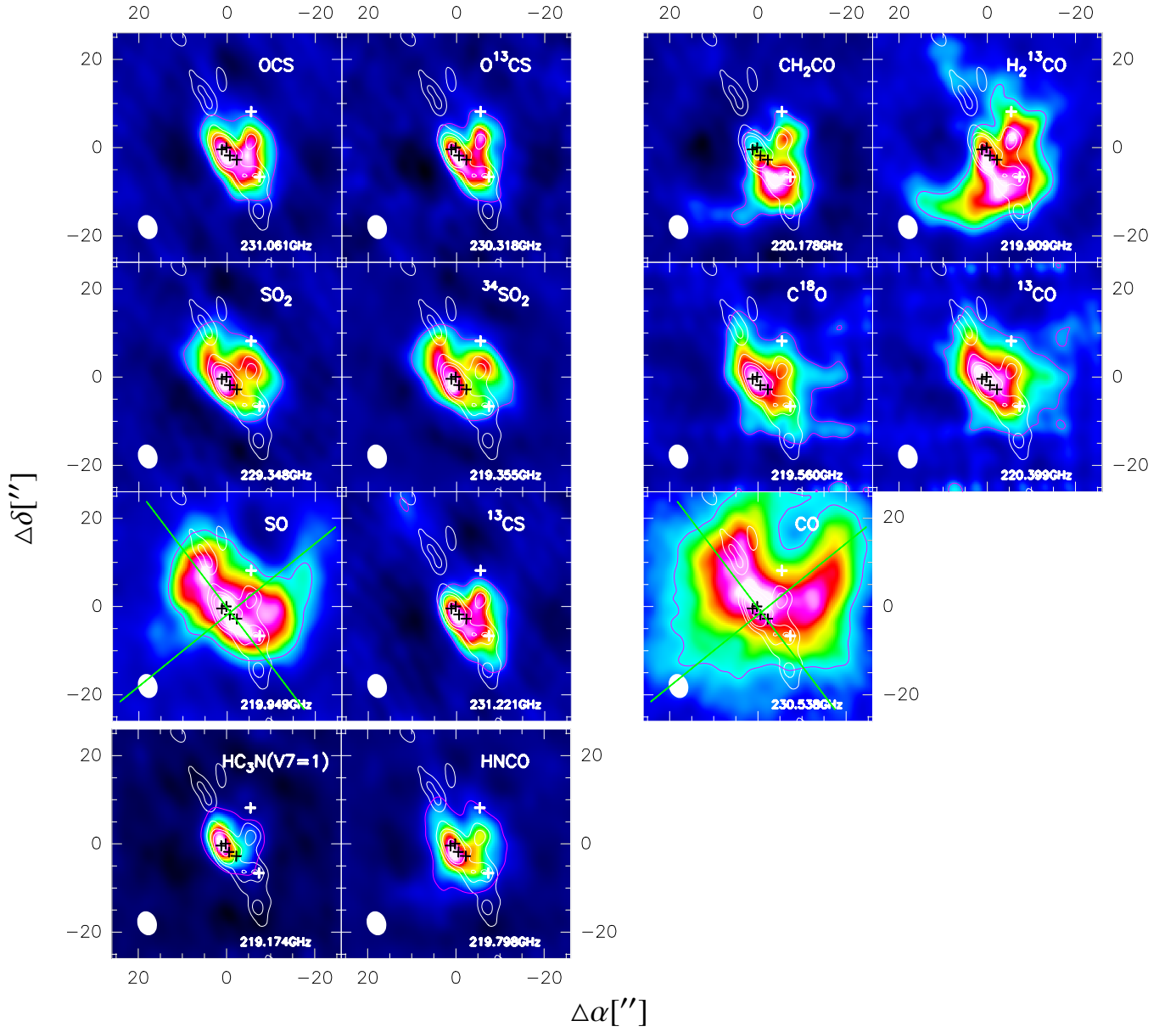
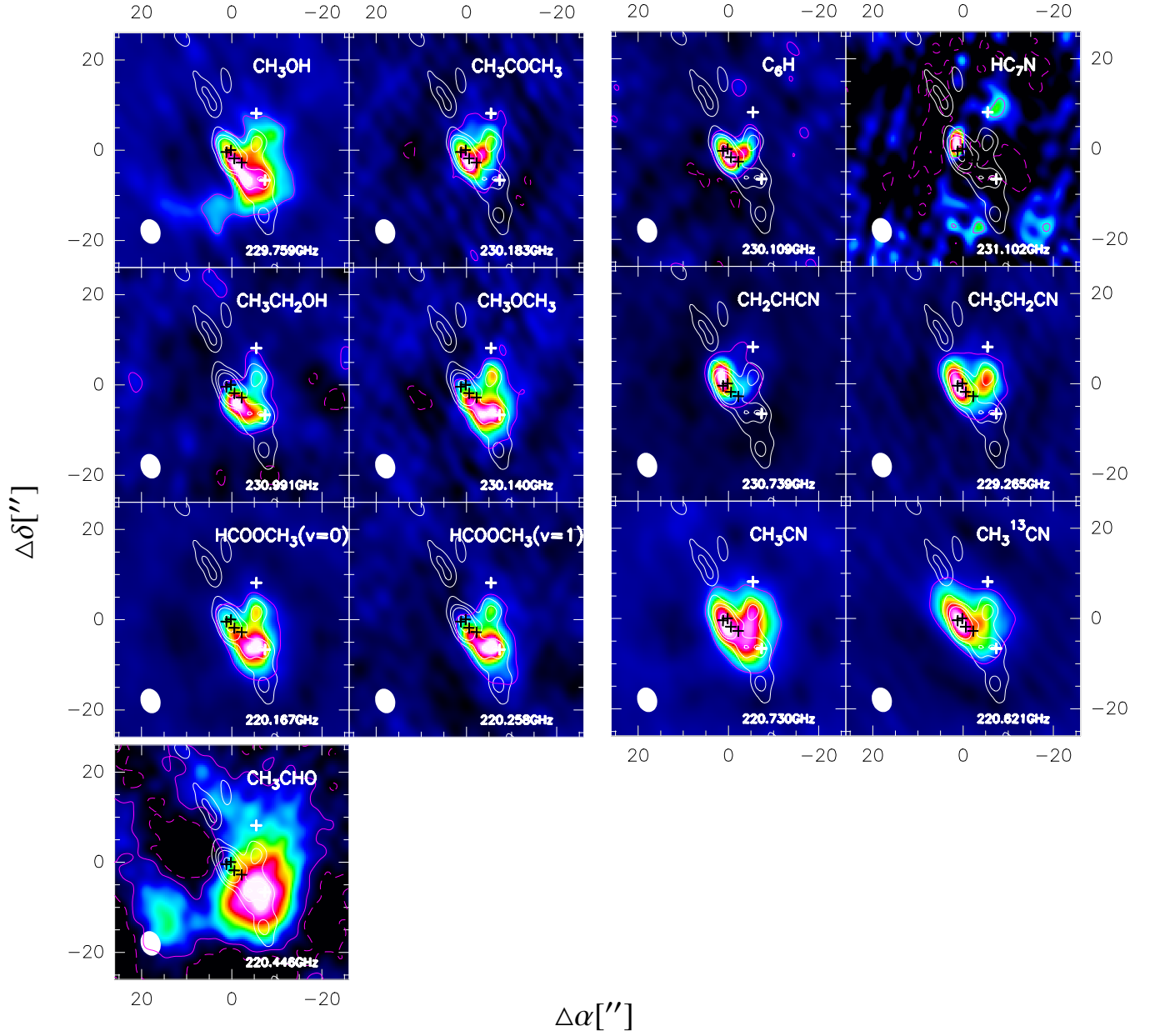


Fig. 4: Intensity distribution maps of transitions from molecules containing <6 atoms, which are detected in the combined SMA-30 m data at 1.3 mm (corresponding quantum numbers are listed in Table A1, with “†” marks). The intensities have been derived by integrating the line emission over the velocity range shown in Figure A3. The filled beam in the bottom left corner is from SMA-30 m data. White contours show the continuum from the SMA-only data (at -5σ , 5σ , 15σ , 25σ , and 60σ levels). Purple contours show $\pm 1\sigma$ levels of the molecular emission (solid contours indicate positive flux, and dashed contours indicate negative flux). Green lines in the SO and CO maps sketch the outflow directions. The white crosses denote the BN object and the CR, and the black crosses denote the positions of the hotcore, Source I, Source N, and SMA1, as in Figure 2. All images have different colour scales (in $\text{Jy beam}^{-1} \text{ km s}^{-1}$), increasing from black to white, which are optimized to emphasize the features in the distribution of each molecules.



* Channel maps of more CH_3OH lines are shown in Figure A6.

Fig. 5: Intensity distribution maps of transitions from COMs and carbon chains detected in the combined SMA-30 m data at 1.3 mm (corresponding quantum numbers are list in Table A1, with “ \ddagger ” marks). The intensities have been derived by integrating the line emission over the velocity range shown in Figure A3. The filled beam in the bottom left corner is from SMA-30 m data. White contours show the continuum from the SMA-only data (at -5σ , 5σ , 15σ , 25σ , and 60σ levels). Purple contours show $\pm 1\sigma$ levels of the molecular emission (solid contours indicate positive flux, and dashed contours indicate negative flux). The white crosses denote the BN object and the CR, and the black crosses denote the positions of the hotcore, Source I, Source N, and SMA1, as in Figure 2. All images have different colour scales (in $\text{Jy beam}^{-1} \text{ km s}^{-1}$), increasing from black to white, which are optimized to emphasize the features in the distribution of each molecules.

The combined data at 220/230 GHz covers a field of view of $52''$, which is greater than the extent of the source (not including the outflows), so our maps exhibit negligible artefacts caused by residual missing flux. The high quality of our data allows us to map molecules, such as $^{34}\text{SO}_2$, O^{13}CS , HNCO , H_2^{13}CO , ^{13}CO , and CH_2CO for the first time with both high resolution and sensitivity to spatial information on all scales. After sorting by different groups, we present the intensity integration map for each identified groups molecule in Figures 4 and 5. Compared to previous sub-mm and mm (especially interferometric) observations in Orion-KL (listed in the following paragraphs), the main features of our molecular distribution maps are:

1. All the identified sulphur- (S-) bearing species in our dataset are diatomic/triatomic containing no hydrogen. Most of them have extended distributions (except for SO_2 and $^{34}\text{SO}_2$), exhibiting a V-shaped morphology that extends from the emission peak at HC, through mm3a, mm3b to mm2. Their velocities at line centre also vary among substructures from $\sim 6 \text{ km s}^{-1}$ (HC) through $8\text{--}10 \text{ km s}^{-1}$ (mm2, mm3a, mm3b, and SR) to $11\text{--}12 \text{ km s}^{-1}$ (NE).

- OCS and O^{13}CS (carbonyl sulphide) peak at SMA1 and have emission that extend to the CR. In addition, OCS is also detected in NE and SR. Although only one line of O^{13}CS is detected in our data ($19 \rightarrow 18$, Fig. 6), other lines of this isotopologue have been previously confirmed and imaged by single-dish observations (e.g., Sutton et al. 1985; Ziurys & McGonagle 1993; Tercero et al. 2010). In addition to the detections by single-dish surveys (e.g., Sutton et al. 1985; Turner 1991; Schilke et al. 1997; Tercero et al. 2010), previous interferometric surveys of OCS also reproduce the same V-shaped widespread intensity distribution of this molecule, peaking at the HC (e.g., Wright et al. 1996; Friedel & Snyder 2008).

- SO_2 and $^{34}\text{SO}_2$ (sulphur dioxide) peak at the hotcore and SMA1 and exhibit extended emission in the NE direction, with $V_{\text{peak}} \sim 9\text{--}11 \text{ km s}^{-1}$. Unlike the other S-bearing species, no emission has been detected from these species in SR, and they do not display a clear V-shaped feature. However, there is a clear second velocity component in the line profile of $^{34}\text{SO}_2$ (at $\sim 22.7 \text{ km s}^{-1}$, Figure 7) and SO_2 (at 22.1 km s^{-1} , Figure 7). In addition, red- and blue-shifted $^{34}\text{SO}_2$ trace outflows in the NW–SE direction (Figure A4). Single-dish studies (e.g., SO_2 ; Blake et al. 1987; Persson et al. 2007; Esplugues et al. 2013, $^{34}\text{SO}_2$; Esplugues et al. 2013) conclude that this species is a good tracer not only for the warm dense gas, but also for regions affected by shocks. While based on the velocity around 22 km s^{-1} , Esplugues et al. (2013)¹² suggests that this velocity component may be associated with shocks caused by the explosive (NW–SE) outflow and/or the BN object, our data clearly show that this velocity component of SO_2 is spatially offset from BN and seems to be associated much more with the main NE–SW outflow (Figure A5). On small scales, interferometric observations of Orion-KL also detect a compact SO_2 emission peak (Wright et al. 1996; Zapata et al. 2011) and strong extended emission of

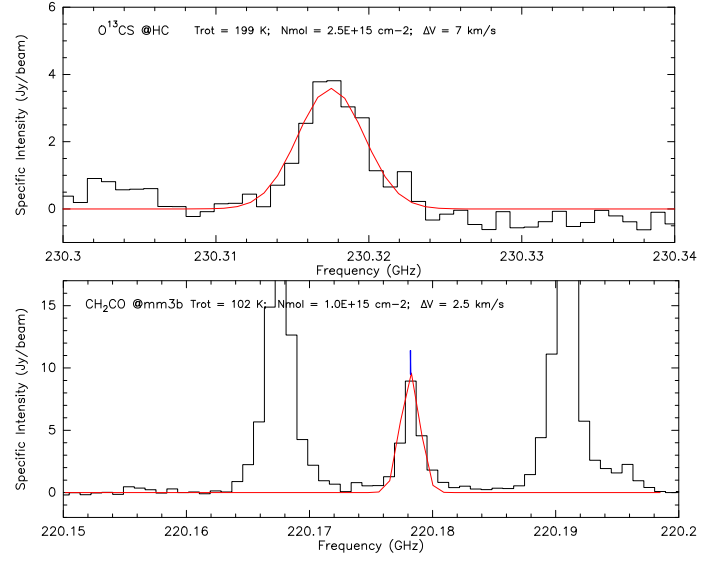


Fig. 6: Lines that only have one transition with low specific intensity ($\leq 10 \text{ Jy beam}^{-1}$) in our data, fitted with synthetic spectrum from their emission peaks.

$^{34}\text{SO}_2$ to mm2 (Beuther et al. 2005).

- SO (sulphur monoxide) has multiple strong emission peaks towards HC, NE, mm3a, and mm3b and exhibits strong self-absorption in mm2 (Figure A3). There is also significant emission extending along both the plateau of high- ($V_{\text{peak}} \sim 8\text{--}10 \text{ km s}^{-1}$) and low-velocity ($V_{\text{peak}} \sim 7\text{--}8 \text{ km s}^{-1}$) outflows. Similar to $^{34}\text{SO}_2$, its line wings are broad ($\Delta V \sim 23 \text{ km s}^{-1}$), and a second velocity component is clear in the line profile at $\sim 21 \text{ km s}^{-1}$ (see Figure A3 mm3b), which may be associated with shock events¹³. These morphological features (elongated emission peak(s) and broad line wings of SO) have also been detected by both single-dish (Persson et al. 2007; Esplugues et al. 2013) and interferometric (Wright et al. 1996) line studies.

- ^{13}CS (carbon monosulphide) has only one transition in our data set, but it is very strong, peaking at SMA1, with a similar distribution to O^{13}CS —extended emission from NE through HC to the CR. Owing to its high dipole moment, this molecule is considered to be a dense gas tracer (e.g., Bronfman et al. 1996), and its detection in both CR and NE is confirmed by Persson et al. (2007) and Tercero et al. (2010).

2. The distribution of simple $\text{C}_x\text{H}_y\text{O}_z$ ($x, z = 1, 2, \dots$; $y = 0, 1, 2, \dots$; $x + y + z \leq 5$) molecules are co-spatially extended.
 - CO , C^{18}O , and ^{13}CO (carbon monoxide) have a common morphological peak at the HC (though the integrated intensity of CO peaks north of the HC due to its strong self-absorption in this source, see Figure A3). Velocity

¹³ The line wing of SO at $\sim 7 \text{ km s}^{-1}$ is broad, and its second velocity component is blended, so we cannot tell the origin of the shock precisely from our observations, Figure A5.

¹² $V_{\text{peak}} = 20.5 \text{ km s}^{-1}$ in Esplugues et al. (2013)

at line centre V_{peak} ranges from 6 km s^{-1} (HC) through 8 km s^{-1} (mm2, mm3a, mm3b, and SR) to 10 km s^{-1} (NE, OF1N, and OF1S), with broad red- and blue-shifted line wings trace both high-velocity (CO, ^{13}CO) and low-velocity (C^{18}O) outflows (Figure A4). As the second most abundant species in the ISM, this species has been detected in numerous other observations of Orion-KL (C^{18}O ; Beuther & Nissen 2008; Plume et al. 2012, CO; Zuckerman et al. 1976; Kwan & Scoville 1976; Erickson et al. 1982; Blake et al. 1987 (single-dish), Masson et al. 1987; Chernin & Wright 1996; Zapata et al. 2009; Peng et al. 2012b (interferometry), ^{13}CO ; Wilson et al. 2011 (single-dish)), showing the same morphology as we see: extended structure, with bipolar line wings covering from the NE through HC to the CR and tracing outflows.

- CH_2CO (ketene) has a single transition ($11_{1,11} \rightarrow 10_{1,10}$) detected (Figure 6), peaking at mm3a and mm3b, with strong emission extending to the OF1S and the NE filament. With $V_{\text{peak}} \sim 8 \text{ km s}^{-1}$ and $\Delta V \sim 2.5 \text{ km s}^{-1}$ in mm2, mm3a, and mm3b, this line has also been confirmed by Sutton et al. (1985). Some other lines of this species are also detected in Orion-KL by Lee & Cho (2002).
- H_2^{13}CO (formaldehyde) exhibits an elongated peak stretching from SMA1 towards mm3a. Similar to the simple organic CH_2CO , it also shows extended structure along the SE lobe of the high-velocity outflow and NE. Single-dish detections (e.g., Persson et al. 2007) confirm that this molecule is present in both the CR and the outflows.
- 3. HNC (isocyanic acid) is the simplest organic molecule containing C, H, O, and N elements. Peaking at SMA1, it shows extended emission towards all the substructures, with V_{peak} ranging from 6 km s^{-1} (HC) through $7\text{--}8 \text{ km s}^{-1}$ (mm3a, mm3b, SR, and OF1S) to $9\text{--}10 \text{ km s}^{-1}$ (mm2, NE, OF1N), and a second velocity component at $\sim 19.8 \text{ km s}^{-1}$ (Figure 7). Although the formation pathway of HNC is still not clear (Hasegawa & Herbst 1993; Turner et al. 1999; Garrod et al. 2008; Tideswell et al. 2010), its distribution is observed to be correlated with shock tracing molecules SiO (e.g., Zinchenko et al. 2000) and CH_3OH (e.g., Meier & Turner 2005), suggesting that it is also produced in shocks.
- 4. In contrast, highly saturated COMs¹⁴ are the typical COMs detected in HMSFRs, and they exhibit a variety of morphological structures in Orion-KL. In general, N-bearing COMs have a similar peak to HNC, at or near HC; while most of the O-bearing COMs are co-spatial with CH_2CO —peaking at mm3a and mm3b, and extending even to southern CR (e.g., HCOOCH_3 , CH_3OCH_3 , and CH_3CHO). This spatial segregation of the N- and O-bearing COM peaks has also been reported by other single-dish (Blake et al. 1987; Persson et al. 2007) and interferometric studies with high spatial resolution (e.g., Wright et al. 1996; Beuther et al. 2005; Favre et al. 2011a; Friedel & Widicus Weaver 2012). In addition, there are several other O-bearing COMs identified in this study, which have unique morphologies. To understand the

¹⁴ A COM that has a chain of carbon atoms linked together by single bonds and has rich hydrogen atoms filling the other bonding orbitals of the carbon atoms.

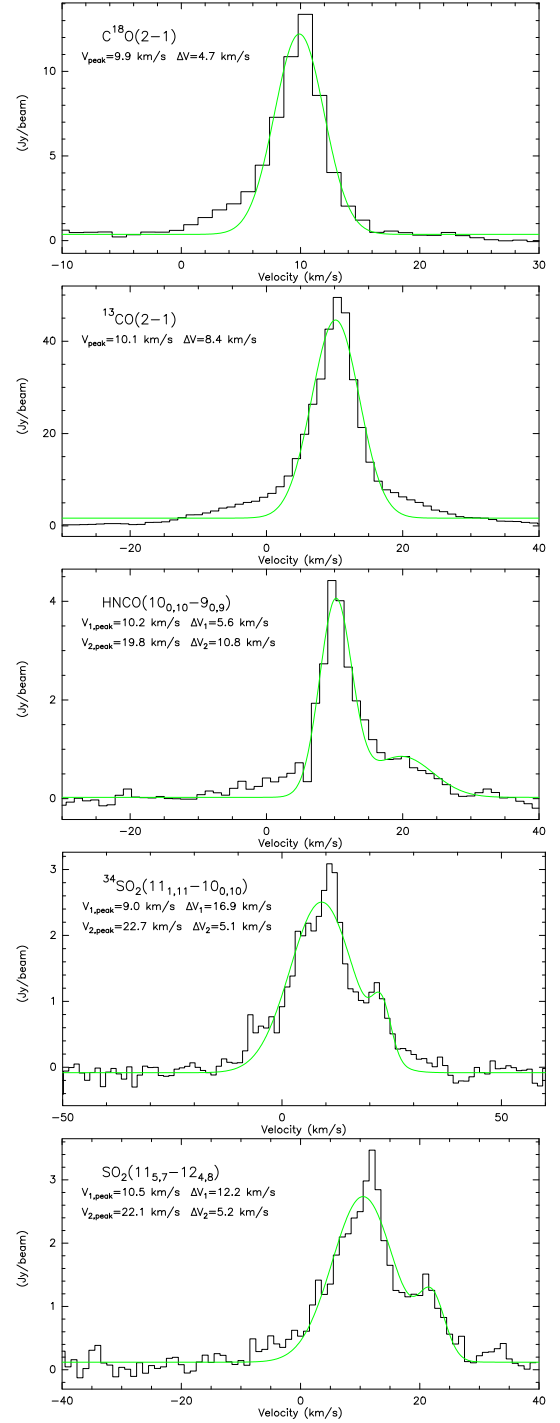


Fig. 7: Gaussian fitting to the line profile of ^{13}CO , C^{18}O , HNC, SO_2 , and $^{34}\text{SO}_2$ extracted from NE. Outflow signatures are seen in the broad line wings and the second velocity component in the HNC, SO_2 , and $^{34}\text{SO}_2$ line profile.

spatial differentiation of COMs on small scales (Figure 5), we compared the distributions of these molecules between our observations to other recent interferometric studies (Table 2).

- CH_3CN and $\text{CH}_3^{13}\text{CN}$ (methyl cyanide) are two abundant N-bearing COMs. In our dataset, we detect the $J = 12 \rightarrow 11$ ladder of both isotopologues around 220 GHz. Most of the $\text{CH}_3^{13}\text{CN}$ lines are blended, but

lines with $K = 2, 4, 5, 6$ are clearly detected in the HC (Figure 8). In particular, $K = 2$ line of $\text{CH}_3^{13}\text{CN}$ and CH_3CN are clearly co-spatial (Figure A3), peaking at SMA1 ($V_{\text{peak}} \sim 5\text{--}7 \text{ km s}^{-1}$) and extending to mm2, mm3a, mm3b ($V_{\text{peak}} \sim 8\text{--}10 \text{ km s}^{-1}$), with $> 3\sigma$ detection in NE ($V_{\text{peak}} \sim 10\text{--}13 \text{ km s}^{-1}$), exhibiting a V-shaped morphology. CH_3CN is detected in SR and OF1N (S), but not for $\text{CH}_3^{13}\text{CN}$. This V-shaped morphology of CH_3CN has also been detected in e.g., Beuther et al. (2005); Zapata et al. (2011); Widicus Weaver & Friedel (2012); Bell et al. (2014), as well as the NE extension in Wright et al. (1996). This species is considered to be a warm and dense gas tracer (e.g., Kalenskii et al. 2000; Araya et al. 2005), with gas phase and grain surface chemical models predicting that it is only detected in an environment with elevated temperatures (e.g., Purcell et al. 2006). We use the CH_3CN ladder and the $\text{CH}_3^{13}\text{CN}(12_2 \rightarrow 11_2)$ line to estimate the temperature of the substructures where these lines are detected (see Section 4.1.1).

- CH_2CHCN (vinyl cyanide) exhibits strong compact emission north of the hotcore, with $V_{\text{peak}} \sim 5 \text{ km s}^{-1}$, and a slight extension towards mm2. The northern peak is also coincident with the one in higher resolution maps of this species from SMA at $865 \mu\text{m}$ (Beuther et al. 2005), CARMA at 1 mm (Friedel & Snyder 2008), and PdBI at 3 mm (Guélin et al. 2008).
- $\text{CH}_3\text{CH}_2\text{CN}$ (ethyl cyanide) emission also makes a V-shaped structure. Unlike the single-peaked structure of CH_2CHCN , $\text{CH}_3\text{CH}_2\text{CN}$ exhibits a dual-peaked structure, with a first emission peak at the hotcore ($\sim 6 \text{ km s}^{-1}$), and a second peak at mm2 ($\sim 9 \text{ km s}^{-1}$). Although there are two velocity components in both mm3a and mm3b (6 km s^{-1} , 10 km s^{-1}), there is no detection in southern CR, which is consistent with Blake et al. (1987). This observed morphology is consistent with other interferometric observations at high spatial resolution (Wright et al. 1996; Beuther et al. 2005; Friedel & Snyder 2008; Guélin et al. 2008; Widicus Weaver & Friedel 2012; Peng et al. 2013).
- CH_3OH (methanol) has multiple transitions in our data (Figure A2). We obtained the channel maps of all the unblended strong CH_3OH transitions in our dataset and found two types of spatial distributions (Figure A6). One type of line clearly shows extended emission from mm2 and SR ($7.2\text{--}8.4 \text{ km s}^{-1}$, e.g., lines of $8_{0,8} \rightarrow 7_{1,6}\text{E}$, $8_{-1,8} \rightarrow 7_{0,7}\text{E}$, and $3_{-2,2} \rightarrow 4_{-1,4}\text{E}$) towards the high-velocity outflow OF1N(S), exhibiting a similar SE tail to H_2^{13}CO at $7\text{--}10 \text{ km s}^{-1}$, which has not been detected before; whereas the other type of line (e.g., lines of $15_{4,11} \rightarrow 16_{3,13}\text{E}$, $22_{4,18} \rightarrow 21_{5,17}\text{E}$, and $19_{5,14} \rightarrow 20_{4,17}\text{A} \rightarrow -$) does not show such a SE tail. However, both of them show multiple velocity-dependent emission peaks: towards SMA1 at 5 km s^{-1} , mm3a at 8 km s^{-1} , and mm3b at 10 km s^{-1} . The multiple-peak structure is different from the traditional segregated dichotomous distribution of COMs in Orion-KL (i.e., the main emission peak is either at HC or mm3a(b)), though it has also been observed in other interferometric surveys (Wright et al. 1996; Beuther et al. 2005; Friedel & Snyder 2008; Guélin et al. 2008; Friedel & Widicus Weaver 2012; Peng et al. 2012a). Methanol has previously been detected in the Orion outflow (Wang et al. 2011), and furthermore, line $8_{-1,8} \rightarrow 7_{0,7}$ is known to be a potential Class I maser that traces shocks (Fish et al. 2011). As a result, the SE tail can be reasonably explained as a feature of the outflow. In addition, it is also suggested that the SMA1-Source N area is the launching point of the Orion-KL outflows (e.g., Menten & Reid 1995; Beuther & Nissen 2008), which may explain CH_3OH and H_2^{13}CO peaking in this area.
- HCOOCH_3 (methyl formate) has the largest number of detected lines in our data (Figure A2). There are two types of HCOOCH_3 in the whole observational band, torsionally excited lines ($\nu = 1$) and lines in ground state ($\nu = 0$). Both of them have identical distributions (Figure 5) that peak at both mm3a and mm3b, with a clear detection in the southern CR, which is similar to CH_2CO . This morphology has also been reported by Wright et al. (1996); Beuther et al. (2005); Guélin et al. (2008); Friedel & Snyder (2008); Favre et al. (2011a); Widicus Weaver & Friedel (2012), indicating that this species arises in a cooler and less dense environment than the HC.
- CH_3OCH_3 (dimethyl ether) peaks towards mm3a and mm3b and extends to the southern CR, similar to HCOOCH_3 . Unlike the other COMs, its emission in mm2 is considerably stronger than towards the HC. This morphology has also been imaged with other interferometric studies (Liu et al. 2002; Beuther et al. 2005; Guélin et al. 2008; Friedel & Snyder 2008; Favre et al. 2011b; Brouillet et al. 2013).
- $\text{CH}_3\text{CH}_2\text{OH}$ (ethanol), the functional isomer¹⁵ of CH_3OCH_3 , exhibits extended emission from the vicinity of HC to mm2, mm3a, and mm3b, indicating the same distinctive V-shaped molecular emission as the N-bearing COMs. However, unlike CH_3OCH_3 and the other COMs, it peaks in between the hotcore and mm3a. The difference in the location of their peaks is exactly the same as reported by Guélin et al. (2008); Brouillet et al. (2013) from PdBI and Friedel & Snyder (2008) with the EVLA and CARMA at high spatial resolution. In the grain mantle chemistry models, both isomers are produced from two radicals involved in the synthesis of CH_3OH ice (Garrod et al. 2008). Therefore, their spatial differentiation may result from the chemical differences between the CH_2OH and CH_3O radicals across Orion-KL, e.g., variations in production rates or chemical evolution (Brouillet et al. 2013).
- CH_3COCH_3 (acetone) is an O-bearing COM, though, it has a similar distribution to $\text{CH}_3\text{CH}_2\text{CN}$, which peaks at SMA1, extends to mm2, and has no detection in the southern CR. Although its nature as a hot molecular core tracer has been confirmed by detections in both Orion-KL (Friedel et al. 2005; Friedel & Snyder 2008; Widicus Weaver & Friedel 2012; Peng et al. 2013) and

¹⁵ Two compounds with the same molecular formula but different functional groups (radicals) are called functional isomers.

Sagittarius B2 (N-LHM) (Snyder et al. 2002), whether this species mainly forms on dust grains or in the gas phase is still not clear.

- CH_3CHO (acetaldehyde) is tentatively detected, as all lines except one at 220.446 GHz (Table A1) are blended with HCOOCH_3 . Morphologically, this line has a similar distribution to CH_2CO , peaking at mm3a and mm3b, with extended emission to the NE and SE tail. Although its origin is still unclear (Charnley 2004), it has been detected in Orion-KL with single-dish telescopes (Turner 1989). Previous interferometric observations failed to detect it because of filtering out the extended structure (e.g., Friedel & Snyder 2008; Widicus Weaver & Friedel 2012). However, its detection has been reported by recent CARMA and ALMA observations (Loomis, priv. comm), which shows the same distribution as our single-dish complemented interferometric observation result.
- There are also several other organics, such as CH_2OHCHO (glycolaldehyde), $(\text{CH}_2\text{OH})_2$ (ethylene glycol), and HCOOH (formic acid), which we do not detect in Orion-KL at 1.3 mm in the SMA-30 m combined data. Of the first two, although there are some candidate detections from our synthetic fitting, they are blended with other nearby lines, and so cannot be confirmed. Although Liu et al. (2002) claimed to detect HCOOH in the CR, in their data the line at 1 mm is only a 2σ feature. Widicus Weaver & Friedel (2012) also did not detect any compact concentrations of HCOOH in our studied region either, and they conclude that the HCOOH emission must be extended on > 1700 AU scales.

In brief, from our detections, N- and O-bearing COMs not only show two segregated peaks, but also exhibit more complicated spatial distributions. Most of the N-bearing species (except CH_2CHCN) are co-spatial and peak at the hotcore. While some O-bearing species (HCOOCH_3 , CH_3OCH_3 , and CH_3CHO) peak at mm3a and mm3b, and others present more unusual features (i.e., CH_3OH has velocity dependent peaks at both hotcore and mm3a/mm3b; $\text{CH}_3\text{CH}_2\text{OH}$ peaks in between mm3a and hotcore; and CH_3COCH_3 peaks in a similar location to N-bearing COMs). This challenges the traditional hypothesis that all of these molecules are forming in the same chemical and physical conditions (Garrod et al. 2008; Laas et al. 2011).

5. Unlike the saturated COMs, long carbon chains (organics with carbon-carbon multiple bonds) are less likely to be detected in star-forming regions (Thorwirth 2001; Rice & Maier 2013).

- C_6H is the parent radical of C_6H^- (the first molecular anion identified in the gas phase interstellar and circumstellar media; McCarthy et al. 2006), after its presence was predicted by Herbst (1981). It had not been detected in Orion-KL before. In our dataset, there is one unblended line at 230.109 GHz with $J = 165/2 \rightarrow 163/2$, although most transitions identified by the synthetic fitting of C_6H are blended. Emission from this tentative detected species appears to be confined to the HC.

- HC_3N and HC_7N are two cyanopolynes (HC_{2n+1}N , n is an integer). We confirmed the detection of $\text{HC}_3\text{N}(\nu_7 = 1)$ to the north of the hotcore and also tentatively detect HC_7N . Although only two out of four of the HC_7N lines predicted by the synthetic fitting programme are detected in our observations¹⁶, these lines are unblended and peak at a similar location to HC_3N . The excited-vibrational state ($\nu_7 = 1$) of HC_3N shows a similar confined structure north-east of the HC in Wright et al. (1996); Beuther et al. (2005) and Zapata et al. (2011), where it is said to form a shell around the HC. HC_3N is an especially useful dense gas tracer due to its relatively low optical depth transitions, large dipole moment, and simple linear structure (Bergin et al. 1996). The $\text{HC}_3\text{N}(\nu_7 = 1)$ lines are believed to be primarily excited by a strong mid-infrared radiation field (e.g., Goldsmith et al. 1982). A gas-phase chemical model of a hot molecular core with high but transitory abundances of cyanopolynes has been presented in Chapman et al. (2009), where these species are formed from reactions between the precursor C_{2n}H_2 (e.g., C_2H_2 , acetylene) and N-bearing species via gas phase chemistry (e.g., $\text{C}_{2n}\text{H}_2 + \text{CN} \rightarrow \text{HC}_{2n+1}\text{N} + \text{H}$).

4. Rotational temperature and abundance estimates

The above qualitative comparison of the morphology of different species show the chemical variations in the above-mentioned substructures. A more precise approach to studying these variations is to measure the quantitative differentiations in chemical parameters towards individual substructures, i.e., the temperatures, molecular column densities, and abundances.

4.1. Temperature estimates

Temperature is commonly used as a benchmark for comparing model results and observations. Since N-, O-, and S-bearing species show different spatial distributions, we estimate their temperatures in each substructure separately.

4.1.1. CH_3CN

A good tracer of temperature in high-density gas ($n \gtrsim 10^5 \text{ cm}^{-3}$) is CH_3CN , which is a symmetric-top molecule with no dipole moment perpendicular to the molecular axis, and its K ladders in rotational levels are excited solely by collisions. Provided that the collision rate is sufficient to thermalize the rotational levels within each K ladder, the rotational excitation temperature of CH_3CN is equal to the gas kinetic temperature (Boucher et al. 1980; Wright et al. 1995). Our observation band covers the $J = 12 \rightarrow 11$ transitions of CH_3CN around 220 GHz, with upper state energy levels from ~ 70 K to ~ 500 K, yielding a wide range for determining temperatures. If we assume that the emission from all of these transitions originate in the same parcels of gas along the line of sight in LTE, having the same size, velocity, and a single temperature, then rotational temperatures can be derived from the rotational diagrams (Hollis 1982; Loren & Mundy 1984; Olmi et al. 1993; Goldsmith & Langer 1999). Traditionally, in the optically thin limit, the level

¹⁶ Lines with $J = 196 \rightarrow 195$ and $J = 205 \rightarrow 204$ are detected, but neither $J = 195 \rightarrow 194$ nor $J = 204 \rightarrow 203$ are detected, so these potential detected lines are marked with “?” in Table A1.

Species	Identification	Peak	Column density @Peak (cm^{-2})	Other interferometric detections
CH_3CN , $\text{CH}_3^{13}\text{CN}$	✓	SMA1	1.4(17), 9.4(14)	a, b, e, i
CH_2CHCN	✓	North to hotcore	$\geq 5.0(15)$	b, d, e
$\text{CH}_3\text{CH}_2\text{CN}$	✓	hotcore	$\geq 1.1(16)$	a, b, d, e, i, k
CH_3OH	✓	SMA1 & mm3a	$\geq 2.5(17)$	a, b, d, e, f, i, m
HCOOCH_3	✓	mm3a & mm3b	$\geq 9.7(16)$	b, d, e, g, i, k
CH_3COCH_3	✓	SMA1	$\geq 1.5(16)$	c, i, k
CH_3OCH_3	✓	mm3a & mm3b	$\geq 2.0(17)$	b, d, e, h, i, j
$\text{CH}_3\text{CH}_2\text{OH}$	✓	near SMA1 & mm3a	$\geq 1.5(16)$	d (×), e and j (only 1 line)
$(\text{CH}_2\text{OH})_2$	×	–	–	–
CH_2OHCHO	×	–	–	g. (some lines $< 3\sigma$)
HCOOH	×	–	–	d (×), l ($< 3\sigma$), i (only from the extended configuration)
CH_3CHO	*	mm3a & mm3b	$\geq 1.3(16)$	d (×), i (×), n (ALMA)
C_6H	*	SMA1	$\geq 1.0(15)$	–
HC_7N	*	North to hotcore	$\geq 1.0(16)$	–

References. a. Wright et al. (1996); b. Beuther et al. (2005); c. Friedel et al. (2005); d. Friedel & Snyder (2008); e. Guélin et al. (2008); f. Zapata et al. (2011); g. Favre et al. (2011a); h. Favre et al. (2011b); i. Widicus Weaver & Friedel (2012); j. Brouillet et al. (2013); k. Peng et al. (2013); l. Liu et al. (2002); m. Peng et al. (2012a); n. R. Loomis, private communication.

Table 2: Identification of saturated COMs and complex carbon chains in Orion-KL. Confirmed COMs are marked with “✓”, tentative detections with “*”, and nondetections with “×”. At each of their main emission peak (Figure 5), column density of CH_3CN is obtained with optical depth correction, while column densities of the rest molecules are obtained at the temperature of an adjacent substructure from synthetic fittings, with an assumption that the species lines are optically thin (we denote them by “ \geq ”), $x(y) = x \times 10^y$.

populations are then directly proportional to the line intensities of the K components. The parameters used to estimate the level populations of CH_3CN transitions (i.e., the line strength $S_{ul}\mu^2$ (Debye²) and the lower state energy E_L (cm^{-1})) in our data are listed in Table A2.

The K = 3, 6 lines are from ortho (o-) transitions, which have a statistical weight that is twice as strong as those of the other para (p-) lines. Radiative transitions between o-/p-types are usually prohibited, so we exclude these lines in the optically thin rotation diagram fitting (shown in black lines in Figure 8, also see Andersson et al. 1984).

Panel 1 of Figure 8 shows the synthesised fitting under the assumption of optically thin emission in LTE for the HC with the dashed lines. To reduce the number of free parameters, we also assume that all the K = 0 – 8 components¹⁷ have the same line width. A satisfactory fit is obtained to all lines except K = 0, 1, 2. Since all transitions were observed simultaneously, calibration errors due to poor pointing or amplitude scaling are not responsible, and the remaining explanations for the deviations are as follows: (1). The K = 0, 1 lines are so close in frequency that they are blended in our fitting by the uniform line width we assumed. (2). It is also likely that lines at K = 2 are more optically thick.

Compared to CH_3CN , lines of its rare isotopologue $\text{CH}_3^{13}\text{CN}$ should be optically thin. However, $\text{CH}_3^{13}\text{CN}$ ($12_2 \rightarrow 11_2$) is the only transition that is not blended with the broad line wings of CH_3CN in substructures other than HC. Even in the HC, only the K = 2, 6, and 7 lines are unblended (Panel 7 of Figure 8). Excluding the o-type lines (K=3, 6), the rotation temperatures in HC we derive from the main and rare isotopologues of CH_3CN have large differences (black fittings in Panels 2 and

8 of Figure 8). Optical depth seems to be the most likely reason for such inconsistency, so to investigate this hypothesis, we use the following iterative approach to correct the optical depth of CH_3CN lines and derive the opacity-corrected rotation temperature $T_{\text{rot},p}$ ($p=\text{HC, mm2, mm3a, mm3b, NE}$) of each substructure (red fittings in Panels 2-6 of Figure 8):

- (1) Obtain the rotation temperature $T_{1,p}$ from weighted least squares fit to Boltzmann diagram, assuming that all the p-type CH_3CN lines are optically thin (see fit to the black dots in Panels 2-6 of Figure 8);
- (2) Estimate the optical depth of CH_3CN ($12_2 \rightarrow 11_2$) $\tau_{K,1}$ (K=2) by comparing its main beam temperature with that of $\text{CH}_3^{13}\text{CN}$ ($12_2 \rightarrow 11_2$), and calculate the column density of line $12_2 \rightarrow 11_2$ at $T_{1,p}$ with the optical depth correction. Then, estimate the total column density of CH_3CN as $N_{1,p}$ assuming LTE (see Section 4.2 for more details about the correction);
- (3) With $T_{1,p}$ and $N_{1,p}$ as trial input parameters, estimate the optical depth for the remaining transitions in the CH_3CN ladder $\tau_{K,1}$ (K=0–8) with the RADEX code package¹⁸ (van der Tak et al. 2007), then correct their column densities line by line (dots and triangles in red in Figure 8) and obtain a new rotation temperature $T_{2,p}$;
- (4) Repeat step (2)–(3) until $(|T_{n,p} - T_{n-1,p}|)/T_{n-1,p} \leq 10\%$ ($n=2,3,\dots$; see fittings in red in Figure 8).

¹⁸ RADEX is a one-dimensional non-LTE radiative transfer code, providing an alternative to the widely used rotation diagram method. Without requiring the observation of many optically thin emission lines, it can be used to roughly constrain the excitation temperature in addition to the column density.

¹⁷ The K = 9 line is blended by strong ^{13}CO ($2 \rightarrow 1$) emission.

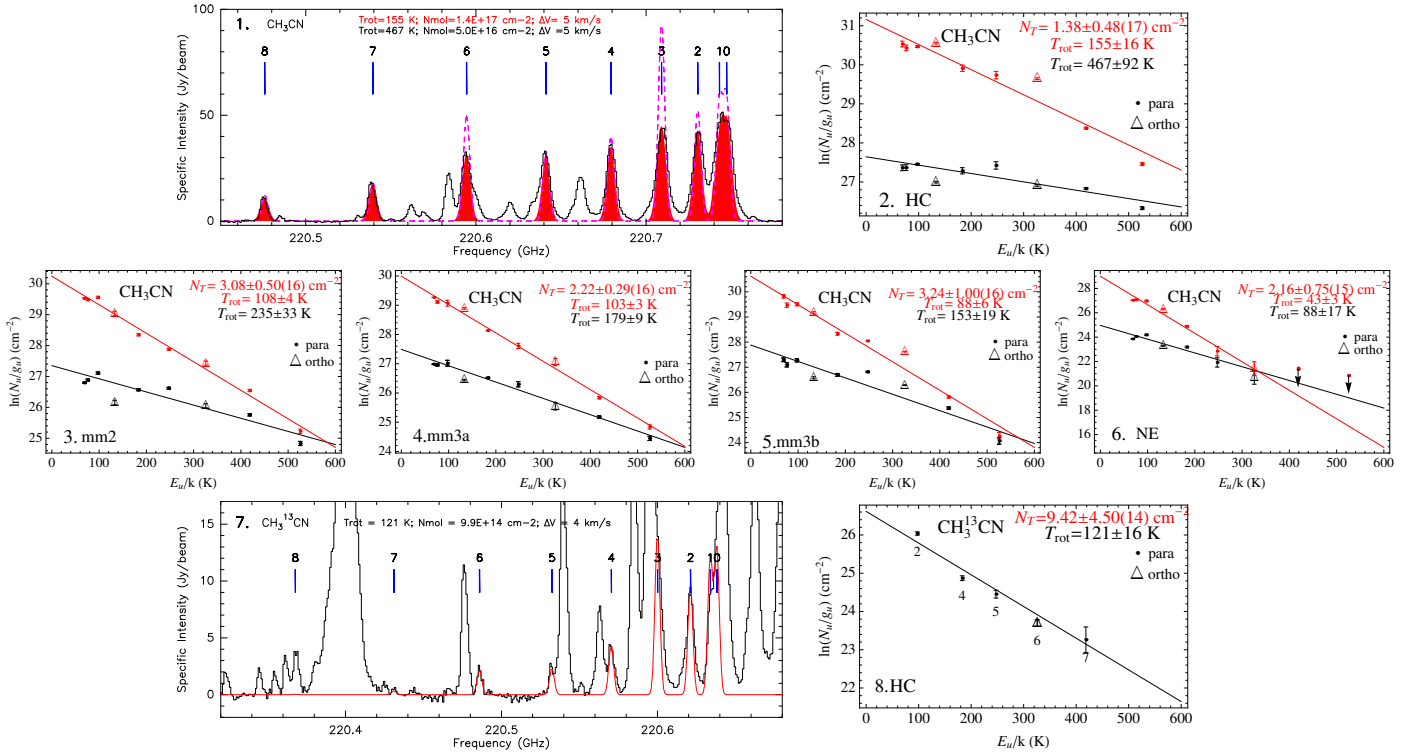


Fig. 8: Panel 1): CH_3CN spectrum towards the HC in black, LTE model fit in dashed purple, and fitting with optical depth correction in filled red. Panels 2-6): rotation diagram of CH_3CN derived for each substructure, with dots for p- CH_3CN and triangles for o- CH_3CN . Black fittings are only for the p-lines when assuming they are optically thin, and red fittings are for both o- and p- lines by optical depth correction. Panel 7): $\text{CH}_3^{13}\text{CN}$ spectrum towards the HC in black and the LTE model fit in red. Panel 8): rotation diagram of $\text{CH}_3^{13}\text{CN}$ in HC with black dots (p-) and triangles (o-) from observation, and fitting is o-lines excluded by assuming lines are optically thin. For lines without detection, an upper limit equal to the 3σ rms is shown as arrow. The estimated temperature and total column density from each fitting is indicated in each panel. Errors are derived from scatter in the data points.

The above approach¹⁹ can be applied to sources HC, mm2 mm3a, mm3b, and NE, where the CH_3CN ladders and $\text{CH}_3^{13}\text{CN}$ ($12_2 \rightarrow 11_2$) can be clearly detected²⁰. In SR and OF1N(S), the CH_3CN lines are below the 3σ detection threshold, so we assume the rotation temperature in these positions to be the same as that in NE.

4.1.2. HCOOCH_3 , CH_3OH , and $^{34}\text{SO}_2$

HCOOCH_3 has the largest number of lines detected in our dataset. From satisfactory synthetic fitting (especially for lines in the torsionally excited state $\nu = 1$, Figure A2), we can reasonably assume that most of its lines are optically thin. Line emissions from this species are not contaminated by N-bearing species owing to their different spatial distributions, so we use them to derive a second set of temperatures.

On the other hand, CH_3OH and H_2^{13}CO have an unusual spatial distribution (dual peaks/extended emissions at both HC

and mm3a(b), and tail towards the SE), which may be affected by their different temperatures. Since multiple transitions of CH_3OH are available in our data, we can use them to derive a third temperature set.

For S-bearing species, their extended emission indicates they may be sensitive to the ambient shock environment, so their temperature in each substructure may be different from the other species. However, in our data, some of the S-bearing species have only a single transition (O^{13}CS , ^{13}CS), and other lines may not be optically thin (SO_2 , SO , and OCS). Because $^{34}\text{SO}_2$ is the only S-bearing rare isotopologue that has multiple transitions in our observations, we applied temperatures derived from transitions of $^{34}\text{SO}_2$ to the other S-bearing species.

Using the lines list in Table A3, we derived the rotation temperatures in each substructure from HCOOCH_3 , CH_3OH , and $^{34}\text{SO}_2$ (Figures 9I–III) and list these temperature sets in bold face in Table 3. Temperatures derived from HCOOCH_3 lines in the ground and torsionally excited states separately have some differences, but they do not deviate significantly from temperatures derived from all of its lines. Therefore, we use the “mixed” temperatures in the end.

¹⁹ In reality, molecules do not distribute homogeneously in the clouds, and they are far from being homogeneous in density and temperature. The ultimate best-fit requires a sophisticated, fully 3Dnd physico-chemo-LRT modelling, which is beyond the scope of our paper. Our iterative approach is between realism and feasibility of the modelling, which fits both o-/p- CH_3CN well.

²⁰ The detection of $\text{CH}_3^{13}\text{CN}$ ($12_2 \rightarrow 11_2$) in NE is 4σ .

4.1.3. The other organics

In addition, since different organic molecules have specific spatial distributions, we also derive the rotation temperatures for the species that have multiple transitions with significantly different E_u/k_B detected in our dataset (Figures 9IV–VI, listed in Table A3). In the condensations HC, mm2, mm3a, and mm3b, rotation temperatures of HNCO are similar to those derived from CH_3CN within uncertainties; and rotation temperatures derived from CH_3OCH_3 and $\text{CH}_3\text{CH}_2\text{OH}$ are close to HCOOCH_3 ($\nu = 1$) within uncertainties. Therefore, temperature sets from CH_3CN and HCOOCH_3 are applicable to the rest N- and O-bearing species (including simple molecules and COMs) in estimating their column densities.

Although temperatures derived from different species at the same substructure vary, HC is consistently the warmest substructure, while mm2, mm3a, and mm3b are slightly cooler. In the outflow regions, there are no sufficiently strong lines for species other than CH_3CN to derive the temperature, which may suggest these regions are cooler, exhibiting similar chemical properties.

4.2. Column densities

4.2.1. Molecular column densities

For all the species we detected, we calculate their column densities (from both main and rare isotopologues) from the integrated spectral line intensities as below.

The optical depth τ_ν (in velocity) along the line of sight is (Zeng et al. 2006, Eq. A.25):

$$\tau_\nu = \frac{c^3}{8\pi\nu^3} A_{ul} N_u (e^{\frac{h\nu}{k_B T_{\text{rot}}}} - 1) \Phi(\nu). \quad (1)$$

where c is the speed of light, k_B the Boltzmann constant, h the Planck constant, ν the line rest frequency, $\Phi(\nu)$ the distribution function of the line shape in terms of velocity ν . Here, A_{ul} is the average spontaneous emission rate from the upper state E_u into the lower state E_l , and it is calculated from line strength S_{ul} and dipole moment μ as

$$A_{ul} = \frac{64\pi^4 \nu^3}{3hc^3} \frac{S_{ul} \mu^2}{g_u} \quad (2)$$

After integrating the optical depth over the observed linewidth, $\int \Phi(\nu) d\nu = 1$, and the column density N_u of the line at ν Hz is

$$N_u = \frac{8\pi\nu^3}{c^3 A_{ul}} \frac{1}{\exp(\frac{h\nu}{k_B T_{\text{rot}}}) - 1} \int \tau_\nu d\nu. \quad (\text{cm}^{-2}) \quad (3)$$

When assuming LTE, the total column density of all transitions for a molecule α is

$$N_{T,\alpha} = \frac{N_u}{g_u} Q(T_{\text{rot}}) e^{\frac{E_u}{k_B T_{\text{rot}}}} \quad (\text{cm}^{-2}) \quad (4)$$

where $Q(T_{\text{rot}})$ is the partition function for the given (rotational) excitation temperature of each sources, which is interpolated from a table of partition functions for fixed temperatures, obtained from CDMS/JPL.

Here, $S_{ul} \mu^2$ can be calculated from CDMS/JPL line intensity $\ell(T_{\text{rot}})$ (Pickett et al. 1998),

$$S_{ul} \mu^2 = \frac{3hc}{8\pi^3 \nu} \ell(T_{\text{rot}}) Q(T_{\text{rot}}) (e^{-\frac{E_l}{k_B T_{\text{rot}}}} - e^{-\frac{E_u}{k_B T_{\text{rot}}}})^{-1} \quad (5)$$

$$= 2.4025 \times 10^{10} \left[\frac{\nu}{\text{Hz}} \right]^{-1} \left[\frac{\ell(300\text{K})}{\text{nm}^2 \text{MHz}} \right] Q(300\text{K}) \times [e^{-\frac{E_l}{k_B 300\text{K}}} - e^{-\frac{E_u}{k_B 300\text{K}}}]^{-1} \text{Debye}^2 \quad (6)$$

For the emission lines, we assume the Rayleigh-Jeans approximation ($\frac{h\nu}{k_B T_{\text{rot}}} \ll 1$) is valid, therefore Eqs. 3 and 4 can be simplified as (Zeng et al. 2006, Eq. 4.26, also see Wilson et al. 2009),

$$\frac{N_u}{g_u} \cong \frac{3k_B}{8\pi^3 \nu S_{ul} \mu^2} T_{\text{rot}} \int \tau_\nu d\nu \quad (\text{cm}^{-2}) \quad (7)$$

$$N_{T,\alpha} = \frac{k_B}{hc} \frac{(e^{\frac{h\nu}{k_B T_{\text{rot}}}} - 1)}{\ell(T_{\text{rot}})} T_{\text{rot}} \int \tau_\nu d\nu \quad (\text{cm}^{-2}) \quad (8)$$

Assuming that the observed emission in each substructure is homogeneous and fills the combined beam, the integration of measured main beam brightness temperature within the velocity range $\int T_B(\nu) d\nu$ can be substituted for the last term in the above equation:

$$T_{\text{rot}} \int \tau_\nu d\nu \cong \frac{\tau_{\alpha,0}}{1 - e^{-\tau_{\alpha,0}}} \int T_B(\nu) d\nu \quad (\text{K cm s}^{-1}) \quad (9)$$

where $\tau_{\alpha,0}$ is the optical depth at line centre, and $\int T_B(\nu) d\nu$ is measured from Gaussian/hyperfine structure (HFS) fitting by using Gildas software package.

The column densities and related uncertainties of species listed in Table 3 (CH_3CN ($\text{CH}_3^{13}\text{CN}$), HNCO, HCOOCH_3 , CH_3OH , CH_3OCH_3 , $\text{CH}_3\text{CH}_2\text{OH}$, and $^{34}\text{SO}_2$) can be estimated directly from their rotation diagrams and the scatterings of the data points (Figure 9). For the species whose transitions are not sufficient to derive the rotation diagrams, we estimate their column densities by assuming that transitions of related species have the same T_{rot} :

- N-bearing species have similar temperatures to those derived from the opacity-corrected CH_3CN ,
- S-bearing species have similar temperatures to $^{34}\text{SO}_2$,
- O-bearing species have similar temperatures to HCOOCH_3 ,
- Given the similarly unusual spatial distribution between H_2^{13}CO and CH_3OH , we also estimate the column densities of H_2^{13}CO at temperatures derived from CH_3OH .

In general, we assume that the observed transitions are optically thin ($\tau_{\alpha,0} \leq 1$, $\frac{\tau_{\alpha,0}}{1 - e^{-\tau_{\alpha,0}}} \approx 1$). However, for several molecules with large abundances, we observe the corresponding transitions of their main and rare isotopologues, e.g., OCS ($J = 19 \rightarrow 18$)- O^{13}CS ($19 \rightarrow 18$), ^{13}CO ($2 \rightarrow 1$)- CO ($2 \rightarrow 1$)- C^{18}O ($2 \rightarrow 1$) and $\text{CH}_3^{13}\text{CN}$ ($12_2 \rightarrow 11_2$)- CH_3CN ($12_2 \rightarrow 11_2$). By measuring the ratio between main beam brightness temperature of the main line $T_{B,\alpha,0}$ and its rare isotopologue $T_{B,\beta,0}$, we can estimate the optical depth at line centre of a given transition $\tau_{\alpha,0}$ (Myers et al. 1983):

$$\frac{1 - \exp(-\tau_{\alpha,0}/\mathfrak{R}^\alpha)}{1 - \exp(-\tau_{\alpha,0})} \approx \frac{T_{B,\beta,0}}{T_{B,\alpha,0}} \quad (10)$$

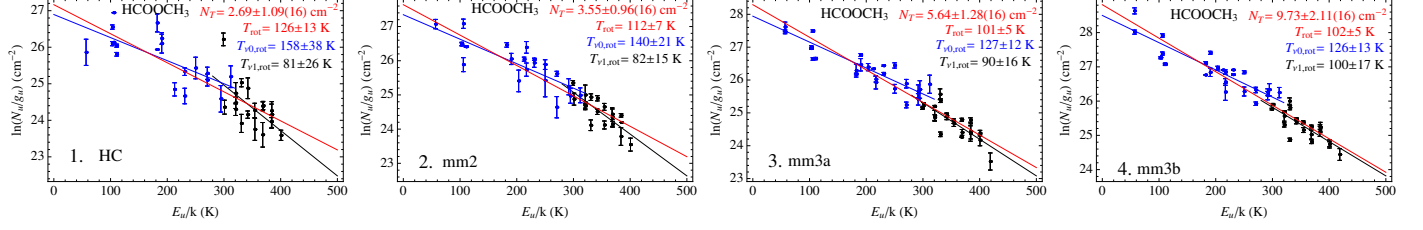
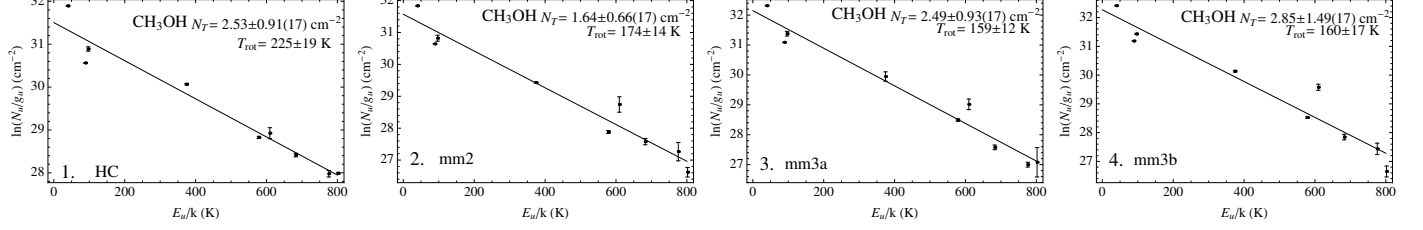
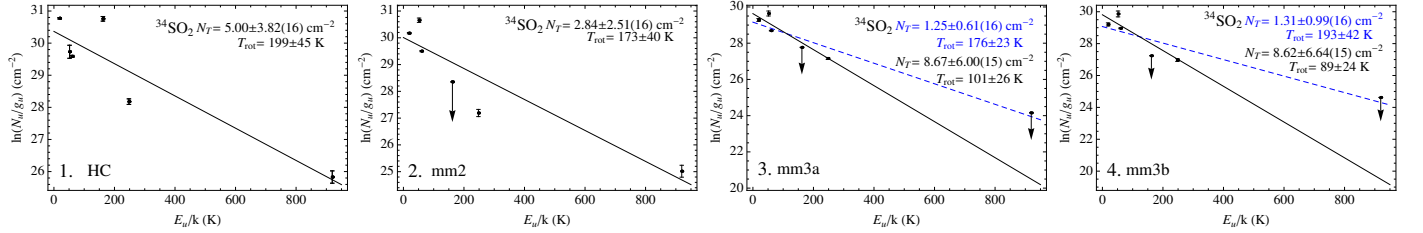
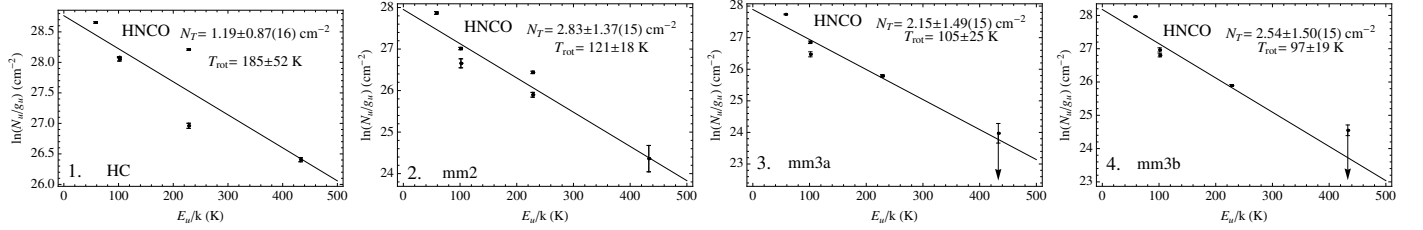
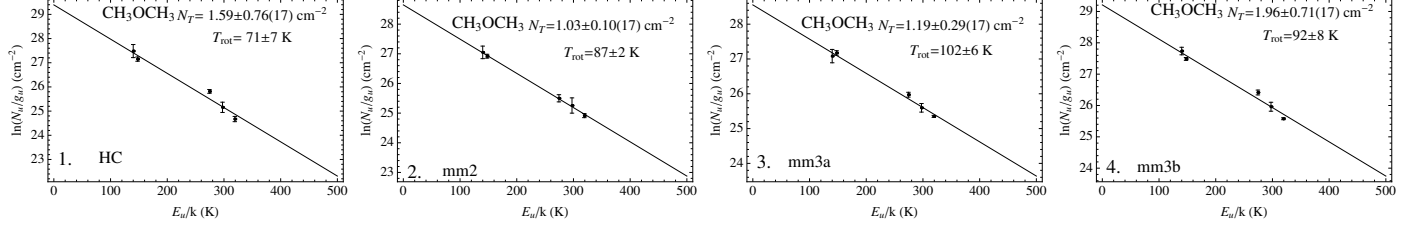
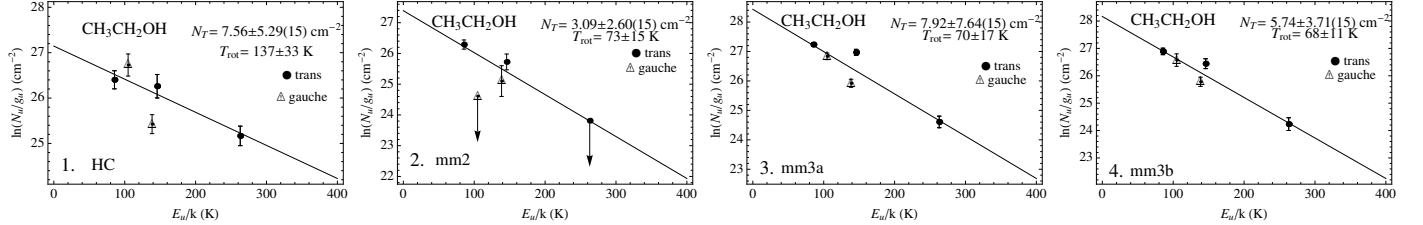
I. HCOOCH_3

 II. CH_3OH

 III. $^{34}\text{SO}_2$

 IV. HNCO

 V. CH_3OCH_3

 VI. $\text{CH}_3\text{CH}_2\text{OH}$


Fig. 9: Rotation diagrams of the N-, O-, and S-bearing species with multiple unblended transitions detection in HC, mm2, mm3a, and mm3b. Panels in Row I show two states of HCOOCH_3 lines, with the blue and black dots from observation of ground state ($v = 0$) and torsionally excited state ($v = 1$) lines, respectively. With the optically thin assumption, fittings for each state are plotted in blue or black, respectively, and fittings for all the transitions are plotted in red. Non-detection of HCOOCH_3 lines are not shown. Panels in Row II–VI show fittings with the optically thin assumption, with 3σ upper limits from non-detections plotted as arrows. Blue dashed lines in Row III are fittings with upper limits included. The estimated temperature and total column density from each fitting is indicated in each panel. Errors are derived from scatters in the data points.

Species	HC (K)	mm2 (K)	mm3a (K)	mm3b (K)	NE (K)
CH₃CN	155 ± 16	108 ± 4	103 ± 3	88 ± 6	43 ± 3
CH ₃ ¹³ CN	121 ± 16	–	–	–	–
HNCO	185 ± 52	121 ± 18	105 ± 25	97 ± 19	–
HCOOCH₃	126 ± 13	112 ± 7	101 ± 5	102 ± 5	–
CH₃OH	225 ± 19	174 ± 14	159 ± 12	160 ± 17	–
CH ₃ OCH ₃	71 ± 7	87 ± 2	102 ± 6	92 ± 8	–
CH ₃ CH ₂ OH	137 ± 33	73 ± 15	70 ± 17	68 ± 11	–
³⁴SO₂	199 ± 45	173 ± 40	101 ± 26	89 ± 24	–

Table 3: Rotation temperature sets for each substructure derived from species, each of which has > 4 transitions with significantly different E_u/k_B detected in our data. The substructures where there are not enough sufficient lines to derive the rotation temperatures are denoted by “–”. Temperatures in bold face are used to estimate the column densities and abundances of species whose rotation diagrams are unable to be derived.

where \mathcal{X}_α is the intrinsic abundance of the main isotope (e.g., ¹²C) compared to its rare isotope (e.g., ¹³C) in the ISM (Table 4, e.g., Wilson & Rood 1994; Chin et al. 1996).

Using the above method, we calculate the column densities of 25 isotopologues (for both optically thin and thick cases) in each substructure, and present them in Tables A5I, A6I and A7I. In Table 4, we list the transitions for which we corrected their optical depths. We found that CO (2 → 1), OCS (19 → 18), and CH₃CN (12₂ → 11₂) are significantly optically thick ($\tau = 6 - 117$) in all substructures where they are detected. The validity of the assumption that the remaining molecular lines are optically thin is discussed in Section 4.4.

In addition, the main emission peak(s) of some COMs (CH₃COCH₃, CH₃CH₂OH, CH₂CHCN, C₆H, and HC₇N) do not strictly coincide with either of the continuum peaks. In determining their column densities at their main emission peaks, we use their strongest transitions (shown in Figure 5) and the temperature from an adjacent substructure. Lines are assumed to be optically thin, and molecular column densities could be underestimated if this assumption is incorrect, so the lower limits are given in Table 2.

4.2.2. H₂ column densities

In Orion-KL, at 1.3 mm wavelength, the continuum emission is dominated by dust-neutral gas emission (Beuther et al. 2004). Assuming the dust emission at mm wavelengths is optically thin and coupled with the gas, which has a single excitation temperature, $T_{\text{ex}} \sim T_{\text{rot}} = T_{\text{dust}}$ (Hildebrand 1983), we use the SMA-only data to calculate the H₂ column densities for different substructures, according to Schuller et al. (2009) :

$$N_{\text{H}_2} = \frac{I_\nu R}{B_\nu(T_{\text{dust}}) \Omega_a \kappa_\nu \mu m_H} \quad (\text{cm}^{-2}) \quad (11)$$

where I_ν is the peak specific intensity for each substructure on the continuum (in Jy beam⁻¹, taken to be the 3 σ upper limit in the outflow regions); R is the isothermal gas to dust mass ratio (taken to be 150, from Draine 2011); $B_\nu(T_{\text{dust}})$ is the Planck function for a dust temperature T_{dust} ; Ω_a is the solid angle of the SMA beam (in rad²); $\kappa_\nu = 1.0 \text{ cm}^2 \text{ g}^{-1}$ is the dust absorption coefficient at 1.3 mm (assuming a model of agglomerated grains with thin ice mantles²¹ for densities 10⁷ cm⁻³ (Blake et al.

1987), extrapolated from Ossenkopf & Henning (1994); μ is the mean molecular weight of the ISM, which is assumed to be 2.33; and m_H is the mass of an hydrogen atom (1.67×10^{-24} g). The results are reported in column $N_{\text{H}_2,1}$ of Table 1.

From the SMA-only observations, the total continuum flux at 1.3 mm is 22.6 Jy. However, extrapolating the flux S_ν from existing SCUBA data (Di Francesco et al. 2008) at 450 μm (28 700 Jy) and 850 μm (2 090 Jy), the total flux should be closer to ~ 400 Jy at 1.3 mm (assuming $S_\nu \propto \nu^4$, Johnstone & Bally 1999). The difference implies that > 90% of the flux has been filtered out by the SMA observations. In contrast, C¹⁸O (2 → 1) from a combination of 30 m and SMA observations is detected towards all the substructures, and it should not suffer from the same spatial filtering as the SMA-only continuum data. As a result, it is a more reliable probe of the total column density of gas in the cloud at all spatial scales. Moreover, as a rare isotopologue line, it can be reasonably assumed to be optically thin, so we use it to make a second independent estimation of the H₂ column density in all the substructures. By assuming a constant abundance in all substructures $\frac{N_{\text{C}^{18}\text{O}}}{N_{\text{H}_2}} = \frac{N_{\text{C}^{18}\text{O}}}{N_{\text{CO}}} \frac{N_{\text{CO}}}{N_{\text{H}_2}} \sim \frac{10^{-4}}{560} \sim 1.79 \times 10^{-7}$ (Wilson & Rood 1994), H₂ column densities can be calculated from the column densities of optically thin C¹⁸O emission (reported in the column $N_{\text{H}_2,2}$ of Table 1).

4.3. Molecular abundances

Subsequently, to study the chemical properties on the small scale of Orion-KL, we derived the molecular abundances with respect to H₂ (converted from C¹⁸O) in each substructure (Tables A5II, A6II, and A7II).

Figure 10 presents the molecular column density and the abundance of each species with respect to $N_{\text{H}_2,2}$. Generally, all the molecules have higher column densities in the central condensations (HC, mm2, mm3a, and mm3b) than the extended regions in the outflows (NE, SR, OF1N, and OF1S). While the abundances of some species have relatively small variations among the substructures (e.g., SO, CO, C¹⁸O, and ¹³CO), some vary substantially. Specifically, N-bearing species are

temperature at different radii, so ice may not be completely evaporated. Therefore, without knowing the real geometry of the source, we assume the dust absorption coefficient according to the “thin ice mantle” case. Moreover, this assumption is consistent with the modelling result in Gerner et al. (2014). In the extremely case, if we assume the ice is completely evaporated, the H₂ column density derived from continuum will be 2–4 times lower than our current estimation.

²¹ At around 100–150 K, water ice starts to be evaporated. However, in the line of sight, the envelope of the protostar may not have the same

significantly underabundant in the SR and the outflow regions; O-bearing organic molecules containing ≤ 6 atoms (e.g., H_2^{13}CO , CH_2CO , CH_3OH) have more extended emission across all the substructures, with nearly constant large abundances in all the substructures except for NE. The S-bearing molecules are an intermediate case: most of them are not detected in the high-velocity outflow, but are clearly detected in NE (OCS , SO_2 , $^{34}\text{SO}_2$, ^{13}CS) and (or) the SR (SO), with lower abundance. Such abundance differentiation among species is consistent with the spatial differentiation shown in Figure 4.

4.4. Error budget

In this section, we consider the effect that the various assumptions that we made in our quantitative analysis have on the results presented in this paper.

1. T_{rot} (rotation temperature): The traditional rotation diagram method is subject to a number of uncertainties owing to various assumptions, e.g. line emission is assumed to be optically thin and LTE is assumed to apply (see discussion in Snyder et al. 2005; Herbst & van Dishoeck 2009). If these assumptions are valid, the points on the population diagram will be well-fit by a straight line, with the slope proportional to the negative reciprocal of the temperature. However, this is not the case (see Figure 8). According to Table 2, the column density in each substructure is $\sim 10^7 \text{ cm}^{-2}$ (assuming a source size ~ 10 times of the beam size, see also Blake et al. 1987; Plume et al. 2012), so LTE can be a reasonable assumption (except for such extreme cases as masing and sub-/super thermal excited conditions), and the main reason for the fittings with uncertainties is the optical depth of the used lines.

(1) In Section 4.1.1, we obtain the optical depth of CH_3CN ($12_2 \rightarrow 11_2$) by comparing its observed main beam brightness temperature to that of $\text{CH}_3^{13}\text{CN}$ ($12_2 \rightarrow 11_2$). Then, we use this optical depth as a standard in non-LTE radiative transfer fitting and derive a lower T_{rot} in each substructure. In the HC, the rotational temperatures derived from CH_3CN ($155 \pm 16 \text{ K}$) and $\text{CH}_3^{13}\text{CN}$ ($121 \pm 16 \text{ K}$) are slightly different, but they agree within the uncertainties, and column densities of N-bearing species are insensitive to temperature uncertainties of this magnitude (Table A6I). On the other hand, temperatures derived from HNCO agree with the above T_{rot} within the uncertainties, so our approach should be applicable.

(2) In Section 4.1.2, T_{rot} for most O-bearing species are assumed to be similar to those derived from HCOOCH_3 . In general, the temperatures derived from two different states of HCOOCH_3 lines are consistent, while the torsionally excited HCOOCH_3 ($\nu = 1$) lines appear to trace lower temperatures than lines in the ground state ($\nu = 0$), because LTE assumption may not be applied in sub-thermal conditions (see also Demyk et al. 2008). In addition, we derived a third temperature set from CH_3OH , which is in general higher than those derived from HCOOCH_3 , CH_3OCH_3 , and $\text{CH}_3\text{CH}_2\text{OH}$. Synthetic spectrum fitting (Figure A2) indicates that some lines of CH_3OH may be optically thick, which may explain the higher measured T_{rot} . On the other hand, CH_3OH lines have broader line widths ($\sim 5 - 7 \text{ km s}^{-1}$) than HCOOCH_3 lines ($\sim 3 - 5 \text{ km s}^{-1}$) in

the central condensations, implying that they trace gas with different temperatures.

(3) For S-bearing species, T_{rot} derived from $^{34}\text{SO}_2$ varies from HC through mm2 to mm3a and mm3b. However, detected lines in mm3a and mm3b are not sufficient to derive a reliable temperature, because we lose the constraint of fittings from the non-detection line with high E_u/k_B at 229.987 GHz (Figure 9III). Nevertheless, we estimate the temperature upper limits for both substructures by including the non-detected lines (dashed blue fittings), and find the differences for column densities derived at temperatures from 89-101 K (non-detection are excluded in fittings) to 176-193 K (upper limits, columns in italic font in Table A7I) are by a factor of < 3 . The insensitivity of S-bearing column densities to this temperature regime may also explain the slightly higher T_{rot} with large uncertainties in HC and mm2.

2. N_T (molecular column density): In Section 4.2, we first assume that all the identified molecular lines are optically thin. Then, we use Eq. 10 to obtain the optical depth of those main isotopologue lines whose rare isotopologue lines with the same transition are detected. Finally, using Eq. 9, we correct the column density of the main isotopologue. In this approach, by assuming the rare isotopologue lines are optically thin, we list the optical depths and abundance ratios for ^{13}CO ($2 \rightarrow 1$), CO ($2 \rightarrow 1$), OCS ($19 \rightarrow 18$), and CH_3CN ($12_2 \rightarrow 11_2$) with respect to the corresponding rare isotopologue lines with and without optical depth correction in Table 4.

However, Eq. 9 is based on the assumption that the main and rare isotopologue lines have the same excitation temperature, which is often not the case. Therefore, a more accurate calculation requires the large velocity gradient (LVG) approach and proper chemical modelling. Nevertheless, our analytic calculations suggest that, the optical depth is the main situation driving the error in the estimated molecular column density. For abundant molecules such as CH_3OH , HNCO , SO , and SO_2 , where we do not observe a corresponding transition of their rare isotopologues, our assumption that their lines are optically thin may result in underestimating their column densities by a factor of 7-10 (coming from the average differences for OCS , CO , and CH_3CN column density values before and after optical depth correction in Figure 10).

Aside from the optical depth, the errors also come from our assumption of LTE. Assuming that the transitions of one species have ideal Boltzmann distributions at the same T_{rot} , molecular total column density can be derived from one transition. However, as represented by points on their rotation diagrams, multiple transitions of certain species (e.g., $^{34}\text{SO}_2$, HNCO , and $\text{CH}_3\text{CH}_2\text{OH}$, Figure 9) show wide scatter, indicating that uncertainties in the estimation of T_{rot} lead to the over-/under-estimation of the total column densities by a factor of 0.5–2 (bold face in Tables A5I, A6I, and A7I). For the species whose total column densities are not able to be estimated from rotation diagram fittings owing to the lack of sufficient transitions, our LTE assumption (using Eq. 4) may also result in the under/over-estimation of their total column densities of the same magnitude.

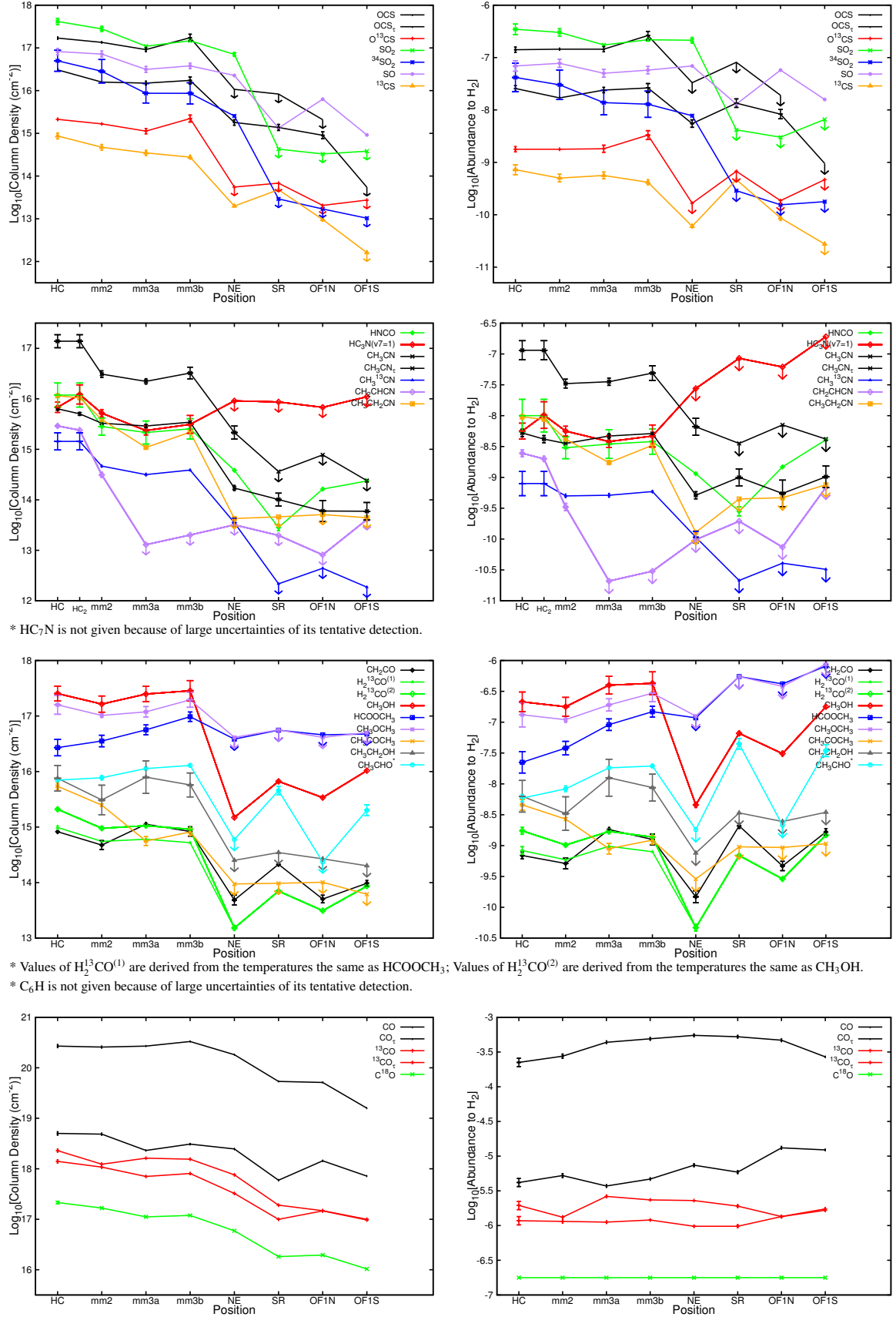


Fig. 10: Molecular column densities (panels in the left column) and abundances (panels in the right column) towards 8 positions in Orion-KL. The molecular abundances of each species with respect to H_2 are converted from C^{18}O , assuming a constant $N_{\text{C}^{18}\text{O}}/N_{\text{H}_2} \sim 1.79 \times 10^{-7}$ ratio. Column densities and abundances with the uncertainties are measured as mentioned in Section 4.4 and Tables A5–A7. Coloured solid lines show the differentiation for each isotopologue calculated from optically thin assumption (arrows highlight the upper limits), while dashed lines show the differentiation calculated with optical depth correction from Eq. 10. For abundant molecules (e.g., HNCO , SO , SO_2 , CH_3OH) which we have not measured their line optical depths, their densities could be underestimated by a factor of 7–10.

Species	\mathcal{R}_α	HC	mm2	mm3a	mm3b	NE	S	OF1N	OF1S
$\tau_{\text{CO}} (2 \rightarrow 1)$		54	53	117	107	74	90	36	22
$\text{NCO}_7/\text{N}_{\text{C}^{18}\text{O}}$	\dagger 560 ± 25	$1263.0_{\pm 21.8}$	$1541.0_{\pm 57.1}$	$2422.0_{\pm 46.6}$	$2765.0_{\pm 72.3}$	$3100.0_{\pm 52.9}$	$2934.0_{\pm 18.8}$	$2640.0_{\pm 33.7}$	$1517.0_{\pm 29.8}$
$\text{NCO}/\text{N}_{\text{C}^{18}\text{O}}$	\star	$23.4_{\pm 0.4}$	$29.1_{\pm 1.1}$	$20.7_{\pm 0.4}$	$25.8_{\pm 0.7}$	$41.9_{\pm 0.7}$	$32.6_{\pm 0.2}$	$73.3_{\pm 0.9}$	$68.9_{\pm 1.4}$
$\tau_{^{13}\text{CO}} (2 \rightarrow 1)$		1.1	0.25	2	1.5	2	1.5	0.02	0.08
$\text{N}_{^{13}\text{CO}_7}/\text{N}_{\text{C}^{18}\text{O}}$	\dagger 7.2 ± 0.9	$10.8_{\pm 0.2}$	$7.3_{\pm 0.2}$	$14.6_{\pm 0.2}$	$13.1_{\pm 0.2}$	$12.8_{\pm 0.0}$	$10.6_{\pm 0.0}$	$7.6_{\pm 0.0}$	$9.7_{\pm 0.3}$
$\text{N}_{^{13}\text{CO}}/\text{N}_{\text{C}^{18}\text{O}}$	\star	$6.5_{\pm 0.1}$	$6.5_{\pm 0.2}$	$6.3_{\pm 0.1}$	$6.8_{\pm 0.1}$	$5.5_{\pm 0.0}$	$5.5_{\pm 0.0}$	$7.5_{\pm 0.0}$	$9.3_{\pm 0.3}$
$\tau_{\text{OCS}} (19 \rightarrow 18)$		5.5	8.5	6	10	≤ 6	≤ 6	≤ 2	--
$\text{NOCS}_7/\text{N}_{\text{O}^{13}\text{CS}}$	\dagger 77 ± 7	$79.7_{\pm 0.7}$	$81.1_{\pm 2.0}$	$80.1_{\pm 3.0}$	$78.2_{\pm 0.0}$	≤ 195.2	≤ 121.3	≤ 101.1	--
$\text{NOCS}/\text{N}_{\text{O}^{13}\text{CS}}$	\star	$14.4_{\pm 0.1}$	$9.5_{\pm 0.2}$	$13.3_{\pm 0.5}$	$7.8_{\pm 0.0}$	≥ 32.4	≥ 20.2	≥ 43.7	--
$\tau_{\text{CH}_3\text{CN}} (12_2 \rightarrow 11_2)$		18	11	8.5	9	17	≤ 3.5	≤ 13	≤ 4
$\text{N}_{\text{CH}_3\text{CN}_7}/\text{N}_{\text{CH}_3^{13}\text{CN}}$	\dagger 77 ± 7	$79.6_{\pm 3.0} (76.6_{\pm 2.4})^*$	$77.7_{\pm 3.1}$	$78.1_{\pm 1.9}$	$79.8_{\pm 0.3}$	$82.3_{\pm 6.7}$	≤ 168.3	≤ 176.3	≤ 130.0
$\text{N}_{\text{CH}_3\text{CN}}/\text{N}_{\text{CH}_3^{13}\text{CN}}$	\star	$4.4_{\pm 0.2} (4.3_{\pm 0.1})^*$	$7.1_{\pm 0.3}$	$9.2_{\pm 0.2}$	$8.9_{\pm 0.0}$	$4.8_{\pm 0.4}$	≥ 46.6	≥ 13.6	≥ 31.9

* Ratio at temperature derived from $\text{CH}_3^{13}\text{CN}$.

Table 4: Optical depth and abundance ratios for CO, ^{13}CO , OCS, and CH_3CN with respect to their rare isotopologues in each substructure of Orion KL. The values are derived from the single strongest transition of each species using Eqs. 3 and 4. \dagger or \star mark the estimations with or without optical depth correction. “ \geq (\leq)” come from the 3σ limit of the non-detection of O^{13}CS (OCS) and $\text{CH}_3^{13}\text{CN}$. The ratios between isotopes \mathcal{R}_α of $^{12}\text{C}/^{13}\text{C}$ and $^{16}\text{O}/^{18}\text{O}$ are provided from the local ISM ratio measured in Wilson & Rood (1994). Uncertainties on the measured values are typically $\leq 10\%$ (written as the subscript), as determined from T_{rot} , partition function $Q(T_{\text{rot}})$, and $\int T_{\text{B}}(v)dv$ of the transition.

In addition, $\int T_{\text{B}}(v)dv$ measured from Gaussian/HFS fittings brings on average $< 10\%$ uncertainties (Table A4), which is negligible compared to the chemical differentiation amongst the substructures (written as the subscript in Tables A5I, A6I, and A7I).

3. N_{H_2} and molecular abundance: Because no continuum information is available from the combined data, we used two methods to calculate the column density of H_2 (Table 1): from SMA-only continuum ($\text{N}_{\text{H}_2,1}$) and from SMA-30 m C^{18}O ($\text{N}_{\text{H}_2,2}$). The molecular abundances were derived with respect to $\text{H}_{2,2}$. Comparing the column density of $\text{H}_{2,1}$ and $\text{H}_{2,2}$, we found $\text{N}_{\text{H}_2,2}/\text{N}_{\text{H}_2,1}$ is ~ 0.9 in mm2, ~ 0.5 in mm3a and mm3b, ~ 0.4 in HC^{22} , ~ 0.2 in NE, but 0.1 in SR. Several reasons may lead to such difference: (1) the specific intensity (Jy beam^{-1}) used to calculate the column density depends on the beam. The combined beam is larger than the SMA-only beam by a factor of ~ 2.5 , so it is reasonable that for larger beam size, we obtain lower H_2 column density (similar case in Beuther et al. 2007a). (2) In producing the continuum, we select the “line-free” part, but there are still lines with low emission (Figure A2), which may contaminate the continuum; (3) we simply assume that the gas-to-dust ratio and the volume densities in all substructures are similar within an order of magnitude (~ 150 , $\sim 10^7 \text{ cm}^{-3}$), hence also the dust opacity. Since we do not know the size of each substructure, gas is possibly much denser in a warmer source (HC, mm2, mm3a, and mm3b) than in the other cooler substructures (NE, SR), so the homogeneous volume density assumption may not be accurate in the whole region. (4) Grain growth in the envelopes can also be a reason for difference in dust emissivity from centre to extended substructures at (sub-)mm (Miotello et al. 2014). (5) We also note that C^{18}O column density in the central region is a factor of 30 higher than in the outflow. Judging that $\text{N}_{\text{H}_2,2}$ is derived with the assumption that $\text{N}_{\text{C}^{18}\text{O}}/\text{N}_{\text{H}_2} = \text{const.}$ in all the studied substructures, the variation of $\text{N}_{\text{C}^{18}\text{O}}/\text{N}_{\text{H}_2}$ ratio in different substructures can

be another factor that leads to error in our estimation.

4. In addition, another simplification in our calculation is an assumed constant beam-filling factor. Determination of molecular abundances in Orion-KL substructures relies upon an accurate source structure model for each molecule. When the source is smaller than the beam size, the main beam brightness temperature is diluted, leading to an underestimated brightness temperature for more compact structures. To correct this, an appropriate correction factor needs to be applied. Since we do not know the accurate sizes of the substructures, we simply assume that the filling factor is unity in all the calculations.

5. Discussion

These observations comprise a large set of molecular lines (over 160 lines from 20 species, including 25 isotopologues) from combined SMA and IRAM 30 m data towards Orion-KL. Resolving Orion-KL into eight substructures and comparing S-, N-, and O-bearing molecules, we find complicated spatial morphologies for COMs and strong chemical differentiation over the observed substructures.

5.1. Comparison with the other results

Previous quantitative studies of Orion-KL mainly focused on the HC, CR (with mm3a and mm3b treated as a single substructure), and plateau (OF1N, OF1S), therefore comparison of our estimated molecular abundances with previous results is limited to these substructures.

1. Since different molecules have different chemistry, the rotation temperatures derived using different tracers in the same substructure vary. Comparing with the results of others studies, the variation in T_{rot} for different species can be explained.

– Our opacity-corrected temperature in HC derived from CH_3CN is 120–160 K, which is a factor of 1.5 lower

²² In the extreme case, the ratio is 0.8–1, if assuming the ice mantle is completely evaporated.

than reported by Goddi et al. (2011a) from NH_3 at a higher angular resolution ($\sim 0.8''$). Given that HNCO in our dataset probes the similar temperatures, our slightly lower temperatures for N-bearing molecules may trace the envelope region of the HC.

- Our adopted temperatures from HCOOCH_3 agree with the temperatures estimated by Favre et al. (2011a) from observations of this species at similar spatial resolution²³. However, they are lower than those reported in Brouillet et al. (2013) owing to our spectral resolution. Multiplets of CH_3OCH_3 and $\text{CH}_3\text{CH}_2\text{OH}$ are not resolved in this paper, so we treat each detected line of these species as a single component, and temperatures obtained from rotation diagrams are potentially underestimated²⁴.
 - Temperatures probed by CH_3OH (> 200 K in HC, ~ 170 in mm2, and ~ 160 K in CR) are higher than those probed by the other molecules, probably because of the lack of optical depth corrections, or because they trace gas with different temperatures (discussed in Section 4.4 part 1 (2)). Nevertheless, these temperatures agree with those derived from the same species by Sutton et al. (1995) ($^{13}\text{CH}_3\text{OH}$) and Friedel & Widicus Weaver (2012) in HC and CR, and by Beuther et al. (2005) in HC and mm2.
 - We note that S-bearing species may be affected by shocks in the environment. Although they were not often derived previously, and the high E_u/k_B transition leads to large uncertainties in the rotation temperatures derived from $^{34}\text{SO}_2$, our estimated temperatures are within the uncertainty of those derived by Esplagues et al. (2013) from SO_2 in HC (190 ± 60 K) and CR (80 ± 30 K).
2. Due to the compactness of the detected substructures, column densities of CO , ^{13}CO , and C^{18}O are ten times higher than those from lower resolution observations in single-dish observations of Wilson et al. (2011) (FWHP $\sim 13''$) and in Plume et al. (2012) (Herschel/HIFI beam ranges from $13''$ to $40''$). If taking the beam ratio into account, our results are consistent with previous measurement.
 3. In both HC and CR, the abundances of SO , SO_2 , HNCO , HC_3N , CH_3OH , CH_2CHCN , $\text{CH}_3\text{CH}_2\text{CN}$, and CO are comparable to the values in Blake et al. (1987); Wright et al. (1996), and Esplagues et al. (2013), within our factor of 1.5-2 uncertainties. H_2^{13}CO is lower than the value derived from H_2CO in Blake et al. (1987), assuming a standard $^{12}\text{C}/^{13}\text{C}$ ratio, but is comparable to the value in Wright et al. (1996). After the optical depth corrections, our OCS and CH_3CN abundances are ten times higher than those in Blake et al. (1987), because the latter estimation was made assuming lines of these species to be optically thin.

However, our abundances of OCS and ^{13}CS are comparable to those in Tercero et al. (2010), within our factor of 2 uncertainty.

4. Similar to the gradient in Sutton et al. (1995) and Wright et al. (1996), CO and SO have stronger emission and higher abundances in the plateau of both the high- and low-velocity outflows, which has been suggested to be due to shock enhancement in these regions. Although molecules in general have around 1-2 magnitudes lower abundances in our low-velocity outflow than the values reported in the NE–SW plateau from previous interferometric study (Wright et al. 1996), their abundances in our high-velocity outflow are comparable to the single dish results in the NW–SE plateau (Sutton et al. 1995).
5. The estimated column densities of COMs ($\text{CH}_3\text{CH}_2\text{CN}$, CH_3COCH_3 , CH_3OCH_3 , and HCOOCH_3) in HC are found to be lower than the values in Friedel & Snyder (2008) by a factor of 10, because their observations have a smaller synthetic beam. However, HCOOCH_3 has comparable column densities to Favre et al. (2011a) in mm2 (MF4–5), mm3a (MF3), and mm3b (MF1), as does CH_3OCH_3 compared to Brouillet et al. (2013) at all the central condensations (HC, mm2, mm3a, and mm3b), and the abundance of CH_3COCH_3 compared to Peng et al. (2013) at HC and mm2 (Ace-3).

To sum up, the abundance of most species from our study are comparable to previous single-dish studies especially in the central condensations. Therefore, molecular abundance estimation from single-dish observations for the farther sources (e.g., ten times farther than Orion-KL) should be trustworthy at least in the source centre after optical depth correction.

5.2. Chemistry in the hot molecular core

At a spatial resolution of ~ 1200 AU, our data resolves Orion-KL into several condensations. The specific intensities (Jy beam^{-1}) of the dust continuum peaks exhibit a gradient from the central condensations to the extended structures, and the gas temperatures exhibit the same gradient: The HC is the strongest continuum substructure, because it has both the highest gas temperature and column density; mm2, mm3a, and mm3b are slightly fainter and less dense; while NE and SR have weaker continuum and line emission than the former sources, but stronger emission than OF1N(S).

Differentiation in the spatial distribution of S-, N-, and O-bearing species clearly shows that chemistry in the central condensations of Orion-KL is not homogeneous. Simple N- and O-bearing molecules show the strongest emission towards the central condensations. However, unlike most of the N-bearing species (including N-bearing COMs) which are not detected in SR, NE, or the outflow, simple organic molecules (H_2^{13}CO , CH_2CO) and CO (^{13}CO , C^{18}O) have bright extended emission even towards the cooler and less dense regions (SR, OF1N, and OF1S). Compared to the above extreme cases, the S-bearing molecules are widely distributed over the central condensations, NE and (or) SR. A possible reason for this is that the S-bearing molecules are mainly formed via warm gas-phase chemistry or shock chemistry (e.g., Pineau des Forets et al. 1993; Charnley et al. 1997), and then coincide with both N- and O-bearing molecules in the plateau (NE) of BN/KL (e.g., Chandler & Wood 1997; Schreyer & Henning 1999, see discussion in

²³ MF1–5 are the HCOOCH_3 emission peaks in Favre et al. (2011a), which coincide with mm3b (MF1), HC (MF2), mm3a (MF3), and mm2 (MF4–5) in our continuum.

²⁴ Brouillet et al. (2013) resolves the CH_3OCH_3 multiplets and uses them to estimate temperatures as well as column densities. However, if each multiplet is treated as a single component, it would derive temperatures consistent with those we estimate.

Section 5.3).

For the COMs, it has been widely suggested that “N-/O-chemical differentiation” can be caused by lower or higher temperatures during the cold pre-hot molecular core phase and different paces of warm-up in these regions (Caselli et al. 1993; Garrod et al. 2008; Neill et al. 2011; Laas et al. 2011). Besides confirming the HC peak of N-bearing COMs (CH_2CHCN , $\text{CH}_3\text{CH}_2\text{CN}$, CH_3CN , and $\text{CH}_3^{13}\text{CN}$) and the mm3a (or/and mm3b) peak of several O-bearing COMs (e.g., HCOOCH_3 and CH_3OCH_3), we found several other COMs which cannot be classified within these dichotomous emission peaks groups (also see Guélin et al. 2008; Friedel & Widicus Weaver 2012; Peng et al. 2013). For example, the peak of CH_3OH is velocity dependent, shifting from the HC (3.6 km s^{-1}) through mm3a (6 km s^{-1}) to mm3b (7.2 km s^{-1}); the peak of $\text{CH}_3\text{CH}_2\text{OH}$ is in between the HC and mm3a. In contrast, CH_3COCH_3 shares a morphology with N-bearing molecules – peaking towards the HC with a V-shaped distribution. This similarity in morphologies may indicate a link between the HC-peaking N-bearing species and the mm3a (or/and mm3b)-peaking species, therefore their formation pathways likely involve NH_3 (ammonia) or another major N-bearing molecule (e.g., Chen & Woon 2011), or need similar physical conditions appropriate to their production and/or sublimation, such as shocks (Peng et al. 2013). Moreover, although CH_3CHO is only tentatively detected, it peaks in a similar location to HCOOCH_3 . Furthermore, like CH_2CO , it exhibits extended emission from the NE to the SE tail, suggesting these three species may share a common or at least a related formation path.

The favoured model of hot molecular core chemistry so far is the gas-grain model, where frozen radicals, partly produced by photolysis, become mobile during the warm-up phase, and their reactions produce COMs (Markwick et al. 2000; Garrod et al. 2008). Three phases are usually modelled, the cold, warm-up, and hot molecular core stages. During these stages, different species are defined as zeroth-generation (e.g., CH_3OH), first-generation (e.g., HCOOCH_3), and second-generation organic molecules (see Herbst & van Dishoeck 2009). In such a scenario, since the critical densities are fairly similar for N- and O-bearing species, the distribution diversity of species in Orion-KL may also be explained by different initial compositions or different chemical “ages” (evolutionary stage, the time that the gas phase species has had to evolve from an initial composition after being released from ice mantles, Friedel & Snyder 2008). If that is the case, COMs like $\text{CH}_3\text{OCH}_3/\text{CH}_3\text{OH}$ can act as chemical clocks, implying that the different substructures in BN/KL could have different chemical ages (e.g., Charnley et al. 1997; Wakelam et al. 2004).

In addition to grain-surface and gas-phase chemical processing, it is also possible that varying physical conditions, including temperature, density, and kinematics cause the differentiation in the spatial distributions of molecular line emission seen in the Orion-KL region. Probably due to the difference in the central protostars, the warm-up paces of different substructures vary. The modelling result from Garrod et al. (2008) (especially their Figure 8) is an example. In a particular substructure during the warm-up process (e.g., from 100 K to 200 K), the abundances of some molecules increase (e.g., HNCO , CH_3CN , CH_3OH) because of their evaporation from the grain surface to the gas phase, while the abundances of some large molecules cannot be synthesized on grains any longer because their precursor

species have desorbed to the gas phase. They decrease (e.g., HCOOCH_3 , CH_3OCH_3) or start to decrease (CH_3OH). Another possibility is that these species are destroyed by ion-molecule chemistry (e.g., by protonation via XH^+ molecules), followed by dissociative recombination into multiple small fragments. In this scenario, the different emission peaks of different species can be explained by the higher temperature in HC (120–160 K) than in mm3a and mm3b (80–100 K), meaning that N-bearing species are still evaporating in HC but formation of molecules such as HCOOCH_3 is stopped or it is dissociating there.

5.3. Chemistry in the outflow

Outflows from young stars can destroy grain material and/or liberate ices when they impact the surrounding cold matter, meaning that chemical reactions can be driven by the associated shocks even in cold gas (Herbst & van Dishoeck 2009). For years, the outflows in Orion-KL have been the main subject of chemical studies of this region (Wright et al. 1996 and references therein). Although COMs are less abundant or not detected in these outflows, the chemistry of simple molecules especially shock tracers can provide an alternative way to investigate the gas structure of the outflows.

Two outflows have been reported in Orion-KL, almost perpendicular to each other. In addition, along the NE–SW direction, a large-scale “integral-shaped” filament has been detected aligned with the low-velocity outflow (Wright et al. 1992; Lis et al. 1998; Di Francesco et al. 2008). To confirm whether the NE clump is associated with the filament or the outflow, we selected several widespread species, and use a Gaussian function to fit their line profile extracted from NE (Figure 7). Broad line wings (C^{18}O) and a second component (HNCO , SO_2 , and ^{34}SO) with $V_{\text{peak}} \sim 20 - 23 \text{ km s}^{-1}$ indicate that line emission in NE contains significant contribution from the outflow and is part of the plateau.

To study the chemistry in the outflows, we image the blue- and red-shifted gas of several shock-tracing molecules along the outflow direction (Figure A4). To avoid contamination from blending, we image as broad a velocity range as possible (labelled in each panel), though, $-20 \sim +30 \text{ km s}^{-1}$ is the limit for most lines other than SO , CO , and ^{13}CO . Because of the range limit and the limits of the $52''$ primary beam, the high-velocity outflow ($30 - 100 \text{ km s}^{-1}$) cannot be imaged in its entirety. However, the low-velocity outflow ($\sim 18 \text{ km s}^{-1}$) with a NE–SW elongated structure is clearly detected, showing bipolar structure in the intensity-integrated map of H_2^{13}CO . In addition, intensity-integrated maps of such molecules as OCS , $^{34}\text{SO}_2$, SO , HNCO , CH_2CO , CO , and ^{13}CO all have a “butterfly” morphology, with blue-shifted radial velocities of the moving gas towards the NW and the red-shifted velocities in the SE. This morphology is exactly the same as found in SiO (Wright et al. 1995; Plambeck et al. 2009; Zapata et al. 2012; Niederhofer et al. 2012) and H_2O maser observations (Greenhill et al. 2013) on scales of tens of AU. Whether this morphology is due to the bipolar lobes of the high-velocity outflow or to the expanding low-velocity outflow is still not clear. Possibilities are discussed (e.g., two bipolar outflows from a precessing binary, ballistic ejecta from a rotating disk, a single expanding wide-angle NE–SW outflow; Zapata et al. 2012). The asymmetry shape of the lobes (e.g., “U” shape blue-shifted and half “U” red-shifted lobes in the map of SO) is said to

come from some density inhomogeneities in the surroundings (Zapata et al. 2012) or the interaction between outflow and the environment (Niederhofer et al. 2012).

Therefore, it can be suggested that a picture of explosive NW–SE outflow explains the excitation temperature gradient from the central condensations to the extended outflows in Orion-KL (Zapata et al. 2012): the decelerated bullets can be absorbed by the BN/KL cloud, and their kinetic energy can be transferred to thermal energy (Peng et al. 2012b); the closer a gas parcel is to the explosion centre (e.g., the closer encounter of BN, source I and maybe also source N, suggested by proper motion studies from Rodríguez et al. 2005; Gómez et al. 2005, 2008 and 3D modelling from Nissen et al. 2012), the higher the thermal energy available to affect the chemical properties of the gas in the HC and mm2.

Of all the shock-related molecules, S-bearing species are of special interest, not only because their abundance may be enhanced by shocks (Martin-Pintado et al. 1992; Pineau des Forets et al. 1993; Chernin et al. 1994; Bachiller & Pérez Gutiérrez 1997; Schilke et al. 1997; Charnley et al. 1997; Bachiller et al. 2001; Viti et al. 2004; Garrod 2013), but also because they have been proposed as potential chemical clocks to date outflows (and hence their protostellar driving source; e.g., Charnley et al. 1997; Wakelam et al. 2004). The angular resolution of our study does not allow us to investigate the post/pre-shocked chemistry. In spite of that, we do find that some S-bearing molecules (e.g., SO_2 , $^{34}\text{SO}_2$, and SO) have almost the same abundances in NE as in the central sources, which are higher than those in OF1N(S), even though we assume the temperatures in NE and OF1N(S) are equally low. The enhancement of their abundance may indicate stronger shocks in this direction than the rest of Orion-KL. On the other hand, although we cannot tell the precise ages of different substructures, we can compare the variations in abundance ratios SO_2/SO in our observations to the gas-grain modelling result. To simplify the case, we assume that the temperatures in all substructures are 100 K and that all substructures have the same density $\sim 10^7 \text{ cm}^{-3}$, and we estimate the value of SO_2 (lines are possibly optically thick) by using $^{34}\text{SO}_2$ and a ratio of $^{32}\text{S}/^{34}\text{S} = 22$ (Wilson & Rood 1994). Comparing the observed SO_2/SO ratio to modelling of Wakelam et al. (2004)²⁵ in all substructures (Figure 11), we find that the HC has the highest SO_2/SO ratio, which suggests it is the most evolved substructure. Also, mm2, mm3a, and mm3b have lower ratios and are younger. The lowest ratios are in the outflows, which indicate the age of the low-velocity outflow should be $\ll 1 \times 10^4$ years, while the high-velocity outflow should be $\ll 1 \times 10^3$ years²⁶.

The shocks could also be responsible for the observed chemical differentiation in COMs (e.g., by stripping ices from grains). The CR (together with mm3a and mm3b) is thought to be the place where icy grains are released into the gas phase by an outflow from the HC (Blake et al. 1987; Liu et al. 2002). Therefore, based on the reported association between the

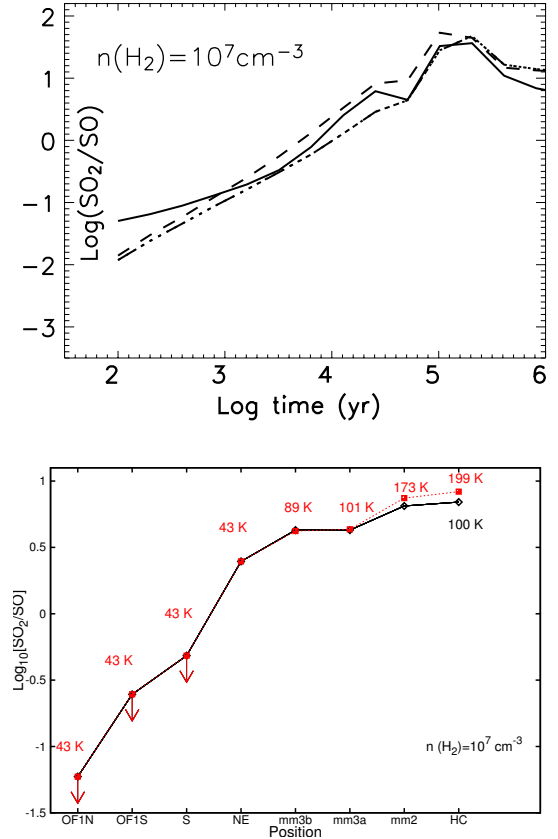


Fig. 11: Observed SO_2/SO ratio compared to the model prediction. The upper panel is adopted from Figure 5 of Wakelam et al. (2004) (100 K , 10^7 cm^{-3}), where different line types are from different grain component models. The lower panel is from our observed SO_2/SO ratio by assuming (1) all substructures have similar density 10^7 cm^{-3} and (2) $N_{\text{SO}_2}/N_{^{34}\text{SO}_2} = 22$ (Wilson & Rood 1994). The black solid line comes from the assumption that all substructures have a temperature close to 100 K , and the red dotted line comes from different temperatures derived in Section 4.1 (labelled in red).

emissions of HCOOCH_3 and the $2.12 \mu\text{m}$ vibrationally excited H_2 (Lacombe et al. 2004), it has been suggested that shocks between the ISM and high-velocity gas “bullets” from the outflow (Zapata et al. 2009; Bally et al. 2011) explains the production of COMs, which has the same morphology as HCOOCH_3 (Favre et al. 2011b). In a similar scenario, N-bearing COMs may be released to the gas phase north-east of the HC (e.g., HC_3N , CH_2CHCN), where the low-velocity outflow is impacting the ambient dusty material, and the weak emission /nondetection of these molecules along the high-velocity outflow may be due to lack of dusty material in the NW–SE direction (Friedel & Widicus Weaver 2012).

5.4. Search for COMs

The chemistry of Orion-KL is rich, not only in high-density tracers and shock tracers, but also with numerous transitions of COMs, which are less abundant than the other tracers and which have a less well understood formation mechanism.

²⁵ In Wakelam et al. (2004), SO/H_2 ratio is sensitive to the grain components. However, SO_2/SO ratios from different grain component models are similar at a particular time (yr), so we compare this ratio to the observations.

²⁶ NE is part of the filamentary structure, so the age of the low-velocity outflow is implied from the upper limit ratio in SR. Due to the non-detection of SO_2 ($^{34}\text{SO}_2$) in OF1N(S), the age of the high-velocity outflow is implied from the upper limit ratio in OF1N.

Three possibilities have been discussed for the formation of the COMs: (1) ion-molecule chemistry involving large radicals (Ehrenfreund & Charnley 2000); (2) formation on dust grains and then released to the gas at higher temperatures in the later stages of star formation (Garrod et al. 2008; Herbst & van Dishoeck 2009); (3) a hybrid approach that COMs are ejected into the gas via efficient reactive desorption, after a sequence of gas-phase reactions between precursor species formed on grain surfaces (Vasyunin & Herbst 2013). In our dataset, we search for several COMs (Table 2) by using the synthetic fitting programme described in Section 3.2.2. HC₇N, C₆H, and CH₃CHO are tentatively detected because of missing predicted lines. For the remaining species, if not taking the blending problem into account, all the predicted transitions are robustly detected. In addition, we find that saturated molecules are likely to be more abundant than unsaturated molecules (e.g., HC₃N, C₆H, HC₇N). This indicates that these saturated species may be formed on dust grain surfaces by subsequent hydrogenation of their precursor species (such as CO, O, N or their more complex combinations).

Unfortunately, we lack the sensitivity to detect HCOOH (formic acid), which has been previously reported in Orion-KL by Liu et al. (2002). Line blending also prevents us from robustly detecting CH₂OHCHO (glycolaldehyde) and (CH₂OH)₂ (ethylene glycol) in our data. We also fail to detect other prebiotic molecules, e.g., NH₂CH₂COOH (glycine; Garrod 2013), CH₃COOH (acetic acid), NH₂CH₂CN (amino acetonitrile; Belloche et al. 2008), CH₃CONH₂ (acetamide; van Dishoeck 2009), and the ring molecules. More sensitive observations (e.g., with ALMA) are required to determine whether these molecules exist in the Orion-KL environment.

6. Conclusions

Based on the analysis of combined SMA and 30 m observations of Orion-KL, we have drawn the following conclusions:

1. From interferometric observations with the SMA, Orion-KL has been resolved into several continuum substructures with different peak flux densities, at the angular resolution of 3'' (1 200 AU at a distance of 414 pc). In addition to the previous well-known compact continuum substructures like the HC and mm2, our data resolves the clump south-west of HC into two cores: mm3a and mm3b. In addition, we confirmed the detection of strong continuum emissions ($> 5\sigma$) from two resolved clumps (SR and NE), which lie along the axis of both the low-velocity outflow and the large-scale dusty filament.
2. For the first time, we have combined interferometric and single-dish observations of Orion-KL, to correct missing short spacings, and achieved high sensitivity to all spatial scales. Covering a field of view of 52'', we mapped the distribution of all the identified species. In particular, we obtained the first maps of molecules such ³⁴SO₂, O¹³CS, HNCO, H₂¹³CO, ¹³CO, and CH₂CO with both high resolution and sensitivity to spatial information on all scales. We also identified several transitions of low abundance ($< 10^{-8}$ with respect to H₂) COMs, such as CH₃COCH₃ and CH₃CH₂OH, as well as made the tentative detection of

CH₃CHO and long carbon chains like C₆H and HC₇N.

3. The Orion KL region exhibits clear chemical differentiation on the scales probed by the SMA-30 m observations. The emission from S-bearing molecules, CO isotopologues, and simple organic molecules are extended, covering not only the central condensations (HC, mm2, mm3a, and mm3b), but also the NE clump, the SR, and even the outflow regions. In comparison, the distributions of COMs are more concentrated and hard to group. The segregated emission peaks at either the HC (e.g., N-bearing) or CR (together with mm3a and mm3b, e.g., HCOOCH₃, CH₃OCH₃) indicates different formation pathways for O-bearing and N-bearing molecules. However, some COMs peak in-between the HC and mm3a (e.g., CH₃CH₂OH), or have dual velocity dependent peaks (CH₃OH), or share the same morphology as N-bearing species (CH₃COCH₃), which may indicate the linking of some formation pathways between O-bearing and N-bearing molecules. Moreover, line widths of the N-bearing, S-bearing species, HCOOCH₃ and CH₃OH vary, and so do the derived rotation temperatures, indicating they trace different gas.
4. By studying the chemistry within outflows of Orion-KL, we found higher abundances of such shock tracers as ³⁴SO₂, SO₂, and SO in the plateau of the low-velocity outflow (NE), indicating stronger shocks in this direction than the rest of Orion-KL.
5. Molecular rotation temperatures and abundances show large gradient between central condensations and the outflow regions, indicating difference between hot molecular core and shock chemistry.

Acknowledgements. We would like to thank the SMA staff and IRAM 30 m staff for their helpful support during the reduction of the SMA data, the performance of the IRAM 30 m observations in service mode, Z. Y. Zhang and Y. Wang for helping with code development, for useful discussion, and the referee for constructive suggestions.

This research made use of NASA's Astrophysics Data System.

The Submillimetre Array is a joint project between the Smithsonian Astrophysical Observatory and the Academia Sinica Institute of Astronomy and Astrophysics, and it is funded by the Smithsonian Institution and the Academia Sinica.

S. F. acknowledges financial support by the European Community Seventh Framework Programme [FP7/2007-2013] under grant agreement no. 238258.

D. S. acknowledges support by the *Deutsche Forschungsgemeinschaft* through SPP 1385: "The first ten million years of the solar system - a planetary materials approach" (SE 1962/1-2).

References

- Allen, D. A. & Burton, M. G. 1993, *Nature*, 363, 54
- Andersson, M., Askne, J., & Hjalmarson, A. 1984, *A&A*, 136, 243
- Araya, E., Hofner, P., Kurtz, S., Bronfman, L., & DeDeo, S. 2005, *ApJS*, 157, 279
- Bachiller, R. & Pérez Gutiérrez, M. 1997, *ApJ*, 487, L93
- Bachiller, R., Pérez Gutiérrez, M., Kumar, M. S. N., & Tafalla, M. 2001, *A&A*, 372, 899
- Bajaja, E. & van Albada, G. D. 1979, *A&A*, 75, 251
- Bally, J., Cunningham, N. J., Moeckel, N., et al. 2011, *ApJ*, 727, 113
- Beckwith, S., Persson, S. E., Neugebauer, G., & Becklin, E. E. 1978, *ApJ*, 223, 464
- Bell, T. A., Cernicharo, J., Viti, S., et al. 2014, *A&A*, 564, A114
- Belloche, A., Garrod, R. T., Müller, H. S. P., et al. 2009, *A&A*, 499, 215
- Belloche, A., Menten, K. M., Comito, C., et al. 2008, *A&A*, 482, 179
- Bergin, E. A., Phillips, T. G., Comito, C., et al. 2010, *A&A*, 521, L20
- Bergin, E. A., Snell, R. L., & Goldsmith, P. F. 1996, *ApJ*, 460, 343

- Beuther, H., Churchwell, E. B., McKee, C. F., & Tan, J. C. 2007a, *Protostars and Planets V*, 165
- Beuther, H., Leurini, S., Schilke, P., et al. 2007b, *A&A*, 466, 1065
- Beuther, H., Linz, H., Bik, A., Goto, M., & Henning, T. 2010, *A&A*, 512, A29
- Beuther, H. & Nissen, H. D. 2008, *ApJ*, 679, L121
- Beuther, H., Zhang, Q., Greenhill, L. J., et al. 2004, *ApJ*, 616, L31
- Beuther, H., Zhang, Q., Greenhill, L. J., et al. 2005, *ApJ*, 632, 355
- Beuther, H., Zhang, Q., Reid, M. J., et al. 2006, *ApJ*, 636, 323
- Blake, G. A., Mundy, L. G., Carlstrom, J. E., et al. 1996, *ApJ*, 472, L49
- Blake, G. A., Sutton, E. C., Masson, C. R., & Phillips, T. G. 1987, *ApJ*, 315, 621
- Boucher, D., Burie, J., Bauer, A., Dubrulle, A., & Demaison, J. 1980, *Journal of Physical and Chemical Reference Data*, 9, 659
- Bronfman, L., Nyman, L.-A., & May, J. 1996, *A&AS*, 115, 81
- Brouillet, N., Despois, D., Baudry, A., et al. 2013, *A&A*, 550, A46
- Caselli, P., Hasegawa, T. I., & Herbst, E. 1993, *ApJ*, 408, 548
- Chandler, C. J. & Wood, D. O. S. 1997, *MNRAS*, 287, 445
- Chapman, J. F., Millar, T. J., Wardle, M., Burton, M. G., & Walsh, A. J. 2009, *MNRAS*, 394, 221
- Charnley, S. B. 2004, *Advances in Space Research*, 33, 23
- Charnley, S. B., Tielens, A. G. G. M., & Rodgers, S. D. 1997, *ApJ*, 482, L203
- Chen, L. & Woon, D. E. 2011, *J. Phys. Chem. A*, 115, 5166
- Chernin, L. M., Masson, C. R., & Fuller, G. A. 1994, *ApJ*, 436, 741
- Chernin, L. M. & Wright, M. C. H. 1996, *ApJ*, 467, 676
- Chin, Y.-N., Henkel, C., Whiteoak, J. B., Langer, N., & Churchwell, E. B. 1996, *A&A*, 305, 960
- Cohen, R. J., Gasiprongs, N., Meaburn, J., & Graham, M. F. 2006, *MNRAS*, 367, 541
- Comito, C., Schilke, P., Phillips, T. G., et al. 2005, *ApJS*, 156, 127
- Crockett, N. R., Bergin, E. A., Neill, J. L., et al. 2014, *ApJ*, 787, 112
- Demyk, K., Włodarczyk, G., & Carvajal, M. 2008, *A&A*, 489, 589
- Di Francesco, J., Johnstone, D., Kirk, H., MacKenzie, T., & Ledwosinska, E. 2008, *ApJS*, 175, 277
- Doeleman, S. S., Lonsdale, C. J., & Pelkey, S. 1999, *ApJ*, 510, L55
- Doi, T., O'Dell, C. R., & Hartigan, P. 2002, *AJ*, 124, 445
- Dougados, C., Lena, P., Ridgway, S. T., Christou, J. C., & Probst, R. G. 1993, *ApJ*, 406, 112
- Downes, D., Genzel, R., Becklin, E. E., & Wynn-Williams, C. G. 1981, *ApJ*, 244, 869
- Draine, B. T. 2011, *Physics of the Interstellar and Intergalactic Medium*
- Ehrenfreund, P. & Charnley, S. B. 2000, *ARA&A*, 38, 427
- Eisner, J. A., Plambeck, R. L., Carpenter, J. M., et al. 2008, *ApJ*, 683, 304
- Erickson, N. R., Goldsmith, P. F., Snell, R. L., et al. 1982, *ApJ*, 261, L103
- Esplugues, G. B., Tercero, B., Cernicharo, J., et al. 2013, *A&A*, 556, A143
- Favre, C., Despois, D., Brouillet, N., et al. 2011a, *A&A*, 532, A32
- Favre, C., Wootten, H. A., Remijan, A. J., et al. 2011b, *ApJ*, 739, L12
- Fish, V. L., Muehlbrad, T. C., Pratap, P., et al. 2011, *ApJ*, 729, 14
- Friedel, D. N. & Snyder, L. E. 2008, *ApJ*, 672, 962
- Friedel, D. N., Snyder, L. E., Remijan, A. J., & Turner, B. E. 2005, *ApJ*, 632, L95
- Friedel, D. N. & Widicus Weaver, S. L. 2011, *ApJ*, 742, 64
- Friedel, D. N. & Widicus Weaver, S. L. 2012, *ApJS*, 201, 17
- Garrod, R. T. 2013, *ApJ*, 765, 60
- Garrod, R. T., Weaver, S. L. W., & Herbst, E. 2008, *ApJ*, 682, 283
- Gaume, R. A., Wilson, T. L., Vrba, F. J., Johnston, K. J., & Schmid-Burgk, J. 1998, *ApJ*, 493, 940
- Genzel, R., Reid, M. J., Moran, J. M., & Downes, D. 1981, *ApJ*, 244, 884
- Genzel, R. & Stutzki, J. 1989, *ARA&A*, 27, 41
- Gerner, T., Beuther, H., Semenov, D., et al. 2014, *A&A*, 563, A97
- Goddi, C., Greenhill, L. J., Humphreys, E. M. L., Chandler, C. J., & Matthews, L. D. 2011a, *ApJ*, 739, L13
- Goddi, C., Humphreys, E. M. L., Greenhill, L. J., Chandler, C. J., & Matthews, L. D. 2011b, *ApJ*, 728, 15
- Goldsmith, P. F. & Langer, W. D. 1999, *ApJ*, 517, 209
- Goldsmith, P. F., Snell, R. L., Deguchi, S., Krotkov, R., & Linke, R. A. 1982, *ApJ*, 260, 147
- Gómez, L., Rodríguez, L. F., Loinard, L., et al. 2008, *ApJ*, 685, 333
- Gómez, L., Rodríguez, L. F., Loinard, L., et al. 2005, *ApJ*, 635, 1166
- Greaves, J. S. & White, G. J. 1991, *A&AS*, 91, 237
- Greenhill, L. J., Gezari, D. Y., Danchi, W. C., et al. 2004, *ApJ*, 605, L57
- Greenhill, L. J., Goddi, C., Chandler, C. J., Matthews, L. D., & Humphreys, E. M. L. 2013, *ApJ*, 770, L32
- Greenhill, L. J., Gwinn, C. R., Schwartz, C., Moran, J. M., & Diamond, P. J. 1998, *Nature*, 396, 650
- Guélin, M., Brouillet, N., Cernicharo, J., Combes, F., & Wootten, A. 2008, *Ap&SS*, 313, 45
- Hasegawa, T. I. & Herbst, E. 1993, *MNRAS*, 261, 83
- Herbst, E. 1981, *Nature*, 289, 656
- Herbst, E. & van Dishoeck, E. F. 2009, *ARA&A*, 47, 427
- Hildebrand, R. H. 1983, *QJRAS*, 24, 267
- Ho, P. T. P., Moran, J. M., & Lo, K. Y. 2004, *ApJ*, 616, L1
- Hollis, J. M. 1982, *ApJ*, 260, 159
- Hollis, J. M., Jewell, P. R., Lovas, F. J., & Remijan, A. 2004, *ApJ*, 613, L45
- Hollis, J. M., Lovas, F. J., & Jewell, P. R. 2000, *ApJ*, 540, L107
- Hollis, J. M., Lovas, F. J., Jewell, P. R., & Coudert, L. H. 2002, *ApJ*, 571, L59
- Johansson, L. E. B., Andersson, C., Ellender, J., et al. 1984, *A&A*, 130, 227
- Johnstone, D. & Bally, J. 1999, *ApJ*, 510, L49
- Kalenskii, S. V., Promislov, V. G., Alakoz, A., Winnberg, A. V., & Johansson, L. E. B. 2000, *A&A*, 354, 1036
- Kwan, J. & Scoville, N. 1976, *ApJ*, 210, L39
- Laas, J. C., Garrod, R. T., Herbst, E., & Widicus Weaver, S. L. 2011, *ApJ*, 728, 71
- Lacombe, F., Gendron, E., Rouan, D., et al. 2004, *A&A*, 417, L5
- Lee, C. W. & Cho, S.-H. 2002, *Journal of Korean Astronomical Society*, 35, 187
- Lee, J.-K. & Burton, M. G. 2000, *MNRAS*, 315, 11
- Lerate, M. R., Yates, J., Viti, S., et al. 2008, *MNRAS*, 387, 1660
- Lis, D. C., Serabyn, E., Keene, J., et al. 1998, *ApJ*, 509, 299
- Liu, S.-Y., Girart, J. M., Remijan, A., & Snyder, L. E. 2002, *ApJ*, 576, 255
- Loren, R. B. & Mundy, L. G. 1984, *ApJ*, 286, 232
- Lovas, F. J. 2004, *Phys. Chem. Ref.*, 33, 117
- Markwick, A. J., Millar, T. J., & Charnley, S. B. 2000, *ApJ*, 535, 256
- Martin-Pintado, J., Bachiller, R., & Fuente, A. 1992, *A&A*, 254, 315
- Masson, C. R., Claussen, M. J., Lo, K. Y., et al. 1985, *ApJ*, 295, L47
- Masson, C. R., Lo, K. Y., Phillips, T. G., et al. 1987, *ApJ*, 319, 446
- Matthews, L. D., Greenhill, L. J., Goddi, C., et al. 2010, *ApJ*, 708, 80
- McCarthy, M. C., Gottlieb, C. A., Gupta, H., & Thaddeus, P. 2006, *ApJ*, 652, L141
- Meier, D. S. & Turner, J. L. 2005, *ApJ*, 618, 259
- Menten, K. M. & Reid, M. J. 1995, *ApJ*, 445, L157
- Menten, K. M., Reid, M. J., Forbrich, J., & Brunthaler, A. 2007, *A&A*, 474, 515
- Miotello, A., Testi, L., Lodato, G., et al. 2014, *A&A*, 567, A32
- Müller, H. S. P., Schlöder, F., Stutzki, J., & Winnewisser, G. 2005, *Journal of Molecular Structure*, 742, 215
- Mundy, L. G., Scoville, N. Z., Baath, L. B., Masson, C. R., & Woody, D. P. 1986, *ApJ*, 304, L51
- Murata, Y., Kawabe, R., Ishiguro, M., et al. 1992, *PASJ*, 44, 381
- Myers, P. C., Linke, R. A., & Benson, P. J. 1983, *ApJ*, 264, 517
- Neill, J. L., Steber, A. L., Muckle, M. T., et al. 2011, *Journal of Physical Chemistry A*, 115, 6472
- Niederhofer, F., Humphreys, E. M. L., & Goddi, C. 2012, *A&A*, 548, A69
- Nissen, H. D., Cunningham, N. J., Gustafsson, M., et al. 2012, *A&A*, 540, A119
- Nissen, H. D., Gustafsson, M., Lemaire, J. L., et al. 2007, *A&A*, 466, 949
- Norris, R. P. 1984, *MNRAS*, 207, 127
- Nummelin, A., Bergman, P., Hjalmarson, Å., et al. 2000, *ApJS*, 128, 213
- Olmi, L., Cesaroni, R., & Walmsley, C. M. 1993, in *Bulletin of the American Astronomical Society*, Vol. 25, American Astronomical Society Meeting Abstracts, 1315
- Olofsson, A. O. H., Persson, C. M., Koning, N., et al. 2007, *A&A*, 476, 791
- Ossenkopf, V. & Henning, T. 1994, *A&A*, 291, 943
- Palau, A., Fuente, A., Girart, J. M., et al. 2011, *ApJ*, 743, L32
- Peng, T.-C., Despois, D., Brouillet, N., et al. 2013, *A&A*, 554, A78
- Peng, T.-C., Despois, D., Brouillet, N., Parise, B., & Baudry, A. 2012a, *A&A*, 543, A152
- Peng, T.-C., Zapata, L. A., Wyrowski, F., Güsten, R., & Menten, K. M. 2012b, *A&A*, 544, L19
- Persson, C. M., Olofsson, A. O. H., Koning, N., et al. 2007, *A&A*, 476, 807
- Pickett, H. M., Poynter, R. L., Cohen, E. A., et al. 1998, *J. Quant. Spec. Radiat. Transf.*, 60, 883
- Pineau des Forets, G., Roueff, E., Schilke, P., & Flower, D. R. 1993, *MNRAS*, 262, 915
- Plambeck, R. L., Wright, M. C. H., Friedel, D. N., et al. 2009, *ApJ*, 704, L25
- Plambeck, R. L., Wright, M. C. H., Welch, W. J., et al. 1982, *ApJ*, 259, 617
- Plume, R., Bergin, E. A., Phillips, T. G., et al. 2012, *ApJ*, 744, 28
- Purcell, C. R., Balasubramanyam, R., Burton, M. G., et al. 2006, *MNRAS*, 367, 553
- Reid, M. J., Menten, K. M., Greenhill, L. J., & Chandler, C. J. 2007, *ApJ*, 664, 950
- Remijan, A. J., Leigh, D. P., Markwick-Kemper, A. J., & Turner, B. E. 2008, *ArXiv e-prints*
- Rice, C. A. & Maier, J. P. 2013, *Journal of Physical Chemistry A*, 117, 5559
- Rizzo, J. R., Martín-Pintado, J., & de Vicente, P. 2001, in *Highlights of Spanish astrophysics II*, ed. J. Zamorano, J. Gorgas, & J. Gallego, 397
- Rodríguez, L. F., Poveda, A., Lizano, S., & Allen, C. 2005, *ApJ*, 627, L65
- Sanchez-Monge, A. 2011, PhD thesis, University of Barcelona
- Sandstrom, K. M., Peek, J. E. G., Bower, G. C., Bolatto, A. D., & Plambeck, R. L. 2007, *ApJ*, 667, 1161
- Sault, R. J., Teuben, P. J., & Wright, M. C. H. 1995, in *Astronomical Society of*

- the Pacific Conference Series, Vol. 77, Astronomical Data Analysis Software and Systems IV, ed. R. A. Shaw, H. E. Payne, & J. J. E. Hayes, 433
- Schilke, P., Benford, D. J., Hunter, T. R., Lis, D. C., & Phillips, T. G. 2001, *ApJS*, 132, 281
- Schilke, P., Walmsley, C. M., Pineau des Forets, G., & Flower, D. R. 1997, *A&A*, 321, 293
- Schreyer, K. & Henning, T. 1999, in *ASP Conference Series*, Vol. 99, *The Orion Complex Revisited*, 1999
- Schuller, F., Menten, K. M., Contreras, Y., et al. 2009, *A&A*, 504, 415
- Scoville, N. Z., Hall, D. N. B., Ridgway, S. T., & Kleinmann, S. G. 1982, *ApJ*, 253, 136
- Snyder, L. E., Lovas, F. J., Hollis, J. M., et al. 2005, *ApJ*, 619, 914
- Snyder, L. E., Lovas, F. J., Mehringer, D. M., et al. 2002, *ApJ*, 578, 245
- Sugai, H., Usuda, T., Kataza, H., et al. 1994, *ApJ*, 420, 746
- Sutton, E. C., Blake, G. A., Masson, C. R., & Phillips, T. G. 1985, *ApJS*, 58, 341
- Sutton, E. C., Peng, R., Danchi, W. C., et al. 1995, *ApJS*, 97, 455
- Tan, J. C., Beltran, M. T., Caselli, P., et al. 2014, *ArXiv e-prints*
- Tang, Y.-W., Ho, P. T. P., Koch, P. M., & Rao, R. 2010, *ApJ*, 717, 1262
- Taylor, K. N. R., Storey, J. W. V., Sandell, G., Williams, P. M., & Zealey, W. J. 1984, *Nature*, 311, 236
- Tercero, B., Cernicharo, J., Pardo, J. R., & Goicoechea, J. R. 2010, *A&A*, 517, A96
- Thorwirth, S. 2001, PhD thesis, I. Physikalisches Institut Universität zu Köln Zùlpicher Str. 77 50937 Köln Germany
- Tideswell, D. M., Fuller, G. A., Millar, T. J., & Markwick, A. J. 2010, *A&A*, 510, A85
- Turner, B. E. 1989, *ApJS*, 70, 539
- Turner, B. E. 1991, *ApJS*, 76, 617
- Turner, B. E., Terzieva, R., & Herbst, E. 1999, *ApJ*, 518, 699
- van der Tak, F. F. S., Black, J. H., Schöier, F. L., Jansen, D. J., & van Dishoeck, E. F. 2007, *A&A*, 468, 627
- van Dishoeck, E. F. 2009, *Astrochemistry of Dense Protostellar and Protoplanetary Environments*, ed. H. A. Thronson, M. Stiavelli, & A. Tielens, 187
- Vasyunin, A. I. & Herbst, E. 2013, *ApJ*, 769, 34
- Viti, S., Codella, C., Benedettini, M., & Bachiller, R. 2004, *MNRAS*, 350, 1029
- Wakelam, V., Caselli, P., Ceccarelli, C., Herbst, E., & Castets, A. 2004, *A&A*, 422, 159
- Wang, S., Bergin, E. A., Crockett, N. R., et al. 2011, *A&A*, 527, A95
- Widicus Weaver, S. L. & Friedel, D. N. 2012, *ApJS*, 201, 16
- Wilner, D. J., Wright, M. C. H., & Plambeck, R. L. 1994, *ApJ*, 422, 642
- Wilson, T. L., Gaume, R. A., Gensheimer, P., & Johnston, K. J. 2000, *ApJ*, 538, 665
- Wilson, T. L., Muders, D., Dumke, M., Henkel, C., & Kawamura, J. H. 2011, *ApJ*, 728, 61
- Wilson, T. L., Rohlf, K., & Hüttemeister, S. 2009, *Tools of Radio Astronomy* (Springer-Verlag)
- Wilson, T. L. & Rood, R. 1994, *ARA&A*, 32, 191
- Woody, D. P., Scott, S. L., Scoville, N. Z., et al. 1989, *ApJ*, 337, L41
- Wright, M., Sandell, G., Wilner, D. J., & Plambeck, R. L. 1992, *ApJ*, 393, 225
- Wright, M. C. H. & Plambeck, R. L. 1983, *ApJ*, 267, L115
- Wright, M. C. H., Plambeck, R. L., & Wilner, D. J. 1995, *Astronomy Data Image Library*, 2
- Wright, M. C. H., Plambeck, R. L., & Wilner, D. J. 1996, *ApJ*, 469, 216
- Wynn-Williams, C. G., Genzel, R., Becklin, E. E., & Downes, D. 1984, *ApJ*, 281, 172
- Zapata, L. A., Rodríguez, L. F., Schmid-Burgk, J., et al. 2012, *ApJ*, 754, L17
- Zapata, L. A., Schmid-Burgk, J., Ho, P. T. P., Rodríguez, L. F., & Menten, K. M. 2009, *ApJ*, 704, L45
- Zapata, L. A., Schmid-Burgk, J., & Menten, K. M. 2011, *A&A*, 529, A24
- Zeng, Q., Mao, P. Q., & Pei, C. C. 2006, *Microwave spectrum of astrophysics diagnosis* (Chinese edition)
- Zinchenko, I., Henkel, C., & Mao, R. Q. 2000, *A&A*, 361, 1079
- Zinnecker, H. & Yorke, H. W. 2007, *ARA&A*, 45, 481
- Ziurys, L. M. & McGonagle, D. 1993, *ApJS*, 89, 155
- Zuckerman, B., Kuiper, T. B. H., & Rodríguez Kuiper, E. N. 1976, *ApJ*, 209, L137

Appendix A:

Table A1. Identified emission lines from the SMA-30 m combined dataset.

Freq. (GHz)	Mol.	E_u/k_B (K)	Note	Freq. (GHz)	Mol. (candidates)	E_u/k_B (K)	Note
218.903	OCS($v=0$)(18 \rightarrow 17)	100					
218.966	HCOOCH ₃ ($v=1$)(18 _{12,6} \rightarrow 17 _{12,5})E	384					
218.981	HNCO($v=0$)(10 _{1,10} \rightarrow 9 _{1,9})	101					
219.068	HCOOCH ₃ ($v=1$)(18 _{17,2} \rightarrow 17 _{17,1})E	481					
219.079	HCOOCH ₃ ($v=1$)(28 _{3,25} \rightarrow 28 _{2,26})E	434					
219.090	HCOOCH ₃ ($v=0$)(34 _{7,28} \rightarrow 34 _{5,29})E	387	*	219.090	HCOOCH ₃ ($v=0$)(34 _{7,28} \rightarrow 34 _{5,29})A	387	
219.154	HCOOCH ₃ ($v=1$)(18 _{11,7} \rightarrow 17 _{11,6})E	369	*	219.153	HCOOCH ₃ ($v=1$)(10 _{4,6} \rightarrow 9 _{3,6})E	230	
219.174	HC ₃ N($v_7=1$)(24 \rightarrow 23)	452	†				
219.195	HCOOCH ₃ ($v=1$)(18 _{16,3} \rightarrow 17 _{16,2})E	459	*	219.196	HCOOCH ₃ ($v=0$)(36 _{6,30} \rightarrow 36 _{6,31})E	429	
219.220	CH ₃ COCH ₃ ($v=0$)(21 _{1,20} \rightarrow 20 _{2,19})AE	122	*	219.220	CH ₃ COCH ₃ ($v=0$)(21 _{2,20} \rightarrow 20 _{1,19})AE	122	
				219.220	CH ₃ COCH ₃ ($v=0$)(21 _{2,20} \rightarrow 20 _{2,19})EA	122	
				219.220	CH ₃ COCH ₃ ($v=0$)(21 _{1,20} \rightarrow 20 _{1,19})EA	122	
219.242	CH ₃ COCH ₃ ($v=0$)(21 _{1,20} \rightarrow 20 _{2,19})EE	122	*	219.242	CH ₃ COCH ₃ ($v=0$)(21 _{2,20} \rightarrow 20 _{1,19})EE	122	
				219.242	CH ₃ COCH ₃ ($v=0$)(21 _{2,20} \rightarrow 20 _{2,19})EE	122	
				219.220	CH ₃ COCH ₃ ($v=0$)(21 _{1,20} \rightarrow 20 _{1,19})EE	122	
219.264	CH ₃ COCH ₃ ($v=0$)(21 _{1,20} \rightarrow 20 _{2,19})AA	122	*	219.264	CH ₃ COCH ₃ ($v=0$)(21 _{2,20} \rightarrow 20 _{1,19})AA	122	
219.276	SO ₂ ($v=0$)(22 _{7,15} \rightarrow 23 _{6,18})	352					
219.311	CH ₃ COCH ₃ ($v=0$)(12 _{9,4} \rightarrow 11 _{8,3})AA	66					
219.325	UL		?				
219.331	HCOOCH ₃ ($v=1$)(18 _{15,4} \rightarrow 17 _{15,3})E	438	*	219.328	HCOOCH ₃ ($v=1$)(36 _{9,28} \rightarrow 36 _{8,29})E	635	
219.355	³⁴ SO ₂ ($v=0$)(11 _{1,11} \rightarrow 10 _{0,10})	60	†				
219.401	CH ₂ CHCN($v=0$)(23 _{3,20} \rightarrow 22 _{3,19})	145					
219.412	HCOOCH ₃ ($v=1$)(18 _{10,8} \rightarrow 17 _{10,7})E	355					
219.417	HCOOCH ₃ ($v=0$)(30 _{5,26} \rightarrow 30 _{4,27})E	291					
219.463	CH ₃ CH ₂ CN(22 _{2,21} \rightarrow 21 _{1,20})	112					
219.479	HCOOCH ₃ ($v=1$)(18 _{14,5} \rightarrow 17 _{14,4})E	419					
219.484	HCOOCH ₃ ($v=0$)(30 _{5,26} \rightarrow 30 _{4,27})A	291					
219.506	CH ₃ CH ₂ CN($v=0$)(24 _{2,22} \rightarrow 23 _{2,21})	136					
219.547	HNCO($v=0$)(10 _{4,6} \rightarrow 9 _{4,5})	750	*	219.547	HNCO($v=0$)(10 _{4,7} \rightarrow 9 _{4,6})	750	
219.560	C ¹⁸ O(2 \rightarrow 1)	16	†				
219.566	HCOOCH ₃ ($v=1$)(18 _{15,4} \rightarrow 17 _{15,3})A	438	*	219.566	HCOOCH ₃ ($v=1$)(18 _{15,3} \rightarrow 17 _{15,2})A	438	
219.568	HCOOCH ₃ ($v=1$)(18 _{14,5} \rightarrow 17 _{14,4})A	419	*	219.568	HCOOCH ₃ ($v=1$)(18 _{14,4} \rightarrow 17 _{14,3})A	419	
219.571	HCOOCH ₃ ($v=1$)(18 _{16,3} \rightarrow 17 _{16,2})A	458	*	219.571	HCOOCH ₃ ($v=1$)(18 _{16,2} \rightarrow 17 _{16,1})A	458	
219.579	HCOOCH ₃ ($v=0$)(28 _{9,19} \rightarrow 28 _{8,20})A	294	*	219.579	HCOOCH ₃ ($v=1$)(18 _{17,2} \rightarrow 17 _{17,1})A	481	
				219.579	HCOOCH ₃ ($v=1$)(18 _{17,1} \rightarrow 17 _{17,0})A	481	
				219.578	HCOOCH ₃ ($v=1$)(29 _{9,21} \rightarrow 29 _{8,21})E	498	
219.584	HCOOCH ₃ ($v=1$)(18 _{13,6} \rightarrow 17 _{13,5})A	401	*	219.584	HCOOCH ₃ ($v=1$)(18 _{13,5} \rightarrow 17 _{13,4})A	401	
				219.586	HCOOCH ₃ ($v=0$)(30 _{9,22} \rightarrow 30 _{8,23})A	330	
219.592	HCOOCH ₃ ($v=0$)(28 _{9,19} \rightarrow 28 _{8,20})E	294					
219.600	HCOOCH ₃ ($v=0$)(30 _{9,22} \rightarrow 30 _{8,23})E	330					
219.607	HCOOCH ₃ ($v=0$)(30 _{5,26} \rightarrow 30 _{3,27})E	291	*	219.610	CH ₃ COCH ₃ ($v=0$)(33 _{8,25} \rightarrow 33 _{8,26})EE	368	
				219.610	CH ₃ COCH ₃ ($v=0$)(33 _{9,25} \rightarrow 33 _{7,26})EE	368	
219.622	HCOOCH ₃ ($v=1$)(18 _{12,7} \rightarrow 17 _{12,6})A	384	*	219.622	HCOOCH ₃ ($v=1$)(18 _{12,6} \rightarrow 17 _{12,5})A	384	
219.642	HCOOCH ₃ ($v=1$)(18 _{13,6} \rightarrow 17 _{13,5})E	401					
219.657	HNCO(10 _{3,8} \rightarrow 9 _{3,7})	447	*	219.657	HNCO(10 _{3,7} \rightarrow 9 _{3,6})	447	
219.696	HCOOCH ₃ ($v=1$)(18 _{11,8} \rightarrow 17 _{11,7})A	369	*	219.696	HCOOCH ₃ ($v=1$)(18 _{11,7} \rightarrow 17 _{11,6})A	369	
219.705	HCOOCH ₃ ($v=1$)(18 _{4,15} \rightarrow 17 _{4,14})A	299					
219.734	HNCO($v=0$)(10 _{2,9} \rightarrow 9 _{2,8})	231					
219.737	HNCO($v=0$)(10 _{2,8} \rightarrow 9 _{2,7})	231					
219.764	HCOOCH ₃ ($v=1$)(18 _{9,9} \rightarrow 17 _{9,8})E	342					
219.798	HNCO($v=0$)(10 _{0,10} \rightarrow 9 _{0,9})	58	†				
219.822	HCOOCH ₃ ($v=1$)(18 _{10,9} \rightarrow 17 _{10,8})A	355	*	219.822	HCOOCH ₃ ($v=1$)(18 _{10,8} \rightarrow 17 _{10,7})A	355	
219.827	HCOOCH ₃ ($v=1$)(18 _{12,7} \rightarrow 17 _{12,6})E	384					
219.909	H ¹³ CO(3 _{1,2} \rightarrow 2 _{1,1})	33	†				
219.949	SO($v=0$)(6 ₅ \rightarrow 5 ₄)	35	†				
219.984	CH ₃ OH($v_1=0$)(25 _{3,22} \rightarrow 24 _{4,20})E	802					
219.994	CH ₃ OH($v_1=0$)(23 _{5,19} \rightarrow 22 _{6,17})E	776					
220.030	HCOOCH ₃ ($v=1$)(18 _{9,10} \rightarrow 17 _{9,9})A	342	*	220.030	HCOOCH ₃ ($v=1$)(18 _{9,9} \rightarrow 17 _{9,8})A	342	
220.043	HCOOCH ₃ ($v=1$)(18 _{11,8} \rightarrow 17 _{11,7})E	368					
220.078	CH ₃ OH($v_1=0$)(8 _{0,8} \rightarrow 7 _{1,6})E	97					
220.154	t-CH ₃ CH ₂ OH(24 _{3,22} \rightarrow 24 _{2,23})	263					
220.167	HCOOCH ₃ ($v=0$)(17 _{4,13} \rightarrow 16 _{4,12})E	103	‡				
220.178	CH ₂ CO(11 _{1,11} \rightarrow 10 _{1,10})	76	†				
220.190	HCOOCH ₃ ($v=0$)(17 _{4,13} \rightarrow 16 _{4,12})A	103					
220.258	HCOOCH ₃ ($v=1$)(18 _{8,10} \rightarrow 17 _{8,9})E	330	‡				
220.296	CH ₃ ¹³ CN(12 ₉ \rightarrow 11 ₉)	646					
220.307	HCOOCH ₃ ($v=1$)(18 _{10,9} \rightarrow 17 _{10,8})E	354					
220.324	CH ₃ CN($v=0$)(12 ₁₀ \rightarrow 11 ₁₀)	782					
220.355	CH ₃ COCH ₃ ($v=0$)(22 _{0,22} \rightarrow 21 _{0,21})	124	AE,EA*	220.355	CH ₃ COCH ₃ ($v=0$)(22 _{1,22} \rightarrow 21 _{1,21})	124	AE,EA
				220.355	C ₆ H(J = 159/2-157/2, $\Omega=3/2$, l=e)	425	?
220.362	CH ₃ COCH ₃ ($v=0$)(22 _{0,22} \rightarrow 21 _{1,21})EE	124	*	220.362	CH ₃ COCH ₃ ($v=0$)(22 _{1,22} \rightarrow 21 _{1,21})EE	124	
				220.362	CH ₃ COCH ₃ ($v=0$)(22 _{1,22} \rightarrow 21 _{0,21})EE	124	
				220.362	CH ₃ COCH ₃ ($v=0$)(22 _{0,22} \rightarrow 21 _{0,21})EE	124	

220.368	HCOOCH ₃ ($\nu=1$)(18 _{8,11} → 17 _{8,10})A	331	*	220.370	HCOOCH ₃ ($\nu=1$)(18 _{8,10} → 17 _{8,9})A	331	
				220.368	CH ₃ COCH ₃ ($\nu=0$)(22 _{1,22} → 21 _{1,21})AA	124	
				220.368	CH ₃ COCH ₃ ($\nu=0$)(22 _{0,22} → 21 _{0,21})AA	124	
				220.368	CH ₃ ¹³ CN(12 ₈ → 11 ₈)	526	
220.399	¹³ CO(2 → 1)	16	†				
220.404	CH ₃ CN($\nu=0$)(12 ₉ → 11 ₉)	646					
220.416	HCOOCH ₃ ($\nu=1$)(18 _{3,16} → 17 _{2,15})A	293					
220.431	CH ₃ ¹³ CN(12 ₇ → 11 ₇)	417	*	220.433	HCOOCH ₃ ($\nu=0$)(35 _{5,28} → 33 _{5,29})A	357	
220.446	CH ₃ CHO(13 _{3,10} → 13 _{2,11} $\nu=0$)E	105	?‡				
220.465	CH ₃ COCH ₃ ($\nu=0$)(11 _{11,1} → 10 _{10,0})AE	63	*	220.466	CH ₃ COCH ₃ ($\nu=0$)(11 _{11,0} → 10 _{10,1})AE	63	
220.476	CH ₃ CN($\nu=0$)(12 ₈ → 11 ₈)	526					
220.486	CH ₃ ¹³ CN(12 ₆ → 11 ₆)	326	*	220.487	C ₆ H($J=159/2-157/2$, $\Omega=3/2$, $l=f$)	426	?
220.525	HCOOCH ₃ ($\nu=1$)(10 _{4,6} → 9 _{3,7})A	231					
220.533	CH ₃ ¹³ CN(12 ₅ → 11 ₅)	247					
220.539	CH ₃ CN($\nu=0$)(12 ₇ → 11 ₇)	419					
220.561	CH ₂ CHCN(24 _{1,24} → 23 _{1,23})	134					
220.570	CH ₃ ¹³ CN(12 ₄ → 11 ₄)	183					
220.585	HNCO($\nu=0$)(10 _{1,9} → 9 _{1,8})	101					
220.594	CH ₃ CN($\nu=0$)(12 ₆ → 11 ₆)	326					
220.621	CH ₃ ¹³ CN(12 ₂ → 11 ₂)	97	‡				
220.641	CH ₃ CN($\nu=0$)(12 ₅ → 11 ₅)	248					
220.661	CH ₃ CH ₂ CN($\nu=0$)(25 _{2,24} → 24 _{2,23})	143					
220.679	CH ₃ CN($\nu=0$)(12 ₄ → 11 ₄)	183					
220.709	CH ₃ CN($\nu=0$)(12 ₃ → 11 ₃)	133					
220.730	CH ₃ CN($\nu=0$)(12 ₂ → 11 ₂)	98	‡				
220.743	CH ₃ CN($\nu=0$)(12 ₁ → 11 ₁)	76					
220.747	CH ₃ CN($\nu=0$)(12 ₀ → 11 ₀)	69					
220.764	CH ₃ COCH ₃ ($\nu=0$)(11 _{11,0} → 10 _{10,0})EE	63					
220.786	HCOOCH ₃ ($\nu=0$)(28 _{3,25} → 28 _{3,26})E	248					
220.812	HCOOCH ₃ ($\nu=0$)(18 _{3,16} → 17 _{2,15})E	105					
220.815	HCOOCH ₃ ($\nu=0$)(18 _{3,16} → 17 _{2,15})A	105					
220.820	HCOOCH ₃ ($\nu=0$)(24 _{2,23} → 24 _{1,24})A	169					
220.848	CH ₃ OCH ₃ (24 _{4,20} → 23 _{5,19})	297	A(E)A(E)				
220.866	HCOOCH ₃ ($\nu=0$)(28 _{3,25} → 28 _{3,26})A	248	*	220.866	HCOOCH ₃ ($\nu=1$)(19 _{2,17} → 18 _{3,16})A	303	
220.889	HCOOCH ₃ ($\nu=0$)(18 _{7,1} → 17 _{17,0})A	293	*	220.889	HCOOCH ₃ ($\nu=0$)(18 _{7,2} → 17 _{17,1})A	293	
220.893	CH ₃ OCH ₃ (23 _{4,20} → 23 _{3,21})	274	A(E)A(E)				
220.901	HCOOCH ₃ ($\nu=0$)(18 _{7,1} → 17 _{17,0})E	293					
220.913	HCOOCH ₃ ($\nu=1$)(18 _{7,12} → 17 _{17,1})A	320	*	220.910	HCOOCH ₃ ($\nu=0$)(18 _{7,2} → 17 _{17,1})E	293	
220.926	HCOOCH ₃ ($\nu=0$)(18 _{16,2} → 17 _{16,1})A	271	*	220.926	HCOOCH ₃ ($\nu=0$)(18 _{16,3} → 17 _{16,2})A	271	
220.935	HCOOCH ₃ ($\nu=0$)(18 _{16,2} → 17 _{16,1})E	271					
220.946	HCOOCH ₃ ($\nu=1$)(18 _{7,11} → 17 _{17,0})A	321	*	220.947	HCOOCH ₃ ($\nu=0$)(18 _{16,3} → 17 _{16,2})E	271	
220.967	HC ₇ N($\nu=0$)($J=196-195$)	1045	?				
220.978	HCOOCH ₃ ($\nu=0$)(18 _{15,4} → 17 _{15,3})A	250	*	220.978	HCOOCH ₃ ($\nu=0$)(18 _{15,3} → 17 _{15,2})A	250	
220.985	HCOOCH ₃ ($\nu=1$)(18 _{7,11} → 17 _{17,0})E	320	*	220.984	HCOOCH ₃ ($\nu=0$)(18 _{15,3} → 17 _{15,2})E	250	
220.998	HCOOCH ₃ ($\nu=0$)(18 _{15,4} → 17 _{15,3})E	250	*	220.999	g-CH ₃ CH ₂ OH(13 _{0,13} → 12 _{0,12} , $\nu_t=0-1$)	136	
221.048	HCOOCH ₃ ($\nu=0$)(18 _{14,5} → 17 _{14,4})A	231	*	221.048	HCOOCH ₃ ($\nu=0$)(18 _{14,4} → 17 _{14,3})A	231	
				221.048	HCOOCH ₃ ($\nu=0$)(18 _{14,4} → 17 _{14,3})E	231	
221.067	HCOOCH ₃ ($\nu=0$)(18 _{14,5} → 17 _{14,4})A	231					
221.076	HCOOCH ₃ ($\nu=0$)(29 _{9,21} → 29 _{8,22})A	312					
221.086	HCOOCH ₃ ($\nu=0$)(29 _{9,21} → 29 _{8,22})E	312					
221.111	HCOOCH ₃ ($\nu=1$)(18 _{8,11} → 17 _{8,10})E	330					
221.115	³⁴ SO ₂ ($\nu=0$)(22 _{2,20} → 22 _{1,21})	248					
221.124	CH ₂ CHCN($\nu=0$)(23 _{1,22} → 22 _{1,21})	130					
221.140	HCOOCH ₃ ($\nu=0$)(18 _{13,5} → 17 _{13,4})E	213	*	221.141	HCOOCH ₃ ($\nu=0$)(18 _{13,5} → 17 _{13,4})A	213	
				221.141	HCOOCH ₃ ($\nu=0$)(18 _{13,6} → 17 _{13,5})A	213	
229.056	CH ₃ COCH ₃ ($\nu=0$)(22 _{1,21} → 21 _{2,20})EE	133	*	229.056	CH ₃ COCH ₃ ($\nu=0$)(22 _{1,21} → 21 _{1,20})EE	133	
				229.056	CH ₃ COCH ₃ ($\nu=0$)(22 _{2,21} → 21 _{2,20})EE	133	
229.078	CH ₃ COCH ₃ ($\nu=0$)(22 _{1,21} → 21 _{2,20})AA	133	*	229.056	CH ₃ COCH ₃ ($\nu=0$)(22 _{2,21} → 21 _{1,20})EE	133	
229.087	CH ₂ CHCN($\nu=0$)(24 _{3,21} → 23 _{3,20})	156		229.058	CH ₃ COCH ₃ ($\nu=0$)(14 _{9,6} → 13 _{8,5})EE	85	
229.117	HCOOCH ₃ ($\nu=1$)(19 _{3,17} → 18 _{2,16})E	303		229.078	CH ₃ COCH ₃ ($\nu=0$)(22 _{2,21} → 21 _{1,20})AA	133	
229.127	CH ₃ COCH ₃ ($\nu=0$)(12 _{10,2} → 11 _{9,2})EE	68					
229.134	CH ₃ CHO(9 _{3,7} → 9 _{2,7})	62					
229.203	UL		?				
229.224	HCOOCH ₃ ($\nu=0$)(23 _{9,14} → 23 _{8,15})A	217					
229.259	HCOOCH ₃ ($\nu=0$)(23 _{9,14} → 23 _{8,15})E	217	*	229.258	CH ₃ CHO(10 _{3,7} → 10 _{2,8})	71	
229.265	CH ₃ CH ₂ CN($\nu=0$)(26 _{2,25} → 25 _{5,24})	154	‡				
229.320	HCOOCH ₃ ($\nu=0$)(23 _{9,15} → 23 _{8,16})E	217					
229.348	SO ₂ ($\nu=0$)(11 _{5,7} → 12 _{4,8})	122	†				
229.389	HCOOCH ₃ ($\nu=0$)(23 _{9,15} → 23 _{8,16})A	217					
229.405	HCOOCH ₃ ($\nu=0$)(18 _{3,15} → 17 _{3,14})E	111					
229.420	HCOOCH ₃ ($\nu=0$)(18 _{3,15} → 17 _{3,14})A	111					
229.474	HCOOCH ₃ ($\nu=0$)(20 _{3,17} → 19 _{4,16})E	134					
229.491	t-CH ₃ CH ₂ OH(17 _{5,12} → 17 _{4,13})	160	*	229.498	g-CH ₃ CH ₂ OH(41 _{11,31} → 40 _{12,29} , $\nu_t=1-0$)	925	
				229.498	g-CH ₃ CH ₂ OH(41 _{11,30} → 40 _{12,28} , $\nu_t=1-0$)	925	
229.505	HCOOCH ₃ ($\nu=0$)(20 _{3,17} → 19 _{4,16})A	134					

229.539	HCOOCH ₃ ($\nu=0$)(31 _{5,27} → 31 _{3,28})E	309					
229.589	CH ₃ OH($\nu_1=0$)(15 _{4,11} → 16 _{3,13})E	374					
229.607	HCOOCH ₃ ($\nu=0$)(31 _{5,27} → 31 _{3,28})A	309					
229.648	CH ₂ CHCN($\nu=0$)(25 _{1,25} → 24 _{1,24})	146					
229.661	HCOOCH ₃ ($\nu=1$)(25 _{9,16} → 25 _{8,17})A	432					
229.759	CH ₃ OH($\nu_1=0$)(8 _{-1,8} → 7 _{0,7})E	89		‡			
229.858	³⁴ SO ₂ ($\nu=0$)(4 _{2,2} → 3 _{1,3})	19					
229.864	CH ₃ OH($\nu_1=0$)(19 _{5,15} → 20 _{4,16})A ++	578					
229.888	³⁴ SO ₂ ($\nu=0$)(17 _{3,15} → 18 _{0,18})	162					
229.939	CH ₃ OH($\nu_1=0$)(19 _{5,14} → 20 _{4,17})A --	578					
229.987	³⁴ SO ₂ ($\nu=0$)(42 _{6,36} → 41 _{7,35})	921					
230.027	CH ₃ OH($\nu_1=0$)(3 _{-2,2} → 4 _{-1,4})E	40					
230.109	C ₆ H(J = 165/2-163/2, Ω=1/2, l=f)	482		? ‡			
230.140	CH ₃ OCH ₃ (25 _{4,22} → 25 _{3,22})EA	319	A(E)A(E)‡				
230.170	CH ₃ COCH ₃ ($\nu=0$)(23 _{0,23} → 22 _{1,22})AE	135	*		230.170	CH ₃ COCH ₃ ($\nu=0$)(23 _{1,23} → 22 _{0,22})AE	135
					230.170	CH ₃ COCH ₃ ($\nu=0$)(23 _{0,23} → 22 _{0,22})EA	135
					230.170	CH ₃ COCH ₃ ($\nu=0$)(23 _{1,23} → 22 _{1,22})EA	135
230.177	CH ₃ COCH ₃ ($\nu=0$)(23 _{0,23} → 22 _{1,22})EE	135	*		230.177	CH ₃ COCH ₃ ($\nu=0$)(23 _{1,23} → 22 _{0,22})EE	135
					230.177	CH ₃ COCH ₃ ($\nu=0$)(23 _{0,23} → 22 _{0,22})EE	135
					230.177	CH ₃ COCH ₃ ($\nu=0$)(23 _{1,23} → 22 _{1,22})EE	135
230.183	CH ₃ COCH ₃ ($\nu=0$)(23 _{0,23} → 22 _{1,22})AA	135	‡*		230.183	CH ₃ COCH ₃ ($\nu=0$)(23 _{1,23} → 22 _{0,22})AA	135
230.234	CH ₃ OCH ₃ (17 _{2,15} → 16 _{3,14})	148	A(E)A(E)		230.234	C ₆ H(J = 165/2-163/2, Ω=1/2, l=e)	483 ?
230.283	CH ₃ COCH ₃ ($\nu=0$)(16 _{8,8} → 15 _{9,7})EE	107					
230.293	CH ₃ OH($\nu_1=0$)(22 _{2,20} → 21 _{-3,19})E	609					
230.318	O ¹³ CS(19 → 18)	111	†				
230.369	CH ₃ OH($\nu_1=0$)(22 _{4,18} → 21 _{5,17})E	683					
230.377	HCOOCH ₃ ($\nu=0$)(22 _{9,14} → 22 _{8,15})A	203					
230.436	HCOOCH ₃ ($\nu=0$)(25 _{1,24} → 25 _{1,25})E	182	*		230.436	HCOOCH ₃ ($\nu=0$)(25 _{1,24} → 25 _{0,25})E	182
230.441	HCOOCH ₃ ($\nu=0$)(25 _{2,24} → 25 _{1,25})E	182	*		230.441	HCOOCH ₃ ($\nu=0$)(25 _{2,24} → 25 _{0,25})E	182
230.481	CH ₃ OCH ₃ (10 _{8,2} → 11 _{7,5})EE	140	*		230.474	CH ₃ OCH ₃ (10 _{8,3} → 11 _{7,4})EA	140
					230.476	CH ₃ OCH ₃ (10 _{8,3} → 11 _{7,4})EE	140
					230.478	CH ₃ OCH ₃ (10 _{8,3} → 11 _{7,4})AA	140
					230.478	CH ₃ OCH ₃ (10 _{8,2} → 11 _{7,5})AA	140
					230.479	CH ₃ OCH ₃ (10 _{8,3} → 11 _{7,4})AE	140
					230.479	CH ₃ OCH ₃ (10 _{8,2} → 11 _{7,5})AE	140
					230.483	CH ₃ OCH ₃ (10 _{8,2} → 11 _{7,5})EA	140
230.488	CH ₂ CHCN($\nu=0$)(24 _{1,23} → 23 _{1,22})	141					
230.505	CH ₃ OCH ₃ (26 _{4,23} → 25 _{5,20})	343	A(E)A(E)				
230.538	CO($\nu=0$)(2 → 1)	17	†				
230.673	g-CH ₃ CH ₂ OH(13 _{2,11} → 12 _{2,10} , $\nu_t = 0 - 0$)	139					
230.697	g-CH ₃ CH ₂ OH(8 _{3,5} → 8 _{2,7} , $\nu_t = 1 - 0$)	103					
230.739	CH ₂ CHCN($\nu=0$)(25 _{0,25} → 24 _{0,24})	146	‡				
230.794	g-CH ₃ CH ₂ OH(6 _{5,1} → 5 _{4,1} , $\nu_t = 0 - 1$)	105	*		230.794	g-CH ₃ CH ₂ OH(6 _{5,2} → 5 _{4,2} , $\nu_t = 0 - 1$)	105
230.844	HCOOCH ₃ ($\nu=1$)(19 _{17,2} → 18 _{17,1})E	493					
230.852	HCOOCH ₃ ($\nu=1$)(19 _{16,3} → 18 _{16,2})E	470					
230.879	HCOOCH ₃ ($\nu=1$)(18 _{4,14} → 17 _{4,13})A	301					
230.889	HCOOCH ₃ ($\nu=1$)(19 _{15,4} → 18 _{15,3})E	450					
230.933	³⁴ SO ₂ ($\nu=0$)(5 _{4,2} → 6 _{3,3})	52	*		230.936	HCOOCH ₃ ($\nu=0$)(29 _{3,26} → 29 _{2,27})E	265
230.954	t-CH ₃ CH ₂ OH(16 _{5,11} → 16 _{4,12})	145					
230.960	HCOOCH ₃ ($\nu=1$)(19 _{14,5} → 18 _{14,4})E	430					
230.991	t-CH ₃ CH ₂ OH(14 _{0,14} → 13 _{1,13})	86	*‡		230.992	g-CH ₃ CH ₂ OH(6 _{5,1} → 6 _{4,2} , $\nu_t = 1 - 1$)	110
					230.993	g-CH ₃ CH ₂ OH(6 _{5,2} → 6 _{4,3} , $\nu_t = 1 - 1$)	110
231.019	HCOOCH ₃ ($\nu=0$)(12 _{4,9} → 11 _{3,8})E	57	*		231.020	HCOOCH ₃ ($\nu=0$)(29 _{3,26} → 29 _{2,27})A	264
231.046	HCOOCH ₃ ($\nu=0$)(12 _{4,9} → 11 _{3,8})A	57					
231.061	OCS($\nu=0$)(19 → 18)	111	†				
231.102	HC ₇ N(J = 205 - 204)	1142	?‡				
231.188	HCOOCH ₃ ($\nu=0$)(21 _{9,13} → 21 _{8,14})E	190					
231.199	HCOOCH ₃ ($\nu=0$)(21 _{9,12} → 21 _{8,13})A	190	*		231.199	HCOOCH ₃ ($\nu=0$)(21 _{9,12} → 21 _{8,13})E	190
231.221	¹³ CS($\nu=0$)(5 → 4)	33	†				
231.231	HCOOCH ₃ ($\nu=1$)(19 _{12,7} → 18 _{12,6})E	396			231.231	g-CH ₃ CHO(12 _{8,5} → 11 _{8,4})E	216

Note. 1. Due to the frequency resolution (0.8125 MHz, $\sim 1.2\text{km s}^{-1}$), lines with broad FWHM width can be attributed to different species, so lines with stronger CDMS/JPL intensity are listed here in the left column with “*”, and the potential blended weaker transitions are listed in the right column.
2. Tentative detections and unidentified lines are marked with “?”.
3. Lines with “†” are imaged in Figure 4, with “‡” are imaged in Figure 5.
4. “A(E)A(E)” represents 4 types of transitions are possible: AA, EE, AE, EA.

Table A2: Laboratory parameters of CH_3CN and $\text{CH}_3^{13}\text{CN}$ and the intensity integrated over the width of each line $\int T_{\text{B}}(\nu) d\nu$, which is used for rotation diagrams in Figure 8. Uncertainties on the measured intensities are typically $\leq 10\%$ (written as the subscript), as determined from Gaussian fitting.

Mol.	Freq (GHz)	K	I(300K) Log10	E_{L} (cm^{-1})	$S_{\text{ul}}\mu^2$ (D^2)	o/p-	HC (K km s $^{-1}$)	mm2 (K km s $^{-1}$)	mm3a (K km s $^{-1}$)	mm3b (K km s $^{-1}$)	NE (K km s $^{-1}$)	Note
CH_3CN ($J = 12 \rightarrow 11$)	220.476	8	-3.098	357.938	205.033	p-	73.64 $_{\pm 2.81}$	16.46 $_{\pm 1.14}$	11.22 $_{\pm 0.85}$	7.67 $_{\pm 1.06}$	≤ 0.31	1, 2, 3, 4
	220.539	7	-2.868	283.608	243.499	p-	144.31 $_{\pm 3.70}$	49.48 $_{\pm 1.90}$	27.68 $_{\pm 1.16}$	33.72 $_{\pm 1.52}$	≤ 0.61	
	220.594	6	-2.377	219.154	553.690	o-	356.10 $_{\pm 7.70}$	150.47 $_{\pm 10.38}$	90.69 $_{\pm 11.98}$	190.53 $_{\pm 2.74}$	0.71 $_{\pm 0.53}$	
	220.641	5	-2.522	164.592	305.047	p-	327.23 $_{\pm 32.55}$	146.62 $_{\pm 4.76}$	106.37 $_{\pm 10.00}$	178.31 $_{\pm 5.00}$	1.34 $_{\pm 0.63}$	
	220.679	4	-2.397	119.933	328.188	p-	307.21 $_{\pm 25.39}$	150.29 $_{\pm 5.73}$	142.61 $_{\pm 2.77}$	170.24 $_{\pm 10.00}$	5.11 $_{\pm 0.36}$	
	220.709	3	-2.001	85.187	692.234	o-	484.10 $_{\pm 10.61}$	209.82 $_{\pm 15.40}$	278.38 $_{\pm 7.16}$	319.87 $_{\pm 13.08}$	11.92 $_{\pm 0.56}$	
	220.730	2	-2.234	60.363	358.988	p-	397.54 $_{\pm 9.19}$	281.55 $_{\pm 10.27}$	256.41 $_{\pm 27.26}$	331.98 $_{\pm 21.20}$	15.17 $_{\pm 1.00}$	
	220.743	1	-2.194	45.467	366.614	p-	371.68 $_{\pm 28.18}$	229.32 $_{\pm 8.17}$	247.64 $_{\pm 10.46}$	284.65 $_{\pm 25.77}$	13.52 $_{\pm 0.66}$	
	220.747	0	-2.180	40.501	369.277	p-	372.96 $_{\pm 28.18}$	211.34 $_{\pm 4.55}$	255.62 $_{\pm 1.40}$	348.84 $_{\pm 25.77}$	11.19 $_{\pm 0.37}$	
	220.431	7	-2.707	283.596	243.492	p-	4.07 $_{\pm 1.61}$					
$\text{CH}_3^{13}\text{CN}$ ($J = 12 \rightarrow 11$)	220.485	6	-2.216	219.141	553.669	o-	14.29 $_{\pm 1.28}$					2, 3, 5
	220.532	5	-2.361	164.575	305.101	p-	16.78 $_{\pm 1.80}$					
	220.570	4	-2.236	119.915	328.169	p-	27.41 $_{\pm 1.75}$					
	220.621	2	-2.073	60.344	358.964	p-	96.44 $_{\pm 4.41}$					

Notes: 1. None detection is given by an upper limit of 3σ rms.

2. Integrated intensities are obtained by Gildas “Gaussian” fittings.

3. Laboratory parameters are given from CDMS.

4. Q(300K, CH_3CN)=14683.6324

5. Q(300K, $\text{CH}_3^{13}\text{CN}$)=199602.70

Table A3: The laboratory parameters and the intensity integrated over the width of each line $\int T_B(\nu)d\nu$, which is used for rotation diagrams in Figure 9. Uncertainties on the measured intensities are typically $\leq 10\%$ (written as the subscript), as determined from Gaussian or HFS fitting.

Mol.	Freq (GHz)	\log_{10}	E_L (cm^{-1})	$S_{ul}\mu^2$ (D^2)	HC (K km s^{-1})	mm2 (K km s^{-1})	mm3a (K km s^{-1})	mm3b (K km s^{-1})	Notes
HCOOCH_3 ($\nu = 1$)	218.966	-4.619	259.918	53.255	2.17 \pm 0.92	2.25 \pm 0.00	2.87 \pm 0.75	6.32 \pm 1.03	
	219.155	-4.543	249.175	60.055	6.26 \pm 0.74	4.81 \pm 0.43	6.26 \pm 0.58	9.44 \pm 0.55	
	219.479	-4.813	283.781	38.005	—	—	0.82 \pm 0.24	2.06 \pm 0.39	
	219.584	-4.704	271.154	45.955	3.18 \pm 0.48	3.05 \pm 0.63	7.04 \pm 0.63	10.08 \pm 0.77	
	219.623	-4.615	259.539	53.333	4.81 \pm 0.98	5.55 \pm 0.30	8.12 \pm 0.56	12.94 \pm 0.94	
	219.642	-4.703	271.148	46.014	—	—	1.90 \pm 0.35	3.39 \pm 0.42	
	219.696	-4.540	248.860	60.113	6.14 \pm 0.79	6.47 \pm 1.07	9.24 \pm 0.43	14.74 \pm 0.62	
	219.705	-4.262	200.469	90.462	28.88 \pm 5.46	12.16 \pm 0.89	9.88 \pm 0.34	18.45 \pm 0.46	
	219.764	-4.424	230.499	71.907	6.03 \pm 1.97	6.18 \pm 0.49	6.27 \pm 0.40	11.04 \pm 0.34	
	219.822	-4.477	239.119	66.281	3.61 \pm 1.27	5.22 \pm 0.64	9.10 \pm 0.86	14.66 \pm 1.09	
	219.827	-4.613	259.457	53.422	1.80 \pm 0.36	1.50 \pm 0.45	2.70 \pm 0.71	5.69 \pm 0.92	
	220.030	-4.423	230.319	71.871	5.86 \pm 0.61	8.35 \pm 0.70	12.28 \pm 1.32	20.35 \pm 1.32	
	220.043	-4.537	248.708	60.241	1.41 \pm 0.56	2.99 \pm 0.93	2.73 \pm 0.00	5.84 \pm 0.81	
	220.258	-4.376	222.578	76.973	7.52 \pm 0.88	6.85 \pm 0.70	10.65 \pm 0.67	16.40 \pm 1.02	
	220.307	-4.473	238.906	66.458	3.04 \pm 0.66	4.45 \pm 0.47	4.91 \pm 0.35	9.25 \pm 0.40	
	220.368	-4.376	222.466	76.856	12.33 \pm 3.46	15.04 \pm 2.53	19.00 \pm 1.36	32.09 \pm 1.55	
	220.914	-4.335	215.570	81.244	7.70 \pm 1.43	11.26 \pm 0.80	13.42 \pm 1.22	21.02 \pm 1.34	
	220.946	-4.335	215.571	81.239	9.18 \pm 1.53	11.30 \pm 1.40	18.88 \pm 0.53	31.07 \pm 0.91	
	220.985	-4.334	215.616	81.434	11.98 \pm 4.04	15.49 \pm 5.21	14.17 \pm 2.53	27.29 \pm 4.45	
	221.111	-4.371	222.159	77.098	—	—	12.95 \pm 2.31	19.97 \pm 1.96	
	230.879	-4.218	201.531	91.238	4.79 \pm 1.00	8.03 \pm 1.53	11.76 \pm 0.68	22.34 \pm 0.71	1, 2, 3, 4
HCOOCH_3 ($\nu = 0$)	219.417	-5.168	195.355	10.989	—	—	1.57 \pm 0.30	3.66 \pm 0.38	
	219.484	-5.168	195.354	10.980	—	—	2.00 \pm 0.44	3.32 \pm 0.43	
	219.592	-5.055	197.439	14.378	0.90 \pm 0.39	1.32 \pm 0.32	2.77 \pm 0.85	5.16 \pm 1.00	
	220.167	-3.999	64.350	85.865	38.44 \pm 2.34	36.01 \pm 2.02	57.74 \pm 1.44	78.96 \pm 1.40	
	220.190	-3.999	64.344	85.884	24.45 \pm 1.42	35.99 \pm 1.39	60.42 \pm 2.36	78.54 \pm 2.59	
	220.812	-4.986	66.218	8.871	5.91 \pm 0.00	6.77 \pm 0.98	10.22 \pm 0.36	15.57 \pm 0.85	
	220.815	-4.987	66.210	8.869	5.24 \pm 0.00	4.09 \pm 0.93	8.71 \pm 0.33	18.34 \pm 0.93	
	220.926	-4.867	180.745	20.185	4.25 \pm 0.75	7.14 \pm 0.54	9.34 \pm 1.30	14.46 \pm 1.19	
	220.935	-4.867	180.739	20.183	5.12 \pm 0.93	2.69 \pm 0.98	4.89 \pm 0.44	9.68 \pm 0.51	
	220.978	-4.675	166.459	29.375	—	—	11.64 \pm 1.66	20.14 \pm 2.81	
	220.998	-4.674	166.446	29.374	4.31 \pm 1.48	8.52 \pm 5.18	11.86 \pm 0.98	17.70 \pm 0.82	
	221.048	-4.535	153.092	37.964	15.11 \pm 1.64	30.75 \pm 0.98	45.62 \pm 0.93	73.34 \pm 1.07	
	221.067	-4.535	153.081	37.964	2.59 \pm 0.61	9.24 \pm 1.28	11.91 \pm 0.48	21.32 \pm 0.47	
	221.086	-5.051	209.447	15.138	1.75 \pm 0.61	1.43 \pm 0.35	3.45 \pm 1.09	5.03 \pm 0.81	
	221.140	-4.426	140.647	45.951	11.28 \pm 2.24	37.37 \pm 2.28	50.30 \pm 0.70	88.58 \pm 0.99	
	229.224	-5.027	143.199	10.854	—	—	2.71 \pm 0.60	5.09 \pm 0.53	
	229.259	-5.092	143.201	9.338	—	—	—	3.27 \pm 0.90	
	229.389	-5.026	143.193	10.851	8.04 \pm 0.00	4.31 \pm 0.80	2.99 \pm 0.27	6.82 \pm 0.46	
	229.405	-3.943	69.316	92.251	20.44 \pm 1.05	37.31 \pm 0.80	47.60 \pm 1.09	72.27 \pm 2.26	
	229.420	-3.943	69.310	92.257	25.89 \pm 1.12	37.54 \pm 1.04	47.68 \pm 1.72	73.39 \pm 1.86	
	230.377	-5.031	133.656	10.167	—	—	4.07 \pm 0.47	7.19 \pm 0.41	
	230.436	-5.566	118.982	2.761	1.40 \pm 0.01	—	1.79 \pm 0.05	3.20 \pm 0.01	
	230.441	-5.566	118.983	2.761	2.90 \pm 0.81	2.37 \pm 0.16	1.99 \pm 0.43	4.53 \pm 0.19	
	231.019	-5.268	31.810	3.599	1.69 \pm 0.73	5.69 \pm 0.83	8.45 \pm 0.51	14.60 \pm 0.91	
	231.046	-5.268	31.801	3.599	—	—	4.90 \pm 0.78	13.58 \pm 1.24	
	231.188	-5.043	124.543	9.415	2.81 \pm 0.83	—	4.06 \pm 0.84	5.91 \pm 0.76	
	231.199	-5.039	124.546	9.492	6.55 \pm 1.13	5.42 \pm 0.96	11.01 \pm 0.48	21.05 \pm 0.96	

Table A3: (continued)

Mol.	Freq (GHz)	I(300K) Log ₁₀	E _L (cm ⁻¹)	$S_{\mu\mu}^2$ (D ²)	HC (K km s ⁻¹)	mm2 (K km s ⁻¹)	mm3a (K km s ⁻¹)	mm3b (K km s ⁻¹)	Notes
CH ₃ OH	219.984	-4.527	550.204	12.441	23.44 \pm 0.53	5.96 \pm 0.96	9.44 \pm 0.60	6.13 \pm 1.28	3, 5, 6
	219.994	-4.591	531.938	9.844	18.37 \pm 1.44	8.99 \pm 3.00	6.88 \pm 0.57	10.65 \pm 2.33	
	220.078	-3.892	59.809	5.111	175.00 \pm 9.00	163.50 \pm 16.00	285.56 \pm 23.00	300.80 \pm 6.77	
	229.589	-4.132	252.591	6.806	106.85 \pm 2.03	56.47 \pm 0.95	94.80 \pm 16.00	114.36 \pm 3.63	
	229.759	-3.678	54.266	7.483	193.14 \pm 2.06	209.17 \pm 2.45	326.94 \pm 1.27	359.76 \pm 1.47	
	229.939	-4.332	394.477	8.463	38.47 \pm 1.03	14.97 \pm 0.68	27.50 \pm 1.10	28.46 \pm 0.71	
	230.027	-4.442	20.009	1.089	106.32 \pm 1.44	100.37 \pm 1.57	162.28 \pm 1.84	179.02 \pm 2.06	
	230.293	-5.130	415.980	1.487	7.48 \pm 1.02	6.23 \pm 1.70	8.19 \pm 1.58	14.36 \pm 1.60	
	230.368	-4.418	466.848	9.772	29.52 \pm 1.24	12.79 \pm 1.32	12.78 \pm 1.02	16.73 \pm 1.69	
	219.355	-3.036	34.438	20.782	192.87 \pm 6.47	177.38 \pm 3.74	78.92 \pm 1.48	103.15 \pm 2.72	
³⁴ SO ₂	221.115	-3.089	164.876	33.785	77.29 \pm 6.98	28.80 \pm 4.13	27.83 \pm 1.59	23.11 \pm 2.11	5, 7, 8, 9
	229.858	-3.595	5.311	4.548	145.14 \pm 3.13	79.54 \pm 2.07	32.57 \pm 2.65	30.12 \pm 3.15	
	229.888	-4.951	104.865	0.322	10.12 \pm 0.75	\leq 0.91	\leq 0.51	\leq 0.30	
	229.987	-4.310	631.573	17.640	4.01 \pm 0.85	1.78 \pm 0.44	\leq 0.75	\leq 1.20	
	230.933	-4.466	28.220	0.676	7.63 \pm 1.72	19.26 \pm 1.63	6.97 \pm 1.02	8.70 \pm 1.75	
	218.981	-2.677	62.949	70.596	145.59 \pm 1.40	49.86 \pm 1.43	42.52 \pm 1.70	47.57 \pm 3.08	
	219.657	-3.232	293.597	59.063	45.60 \pm 1.57	5.91 \pm 2.20	4.01 \pm 1.46	7.13 \pm 1.24	
	219.734	-2.887	151.337	66.112	155.14 \pm 2.02	26.39 \pm 0.78	13.81 \pm 0.45	15.35 \pm 0.42	
	219.737	-2.887	151.337	66.110	44.49 \pm 1.89	15.39 \pm 0.91	13.81 \pm 0.45	15.35 \pm 0.42	
	219.798	-2.602	32.994	72.127	263.86 \pm 3.43	120.56 \pm 4.15	105.66 \pm 1.53	131.98 \pm 2.02	
CH ₃ OCH ₃	220.585	-2.671	63.190	70.599	141.92 \pm 4.26	35.20 \pm 4.03	29.29 \pm 2.42	40.71 \pm 1.98	5, 8, 10, 11
	220.848	-4.939	199.405	21.418	4.77 \pm 1.13	5.27 \pm 1.55	7.41 \pm 0.97	10.65 \pm 1.63	
	220.893	-4.372	183.375	73.169	31.48 \pm 2.58	22.98 \pm 2.95	36.87 \pm 2.65	57.36 \pm 4.60	
	230.141	-4.374	214.188	77.819	11.12 \pm 1.27	14.20 \pm 1.01	21.92 \pm 0.64	27.49 \pm 0.85	
	230.234	-4.675	94.945	21.945	37.39 \pm 3.46	29.69 \pm 1.98	38.29 \pm 2.58	52.30 \pm 2.45	
	230.476	-5.794	89.617	1.622	5.79 \pm 1.80	3.75 \pm 0.88	3.88 \pm 0.82	7.47 \pm 0.95	
	220.155 [†]	-4.109	175.464	25.923	2.91 \pm 0.69	\leq 0.75	1.66 \pm 0.36	1.15 \pm 0.30	
	230.673 ^g	-3.995	88.651	20.283	3.09 \pm 0.71	2.23 \pm 1.45	5.06 \pm 0.74	4.41 \pm 0.81	
	230.794 ^g	-4.508	65.142	5.557	6.23 \pm 1.71	\leq 0.75	6.93 \pm 0.82	5.33 \pm 1.36	
	230.954 [†]	-4.098	93.618	16.339	5.74 \pm 1.69	3.36 \pm 0.98	11.65 \pm 1.27	6.88 \pm 1.35	
CH ₃ CH ₂ OH	230.991 [†]	-4.081	51.739	13.896	5.63 \pm 1.24	5.02 \pm 0.81	12.93 \pm 0.86	9.16 \pm 1.15	2, 3, 7, 13, 14

Notes: 1. None detection is marked with “—”.

2. Integrated intensities of multiplet (blending) are obtained by Gildas “HFS” fittings.

3. Laboratory parameters are given from JPL.

4. Q(300K, HCOOCH₃)=199602.70

5. Integrated intensities are obtained by Gildas “Gaussian” fittings.

6. Q(300K, CH₃OH)=9473.11987. None detection is given by an upper limit of 3 σ rms.

8. Laboratory parameters are given from CDMS.

9. Q(300K, ³⁴SO₂)=6020.75410. Lines marked with “*” are blended with HCOOCH₃ lines.

11. Q(300K, HNC)=7785.741

12. Q(300K, CH₃OCH₃)=22801613. Lines marked with “*t*” are trans-CH₃CH₂OH, with “*g*” are gauche-CH₃CH₂OH.14. Q(300K, CH₃CH₂OH)=45583.66

Species	Freq (GHz)	Integrated intensity $\int T_B(\nu) d\nu$ (K km s ⁻¹)							OFIS
		HC	mm2	mm3a	mm3b	NE	SR	OFIN	
CO §	230.538	3204.00 \pm 40.97	3411.50 \pm 8.27	1777.80 \pm 17.41	2346.00 \pm 15.90	3553.00 \pm 1.13	853.91 \pm 5.08	2062.80 \pm 10.77	1028.70 \pm 12.43
¹³ CO §	220.399	828.40 \pm 7.77	702.33 \pm 9.91	502.14 \pm 6.32	568.77 \pm 9.99	437.89 \pm 9.19	134.30 \pm 1.22	197.20 \pm 2.72	129.92 \pm 0.56
C ¹⁸ O §	219.560	126.00 \pm 4.23	108.00 \pm 4.61	79.10 \pm 2.41	83.60 \pm 4.07	79.00 \pm 1.55	24.40 \pm 0.34	26.20 \pm 0.52	13.90 \pm 0.47
H ¹³ CO	219.909	53.93 \pm 2.30	34.70 \pm 2.01	43.23 \pm 0.80	36.86 \pm 1.61	2.53 \pm 0.40	11.63 \pm 0.40	5.18 \pm 0.39	14.31 \pm 0.26
CH ₂ CO	220.178	14.44 \pm 2.31	9.02 \pm 2.39	23.11 \pm 2.52	17.00 \pm 4.34	1.27 \pm 0.26	5.58 \pm 0.30	1.32 \pm 0.20	2.54 \pm 0.26
CH ₃ OH	229.759	193.14 \pm 2.06	209.17 \pm 2.45	326.94 \pm 1.27	359.76 \pm 1.47	6.62 \pm 0.37	29.56 \pm 0.77	15.08 \pm 0.67	46.21 \pm 0.53
CH ₃ OH	229.939	38.47 \pm 1.03	14.97 \pm 0.68	27.50 \pm 1.10	28.46 \pm 0.71	\leq 0.25	\leq 0.32	\leq 0.17	\leq 0.28
HCOOCH ₃	220.258	7.52 \pm 0.88	6.85 \pm 0.70	10.65 \pm 0.67	16.40 \pm 1.02	\leq 0.24	\leq 0.34	\leq 0.28	\leq 0.29
HCOOCH ₃	220.167	38.44 \pm 2.34	36.01 \pm 2.02	57.74 \pm 1.44	78.96 \pm 1.40	\leq 43.22	3.97 \pm 0.30	\leq 0.34	\leq 0.04
CH ₃ OCH ₃	230.141	11.12 \pm 1.27	14.20 \pm 1.01	21.92 \pm 0.64	21.49 \pm 0.85	\leq 0.21	\leq 0.28	\leq 0.21	\leq 0.25
CH ₃ COCH ₃	230.183	6.72 \pm 0.86	4.12 \pm 0.51	1.20 \pm 0.40	1.70 \pm 0.49	\leq 0.15	\leq 0.15	\leq 0.16	\leq 0.10
CH ₃ CH ₂ OH	230.991	5.63 \pm 1.24	5.02 \pm 0.81	12.93 \pm 0.86	9.16 \pm 1.15	\leq 0.47	\leq 0.66	\leq 0.51	\leq 0.38
CH ₃ CHO *	220.446	3.50 \pm 0.68	4.33 \pm 0.72	6.93 \pm 0.53	7.82 \pm 0.77	\leq 0.37	2.79 \pm 0.34	\leq 0.14	1.24 \pm 0.22
C ₆ H *	230.109	10.46 \pm 0.92	2.08 \pm 0.80	\leq 0.22	\leq 0.44	\leq 0.92	\leq 0.34	\leq 0.60	\leq 0.08
HNCO	219.798	263.86 \pm 3.43	120.56 \pm 4.15	105.66 \pm 1.53	131.98 \pm 2.02	22.61 \pm 1.08	1.68 \pm 0.28	9.65 \pm 0.28	13.94 \pm 0.40
HC ₃ N($\nu_7 = 1$)	219.174	227.01 \pm 2.74	70.10 \pm 2.64	27.10 \pm 2.77	19.87 \pm 2.36	\leq 0.51	\leq 0.48	\leq 0.38	\leq 0.61
CH ₃ CN	220.730	397.54 \pm 9.19	281.55 \pm 10.27	256.41 \pm 27.26	331.98 \pm 21.20	15.17 \pm 1.00	8.98 \pm 2.42	5.32 \pm 2.84	5.27 \pm 2.19
CH ¹³ CN	220.621	96.44 \pm 4.41	40.71 \pm 3.12	28.38 \pm 2.19	37.73 \pm 2.46	3.13 \pm 0.50	\leq 0.19	\leq 0.39	\leq 0.17
CH ₂ CHCN	230.739	48.99 \pm 0.90	6.68 \pm 0.96	\leq 0.28	\leq 0.45	\leq 0.37	\leq 0.23	\leq 0.10	\leq 0.48
CH ₃ CH ₂ CN	229.265	160.64 \pm 1.52	60.39 \pm 1.36	16.99 \pm 1.18	33.60 \pm 2.38	\leq 0.30	\leq 0.33	\leq 0.36	\leq 0.31
HC ₇ N *	231.102	4.39 \pm 0.46	\leq 0.58	\leq 0.38	\leq 0.77	\leq 0.31	\leq 0.48	\leq 0.33	\leq 0.63
OCS	231.061	345.79 \pm 8.67	189.26 \pm 6.48	194.18 \pm 4.19	219.78 \pm 9.42	12.25 \pm 0.54	9.38 \pm 0.57	6.15 \pm 0.53	\leq 0.37
O ¹³ CS	230.318	23.84 \pm 0.84	19.77 \pm 1.21	14.54 \pm 0.91	28.06 \pm 1.26	\leq 0.38	\leq 0.47	\leq 0.14	\leq 0.19
SO ₂	229.348	295.36 \pm 3.65	225.41 \pm 3.96	120.92 \pm 3.94	166.97 \pm 3.86	54.45 \pm 1.15	\leq 0.33	\leq 0.25	\leq 0.30
³⁴ SO ₂	219.355	192.87 \pm 6.47	177.38 \pm 3.74	78.92 \pm 1.48	103.15 \pm 2.72	52.70 \pm 1.24	\leq 0.60	\leq 0.35	\leq 0.21
SO	219.949	2281.00 \pm 16.36	2244.90 \pm 24.92	1500.70 \pm 17.58	1981.60 \pm 19.50	1748.00 \pm 58.77	102.16 \pm 3.93	487.06 \pm 2.87	70.85 \pm 3.55
¹³ CS	231.221	108.47 \pm 1.87	66.13 \pm 1.40	73.18 \pm 1.25	62.71 \pm 3.86	6.23 \pm 0.45	15.05 \pm 0.33	3.01 \pm 0.35	\leq 0.51

Table A4: Intensity integrated over the width of each line, corresponding to the transitions shown in Figure A3. Most species are measured from Gaussian fittings, and uncertainties (written as the subscript) on the measured intensities are typically $\leq 10\%$. For those marked with “§”, integration is from the whole area because they have none-Gaussian profiles caused by strong self-absorption, and uncertainties are from their difference to Gaussian fitting. For species which are not detected, an upper limit equal to the 3σ rms is given. Species with “*” are tentative detected due to only one unblended line which has not been confirmed previously.

Table A5: Column densities and abundances for O-bearing molecules and carbon chains from different substructures in Orion-KL denoted in Figures 4 and 5.

Species	HC (126 ± 13 K)	mm2 (112 ± 7 K)	mm3a (101 ± 5 K)	mm3b (102 ± 5 K)	NE (43 ± 3 K)	SR (43 ± 3 K)	OFIN (43 ± 3 K)	OFIS (43 ± 3 K)
I. Column densities (in the form of $x \pm y(z) = (x \pm y) \times 10^2 \text{ cm}^{-2}$)								
C ¹⁸ O	2.14 \pm 0.13(17)	1.67 \pm 0.02(17)	1.11 \pm 0.01(17)	1.19 \pm 0.01(17)	5.90 \pm 0.10(16)	1.82 \pm 0.04(16)	1.96 \pm 0.03(16)	1.04 \pm 0.00(16)
CO	2.71 \pm 0.21(20)	2.57 \pm 0.13(20)	†	†	1.83 \pm 0.06(20)	†	†	†
13CO	2.31 \pm 0.19(18)	1.22 \pm 0.05(18)	†	†	7.52 \pm 0.12(17)	†	†	†
CH ₂ CO	8.26 \pm 0.57(14)	4.74 \pm 0.97(14)	1.12 \pm 0.08(15)	8.34 \pm 1.79(14)	4.86 \pm 1.11(13)	2.14 \pm 0.16(14)	5.07 \pm 0.87(13)	9.72 \pm 1.23(13)
H ₂ ¹³ CO ⁽¹⁾	9.86 \pm 0.85(14)	5.54 \pm 0.13(14)	6.05 \pm 0.24(14)	5.24 \pm 0.08(14)	1.53 \pm 0.17(13)	7.04 \pm 0.07(13)	3.14 \pm 0.09(13)	8.66 \pm 0.22(13)
CH ₃ CHO *	6.99 \pm 0.51(15)	7.74 \pm 0.79(15)	1.13 \pm 0.04(16)	1.29 \pm 0.08(16)	≤ 5.99(14)	4.54 \pm 0.87(15)	2.01 \pm 0.50(15)	2.01 \pm 0.50(15)
C ₆ H *	9.74 \pm 4.88(14)	2.71 \pm 1.96(14)	≤ 4.26(13)	≤ 7.89(13)	≤ 4.46(16)	≤ 1.66(16)	≤ 2.92(16)	≤ 4.09(15)
CH ₃ COCH ₃	5.43 \pm 0.82(15)	2.48 \pm 0.10(15)	5.61 \pm 1.14(14)	8.16 \pm 1.30(14)	≤ 9.47(13)	≤ 9.72(13)	≤ 1.02(14)	≤ 6.20(13)
HCOOCH ₃	2.69 ± 1.09(16)	3.55 ± 0.96(16)	5.64 ± 1.28(16)	9.73 ± 2.11(16)	≤ 3.84(16)	≤ 5.56(16)	≤ 4.59(16)	≤ 4.74(16)
CH ₃ OCH ₃	1.59 ± 0.76(17)	1.03 ± 0.10(17)	1.19 ± 0.29(17)	1.96 ± 0.71(17)	≤ 4.13(16)	≤ 5.63(16)	≤ 4.13(16)	≤ 5.04(16)
CH ₃ CH ₂ OH	7.56 ± 5.29(15)	3.09 ± 2.60(15)	7.92 ± 7.64(15)	5.74 ± 3.71(15)	≤ 2.52(14)	≤ 3.48(14)	≤ 2.69(14)	≤ 2.01(14)
H ₂ ¹³ CO ⁽²⁾	2.09 \pm 0.16(15)	9.53 \pm 0.51(14)	1.06 \pm 0.08(15)	9.13 \pm 0.83(14)	1.53 \pm 0.17(13)	7.04 \pm 0.07(13)	3.14 \pm 0.09(13)	8.66 \pm 0.22(13)
CH ₃ OH	2.53 ± 0.91(17)	1.64 ± 0.66(17)	2.49 ± 0.93(17)	2.85 ± 1.49(17)	1.49 \pm 0.13(15)	6.66 \pm 0.36(15)	3.40 \pm 0.25(15)	1.04 \pm 0.04(16)
II. Abundances (in the form of $x \pm y(z) = (x \pm y) \times 10^4$)								
C ¹⁸ O	1.79(−7)	1.79(−7)	1.79(−7)	1.79(−7)	1.79(−7)	1.79(−7)	1.79(−7)	1.79(−7)
CO	2.26 \pm 0.32(−4)	2.76 \pm 0.18(−4)	†	†	5.55 \pm 0.29(−4)	†	†	†
13CO	1.93 \pm 0.28(−6)	1.31 \pm 0.07(−6)	†	†	2.28 \pm 0.08(−6)	†	†	†
CH ₂ CO	6.90 \pm 0.93(−10)	5.09 \pm 1.13(−10)	1.81 \pm 0.15(−9)	1.25 \pm 0.28(−9)	1.48 \pm 0.37(−10)	2.10 \pm 0.21(−9)	4.64 \pm 0.89(−10)	1.68 \pm 0.22(−9)
H ₂ ¹³ CO ⁽¹⁾	8.24 \pm 1.27(−10)	5.94 \pm 0.22(−10)	9.73 \pm 0.51(−10)	7.89 \pm 0.17(−10)	4.64 \pm 0.60(−11)	6.92 \pm 0.23(−10)	2.87 \pm 0.13(−10)	1.49 \pm 0.04(−9)
CH ₃ CHO *	5.84 \pm 0.82(−9)	8.31 \pm 0.98(−9)	1.82 \pm 0.09(−8)	1.94 \pm 0.13(−8)	≤ 1.82(−9)	4.46 \pm 0.98(−8)	≤ 2.15(−9)	3.47 \pm 0.88(−8)
C ₆ H *	8.14 \pm 4.84(−10)	2.91 \pm 2.18(−10)	≤ 6.84(−11)	≤ 1.19(−10)	≤ 1.35(−7)	≤ 1.63(−7)	≤ 2.67(−7)	≤ 7.05(−8)
CH ₃ COCH ₃	4.54 \pm 1.01(−9)	2.66 \pm 0.15(−9)	9.02 \pm 1.96(−10)	1.23 \pm 0.23(−9)	≤ 2.87(−10)	≤ 9.55(−10)	≤ 9.29(−10)	≤ 1.07(−9)
HCOOCH ₃	2.25 ± 1.11(−8)	3.81 ± 1.10(−8)	9.06 ± 2.19(−8)	1.46 ± 0.33(−7)	≤ 1.16(−7)	≤ 5.46(−7)	≤ 4.20(−7)	≤ 8.18(−7)
CH ₃ OCH ₃	1.33 ± 0.76(−7)	1.10 ± 0.12(−7)	1.91 ± 0.50(−7)	2.94 ± 1.09(−7)	≤ 1.25(−7)	≤ 5.53(−7)	≤ 3.78(−7)	≤ 8.69(−7)
CH ₃ CH ₂ OH	6.32 ± 5.09(−9)	3.31 ± 2.88(−9)	1.27 ± 1.26(−8)	8.63 ± 5.67(−9)	≤ 7.63(−10)	≤ 3.42(−9)	≤ 2.46(−9)	≤ 3.47(−9)
H ₂ ¹³ CO ⁽²⁾	1.75 \pm 0.25(−9)	1.02 \pm 0.07(−9)	1.70 \pm 0.15(−9)	1.37 \pm 0.14(−9)	4.64 \pm 0.60(−11)	6.92 \pm 0.23(−10)	2.87 \pm 0.13(−10)	1.49 \pm 0.04(−9)
CH ₃ OH	2.12 ± 0.94(−7)	1.76 ± 0.74(−7)	4.00 ± 1.57(−7)	4.29 ± 2.29(−7)	4.52 \pm 0.47(−9)	6.54 \pm 0.52(−8)	3.11 \pm 0.29(−8)	1.79 \pm 0.08(−7)

Notes: 1. “*” mark the tentative detected molecules.

2. Species except for those marked with “†” are assumed to have the same temperature (listed in the table head) in the same substructure.

3. Values and uncertainties in bold face are obtained directly from the rotation diagram fittings in Figure 9.

4. For the species whose transitions are not sufficient to derive the rotation diagrams, their column densities are obtained from one strongest transition by assuming LTE with the excitation temperatures list in the table head (derived from HCOOCH₃ for HC, mm2, mm3a, and mm3b).

5. Values of H₂¹³CO⁽²⁾ are derived from the temperatures the same as CH₃OH list in Table 3.

6. Values of all species in the outflow regions (NE, SR, OFIN, and OFIS) are derived from the temperatures the same as CH₃CN at NE.

7. Uncertainties for the values derived from one transition (written as the subscript) are determined from T_{rot}, partition function Q(T_{rot}), and fitting to $\int T_B(\nu) d\nu$.

8. For species which are not detected, an upper limit derived from 3σ rms is given.

9. “+” mark the values which are likely obtained from optically thick lines and for those we did the optical depth correction.

Table A6: Column densities and abundances for N-bearing molecules from different substructures in Orion-KL denoted in Figure 4 and 5.

Species	HC (155 ± 16 K)	HC (121 ± 16 K)	mm2 (108 ± 4 K)	mm3a (103 ± 3 K)	mm3b (88 ± 6 K)	NE (43 ± 3 K)	SR (43 ± 3 K)	OFIN (43 ± 3 K)	OFIS (43 ± 3 K)
I. Column densities (in the form of $x \pm y(z) = (x \pm y) \times 10^z \text{ cm}^{-2}$)									
HC ₃ N($v_7 = 1$)	6.81 \pm 1.81(15)	1.22 \pm 0.67(16)	5.20 \pm 0.96(15)	2.36 \pm 0.54(15)	3.13 \pm 1.56(15)	\leq 9.13(15)	\leq 8.67(15)	\leq 6.79(15)	\leq 1.10(16)
CH ₃ CN	1.38\pm0.48(17) †	—	3.08\pm0.50(16) †	2.22\pm0.29(16) †	3.24\pm1.00(16) †	2.16\pm0.75(15) †	\leq 3.65(14)	\leq 7.79(14)	\leq 2.42(16)
CH ₃ ¹³ CN	—	9.42\pm4.50(14)	4.66 \pm 0.24(14)	3.16 \pm 0.18(14)	3.88 \pm 0.15(14)	3.53 \pm 0.78(13)	\leq 2.17(12)	\leq 4.42(12)	\leq 1.86(12)
CH ₂ CHCN	2.91 \pm 0.21(15)	2.40 \pm 0.10(15)	3.11 \pm 0.40(14)	\leq 1.29(13)	\leq 2.01(13)	\leq 3.19(13)	\leq 1.97(13)	\leq 8.13(12)	\leq 4.05(13)
CH ₃ CH ₂ CN	1.15 \pm 0.04(16)	1.05 \pm 0.01(16)	3.88 \pm 0.08(15)	1.09 \pm 0.08(15)	2.19 \pm 0.20(15)	\leq 4.26(13)	\leq 4.59(13)	\leq 5.10(13)	\leq 4.41(13)
HC ₇ N *	8.25 \pm 1.50(15)	5.83 \pm 18.30(16)	\leq 2.10(16)	\leq 2.24(16)	\leq 2.62(17)	\leq 5.28(22)	\leq 8.12(22)	\leq 5.58(22)	\leq 1.06(23)
HNCO	1.19\pm0.87(16) #	—	2.83\pm1.37(15) #	2.15\pm1.49(15) #	2.54\pm1.50(15) #	3.82 \pm 0.15(14)	2.84 \pm 0.44(13)	1.63 \pm 0.04(14)	2.36 \pm 0.05(14)
II. Abundances (in the form of $x \pm y(z) = (x \pm y) \times 10^z$)									
HC ₃ N($v_7 = 1$)	5.69 \pm 1.96(−9)	1.02 \pm 0.66(−8)	5.58 \pm 1.12(−9)	3.79 \pm 0.92(−9)	4.70 \pm 2.40(−9)	\leq 2.77(−8)	\leq 8.52(−8)	\leq 6.21(−8)	\leq 1.90(−7)
CH ₃ CN	1.16\pm0.50(−7) †	—	3.31\pm0.60(−8) †	3.56\pm0.52(−8) †	4.88\pm1.54(−8) †	6.54\pm2.42(−9) †	\leq 3.59(−9)	\leq 7.13(−9)	\leq 4.17(−9)
CH ₃ ¹³ CN	—	7.87\pm4.48(−10)	5.00 \pm 0.33(−10)	5.07 \pm 0.36(−10)	5.84 \pm 0.27(−10)	1.07 \pm 0.26(−10)	\leq 2.13(−11)	\leq 4.04(−11)	\leq 3.21(−11)
CH ₂ CHCN	2.43 \pm 0.34(−9)	2.01 \pm 0.21(−9)	3.34 \pm 0.48(−10)	\leq 2.07(−11)	\leq 3.02(−11)	\leq 9.68(−11)	\leq 1.94(−10)	\leq 7.44(−11)	\leq 6.99(−10)
CH ₃ CH ₂ CN	9.59 \pm 0.97(−9)	8.77 \pm 0.63(−9)	4.16 \pm 0.15(−9)	1.75 \pm 0.14(−9)	3.29 \pm 0.33(−9)	\leq 1.29(−10)	\leq 4.51(−10)	\leq 4.67(−10)	\leq 7.61(−10)
HC ₇ N *	6.89 \pm 10.60(−9)	4.87 \pm 16.50(−8)	\leq 2.25(−8)	\leq 3.60(−8)	\leq 3.94(−7)	\leq 1.60(−1)	\leq 7.98(−1)	\leq 5.10(−1)	\leq 18.30(−1)
HNCO	9.93\pm8.33(−9) #	—	3.04\pm1.53(−9) #	3.46\pm2.47(−9) #	3.83\pm2.30(−9) #	1.16 \pm 0.07(−9)	2.79 \pm 0.51(−10)	1.49 \pm 0.06(−9)	4.07 \pm 0.10(−9)

Notes: 1. “*” marks the tentative detected molecule.

2. Species except for those marked with “†” are assumed to have the same temperature (listed in the table head) in the same substructure.

3. Values and uncertainties in bold face are obtained directly from the rotation diagram fittings in Figures 8 and 9.

4. For the species whose transitions are not sufficient to derive the rotation diagrams, their column densities are obtained from one strongest transition by assuming LTE with the excitation temperatures list in the table head (derived from CH₃CN for HC, mm2, mm3a and mm3b).5. Values of all species in the outflow regions (NE, SR, OFIN, and OFIS) are derived from the temperatures the same as CH₃CN at NE.6. Uncertainties for the values derived from one transition (written as the subscript) are determined from T_{rot} , partition function $Q(T_{\text{rot}})$, and fitting to $\int T_{\text{B}}(\nu) d\nu$.7. For species which are not detected, an upper limit derived from 3σ rms is given.

8. “†” mark the values which are likely obtained from optically thick lines and for those we did the optical depth correction.

Table A7: Column densities and abundances for S-bearing molecules from different substructures in Orion-KL denoted in Figure 4.

Species	HC (199 ± 45 K)	mm2 (173 ± 40 K)	mm3a (101 ± 26 K)	(89 ± 24 K)	mm3b (193 ± 42 K)	NE (43 ± 3 K)	SR (43 ± 3 K)	OFIN (43 ± 3 K)	OFIS (43 ± 3 K)
I. Column densities (in the form of $x \pm y(z) = (x \pm y) \times 10^2 \text{ cm}^{-2}$)									
OCS	$1.69_{\pm 0.11}(17)$	$1.35_{\pm 0.05}(17)$	$9.02_{\pm 1.00}(16)$	$1.73_{\pm 0.36}(17)$	$1.92_{\pm 0.08}(17)$	$\leq 1.08(16)$	$\leq 8.26(15)$	$\leq 2.08(15)$	—
O ¹³ CS	$2.12_{\pm 0.12}(15)$	$1.66_{\pm 0.02}(15)$	$1.13_{\pm 0.17}(15)$	$2.22_{\pm 0.46}(15)$	$2.46_{\pm 0.10}(15)$	$\leq 5.53(13)$	$\leq 6.81(13)$	$\leq 2.06(13)$	$\leq 2.73(13)$
SO ₂	$4.16_{\pm 0.78}(17)$	$2.79_{\pm 0.43}(17)$	$1.09_{\pm 0.00}(17)$	$1.47_{\pm 0.09}(17)$	$2.28_{\pm 0.38}(17)$	$7.03_{\pm 0.81}(16)$	$\leq 4.26(14)$	$\leq 3.29(14)$	$\leq 3.82(14)$
³⁴ SO ₂	$5.00 \pm 3.82(16)$	$2.84 \pm 2.51(16)$	$8.67 \pm 6.00(15)$	$1.25 \pm 0.61(16)$	$8.62 \pm 6.64(15)$	$2.55_{\pm 0.05}(15)$	$\leq 2.91(13)$	$\leq 1.70(13)$	$\leq 1.03(13)$
SO	$8.20_{\pm 1.53}(16)$	$7.16_{\pm 1.29}(16)$	$3.13_{\pm 0.55}(16)$	$4.86_{\pm 0.48}(16)$	$3.79_{\pm 0.63}(16)$	$2.26_{\pm 0.03}(16)$	$1.32_{\pm 0.02}(15)$	$6.31_{\pm 0.09}(15)$	$9.18_{\pm 0.26}(14)$
¹³ CS	$8.69_{\pm 1.49}(14)$	$4.72_{\pm 0.78}(14)$	$3.49_{\pm 0.53}(14)$	$5.30_{\pm 0.48}(14)$	$2.77_{\pm 0.30}(14)$	$1.99_{\pm 0.12}(13)$	$4.80_{\pm 0.05}(13)$	$9.61_{\pm 0.98}(12)$	$\leq 1.61(12)$
II. Abundances (in the form of $x \pm y(z) = (x \pm y) \times 10^2$)									
OCS	$1.41_{\pm 0.18}(-7)$	$1.45_{\pm 0.07}(-7)$	$1.45_{\pm 0.18}(-7)$	$1.58_{\pm 0.06}(-7)$	$2.61_{\pm 0.56}(-7)$	$\leq 3.27(-8)$	$\leq 8.12(-8)$	$\leq 1.90(-8)$	—
O ¹³ CS	$1.77_{\pm 0.22}(-9)$	$1.78_{\pm 0.04}(-9)$	$1.81_{\pm 0.30}(-9)$	$1.98_{\pm 0.05}(-9)$	$3.34_{\pm 0.72}(-9)$	$\leq 1.68(-10)$	$\leq 6.69(-10)$	$\leq 1.88(-10)$	$\leq 4.72(-10)$
SO ₂	$3.47_{\pm 0.91}(-7)$	$2.99_{\pm 0.51}(-7)$	$1.76_{\pm 0.02}(-7)$	$2.44_{\pm 0.22}(-7)$	$2.21_{\pm 0.15}(-7)$	$2.13_{\pm 0.29}(-7)$	$\leq 4.19(-9)$	$\leq 3.01(-9)$	$\leq 6.58(-9)$
³⁴ SO ₂	$4.18 \pm 3.65(-8)$	$3.04 \pm 2.78(-8)$	$1.39 \pm 0.99(-8)$	$2.01 \pm 1.01(-8)$	$1.30 \pm 1.01(-8)$	$7.75_{\pm 0.29}(-9)$	$\leq 2.86(-10)$	$\leq 1.55(-10)$	$\leq 1.78(-10)$
SO	$6.85_{\pm 1.79}(-8)$	$7.69_{\pm 1.51}(-8)$	$5.04_{\pm 0.95}(-8)$	$7.81_{\pm 0.88}(-8)$	$5.71_{\pm 1.00}(-8)$	$6.87_{\pm 0.21}(-8)$	$1.30_{\pm 0.05}(-8)$	$5.77_{\pm 0.19}(-8)$	$1.58_{\pm 0.05}(-8)$
¹³ CS	$7.26_{\pm 1.77}(-10)$	$5.06_{\pm 0.92}(-10)$	$5.62_{\pm 0.92}(-10)$	$8.51_{\pm 0.88}(-10)$	$4.16_{\pm 0.49}(-10)$	$6.03_{\pm 0.48}(-11)$	$4.71_{\pm 0.16}(-10)$	$8.80_{\pm 1.06}(-11)$	$\leq 2.78(-11)$

Notes: 1. Values and uncertainties in bold face are obtained directly from the rotation diagram fittings in Figure 9.

2. Values in italic font are derived from upper limit of T_{rot} in mm3a and mm3b.

3. For the species whose transitions are not sufficient to derive the rotation diagrams, their column densities are obtained from one strongest transition by assuming LTE with the excitation temperatures list in the table head (derived from ³⁴SO₂ for HC, mm2, mm3a and mm3b).

4. Values of all species in the outflow regions (NE, SR, OFIN, and OFIS) are derived from the temperatures the same as CH₃CN at NE.

5. Uncertainties for the values derived from one transition (written as the subscript) are determined from T_{rot} , partition function $Q(T_{\text{rot}})$, and fitting to $\int T_{\text{B}}(\nu) d\nu$.

6. For species which are not detected, an upper limit derived from 3σ rms is given.

7. “+” mark the values which are likely obtained from optically thick lines and for those we did the optical depth correction.

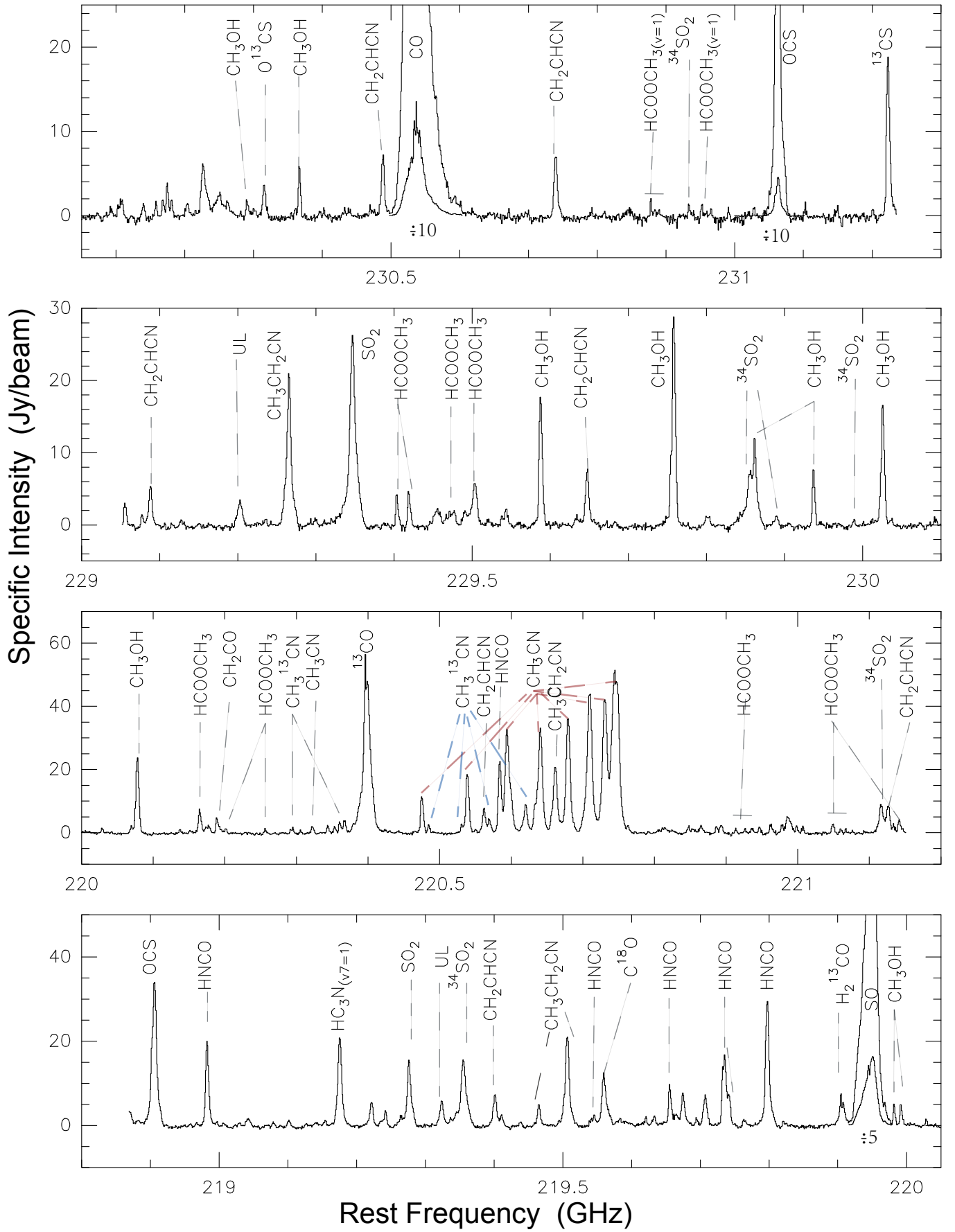
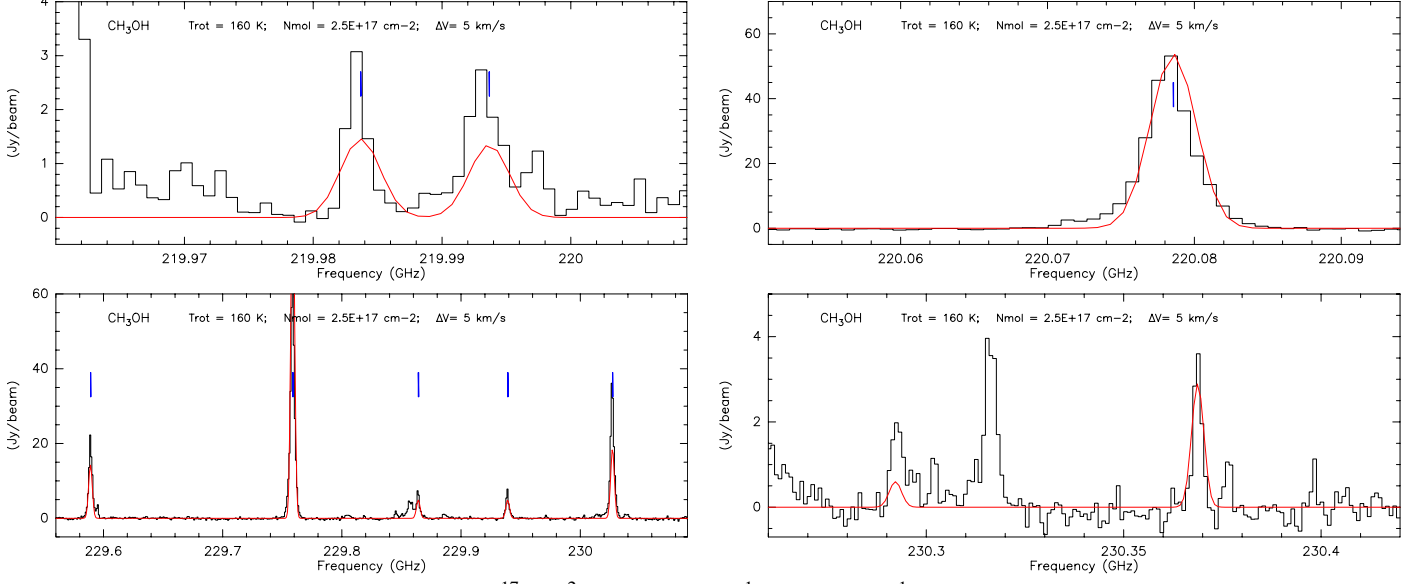


Fig. A1: Spectrum from the HC, with identified strong lines marked. From 220.5 GHz to 220.8 GHz, CH_3CN and $\text{CH}_3^{13}\text{CN}$ are labelled in red and blue, respectively. COMs containing only C, H, O elements and other tentative detections are labelled in Figure A2.

CH₃OH @ mm3a ($T_{\text{rot}}=160$ K; $N_{\text{mol}} = 2.5 \times 10^{17} \text{ cm}^{-2}$; $V_{\text{lsr}} = 7.6 \text{ km s}^{-1}$; $\Delta V = 5 \text{ km s}^{-1}$)



HCOOCH₃ @ mm3b ($T_{\text{rot}}=102$ K; $N_{\text{mol}} = 1.0 \times 10^{17} \text{ cm}^{-2}$; $V_{\text{lsr}} = 7.8 \text{ km s}^{-1}$; $\Delta V = 3 \text{ km s}^{-1}$)

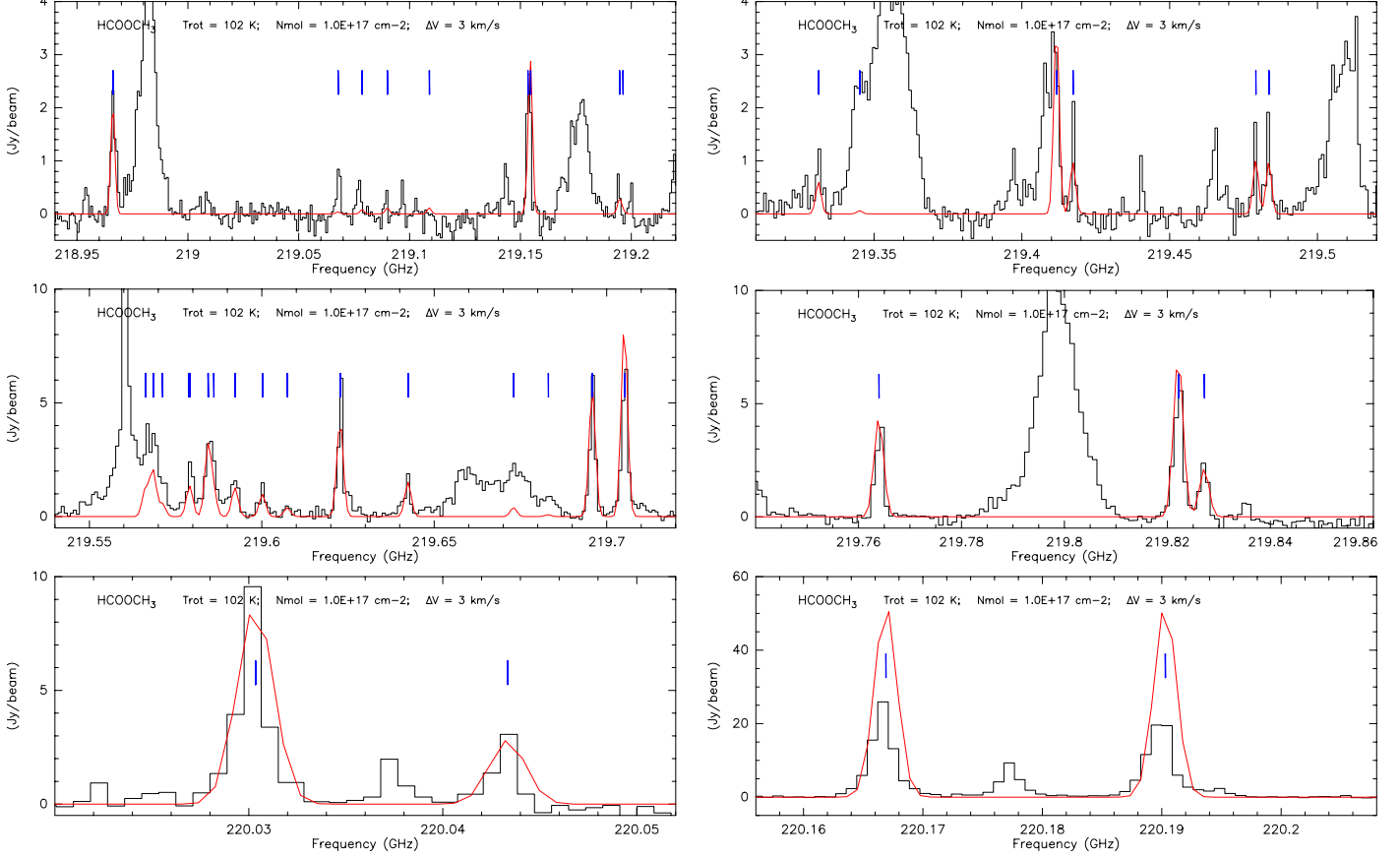


Fig. A2: Synthetic spectrum fitting of COMs towards their emission peaks (V_{lsr} of each species are corrected according to V_{peak} from Figure A3). The black histograms are the observed spectra, overlaid with a best fit model spectrum for given uniform FWHM linewidth (ΔV) (fit from Figure A3), T_{rot} (assumed from an adjacent substructure), and N_{mol} (adjusted based on N_{T} in Tables A5I, A6I, and A7I) listed on top of each panel. Blue line mark the central frequency of each transition. Uncertainties of the fitting to observations come from the assumption that under LTE, the candidate molecule lines are optically thin, and each species has the same line width at different transitions. Referenced molecular data are from CDMS/JPL (Sanchez-Monge 2011; Palau et al. 2011).

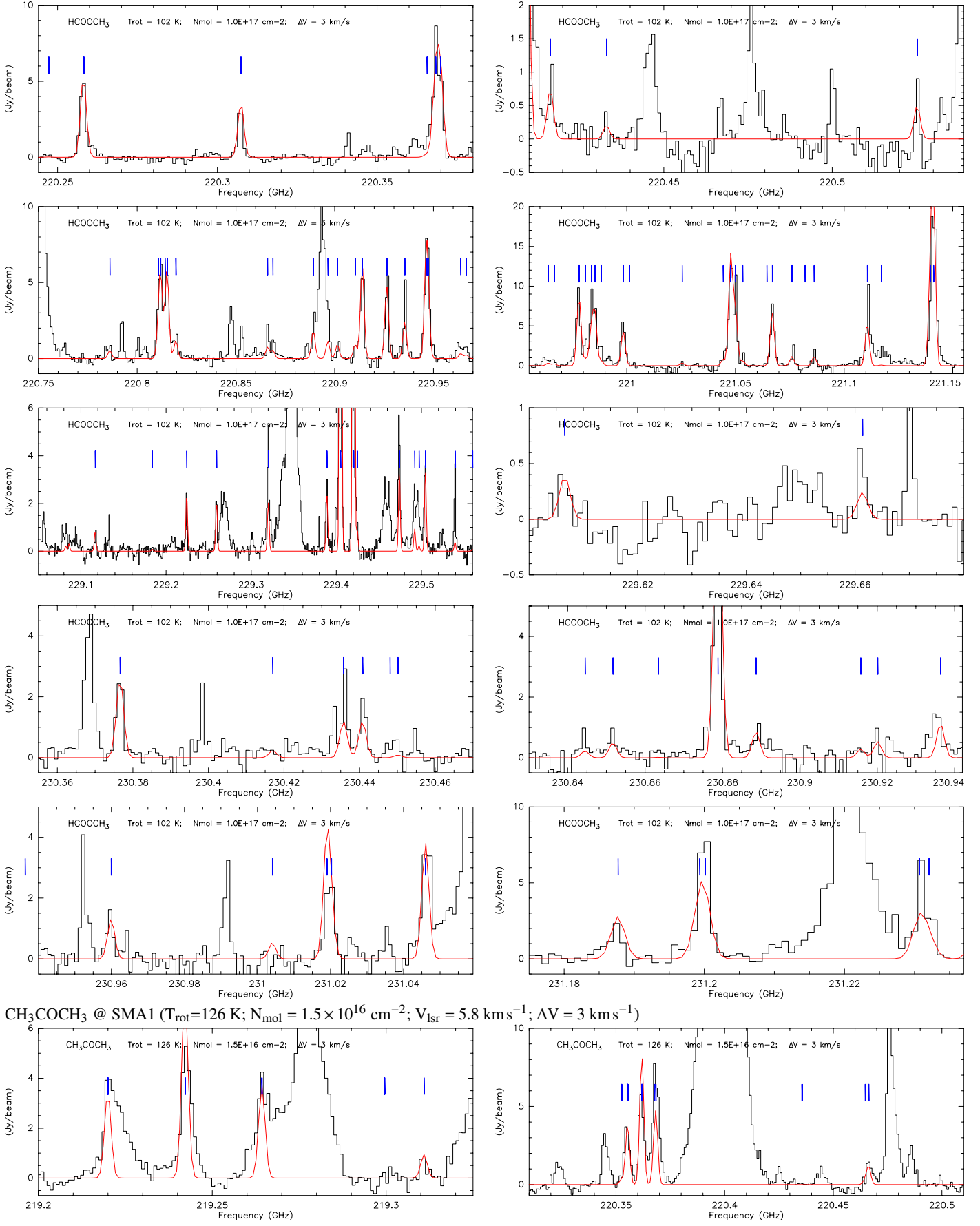


Fig. A2: (continued)

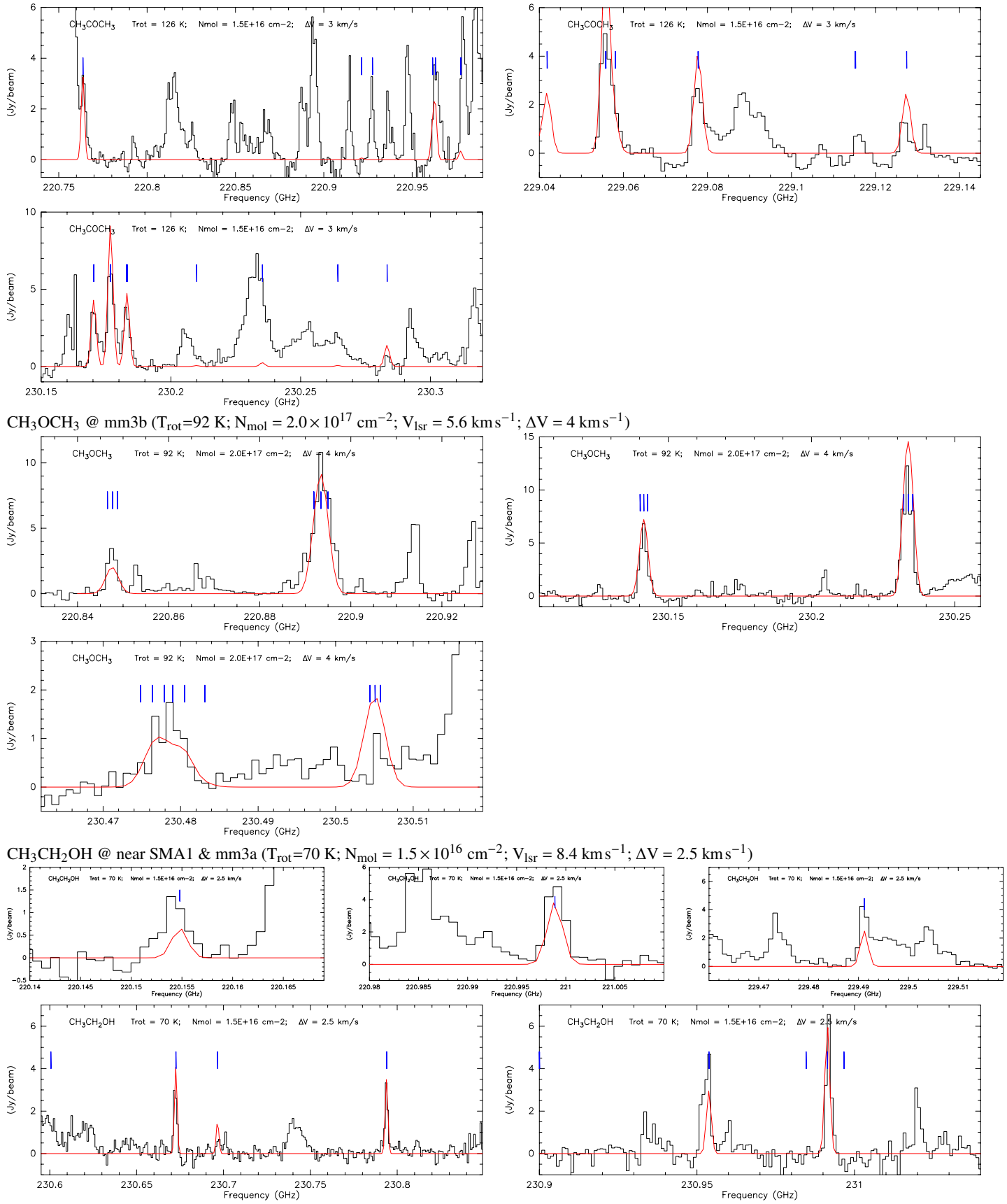
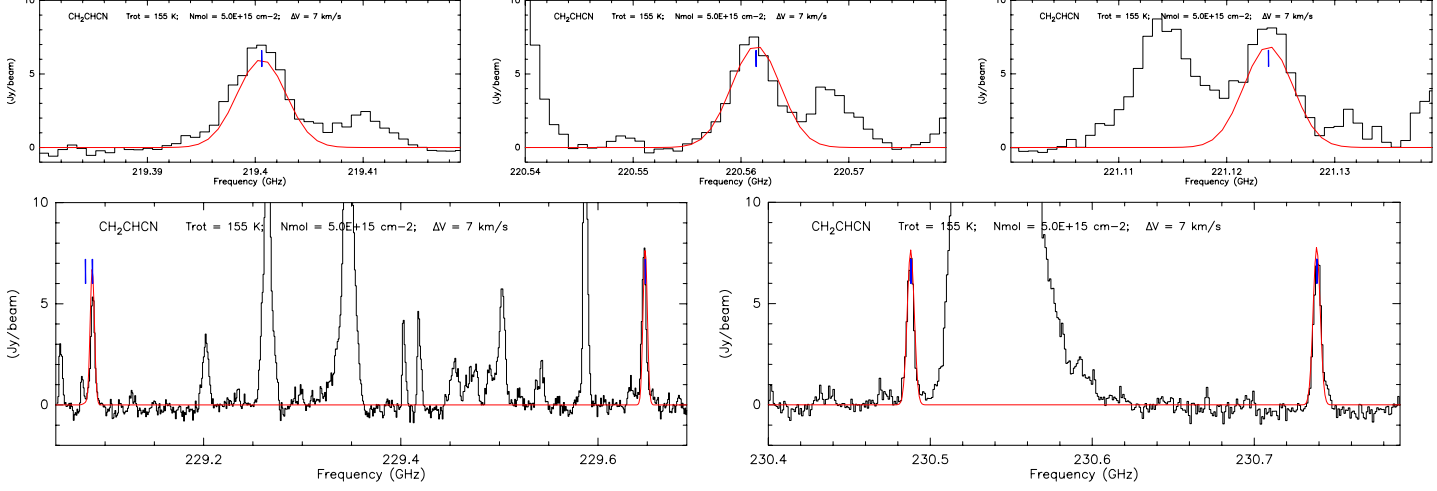
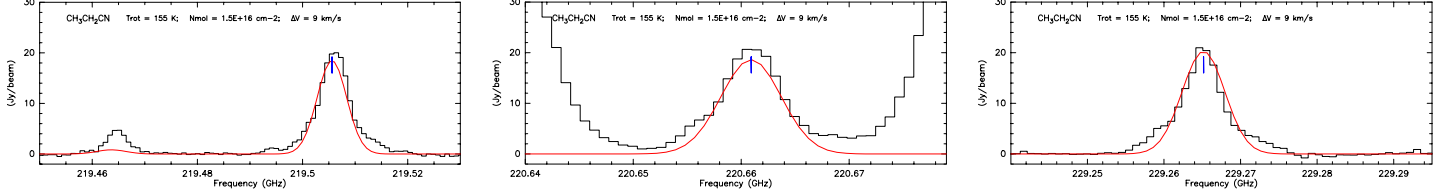


Fig. A2: (continued)

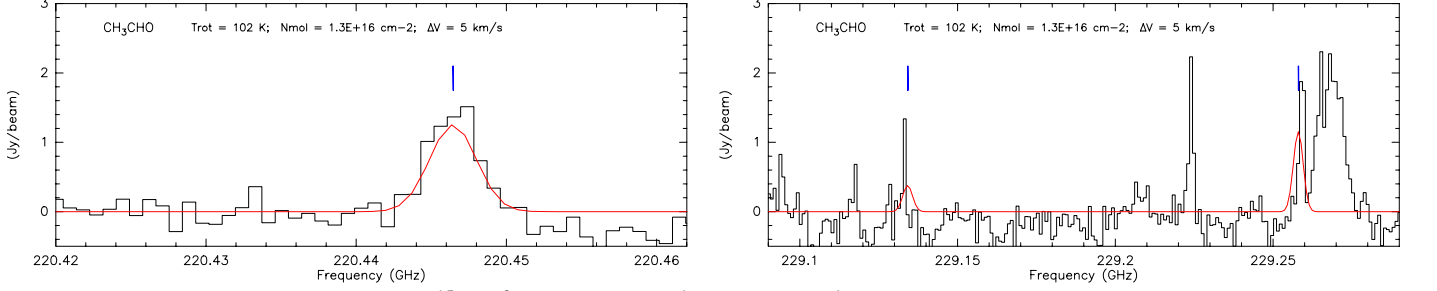
CH₂CHCN @ North to hotcore ($T_{\text{rot}}=155$ K; $N_{\text{mol}} = 5.0 \times 10^{15} \text{ cm}^{-2}$; $V_{\text{lsr}} = 4.9 \text{ km s}^{-1}$; $\Delta V = 7 \text{ km s}^{-1}$)



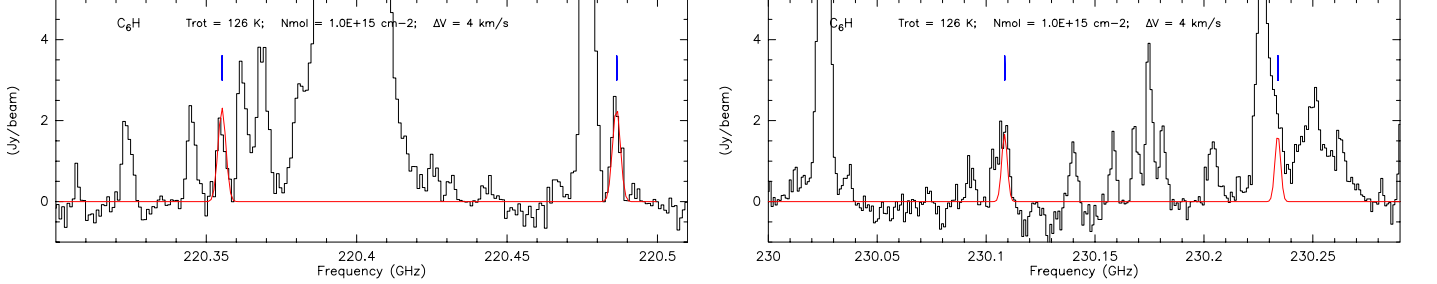
CH₃CH₂CN @ hotcore ($T_{\text{rot}}=155$ K; $N_{\text{mol}} = 1.5 \times 10^{16} \text{ cm}^{-2}$; $V_{\text{lsr}} = 5.1 \text{ km s}^{-1}$; $\Delta V = 9 \text{ km s}^{-1}$)



CH₃CHO @ mm3b ($T_{\text{rot}}=102$ K; $N_{\text{mol}} = 1.3 \times 10^{16} \text{ cm}^{-2}$; $V_{\text{lsr}} = 8.0 \text{ km s}^{-1}$; $\Delta V = 5 \text{ km s}^{-1}$)



C₆H @ SMA1 ($T_{\text{rot}}=126$ K; $N_{\text{mol}} = 1.0 \times 10^{15} \text{ cm}^{-2}$; $V_{\text{lsr}} = 4.0 \text{ km s}^{-1}$; $\Delta V = 4 \text{ km s}^{-1}$)



HC₇N @ North to hotcore ($T_{\text{rot}}=155$ K; $N_{\text{mol}} = 1.0 \times 10^{16} \text{ cm}^{-2}$; $V_{\text{lsr}} = 6.3 \text{ km s}^{-1}$; $\Delta V = 5 \text{ km s}^{-1}$)

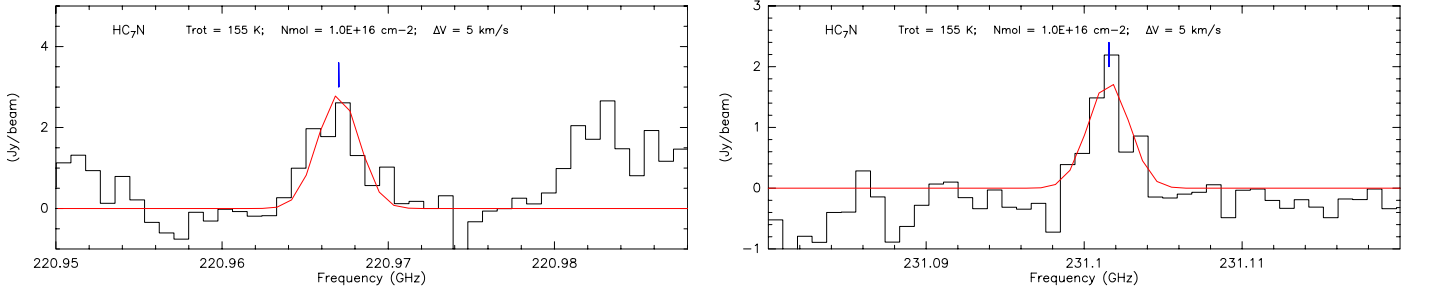


Fig. A2: (continued)

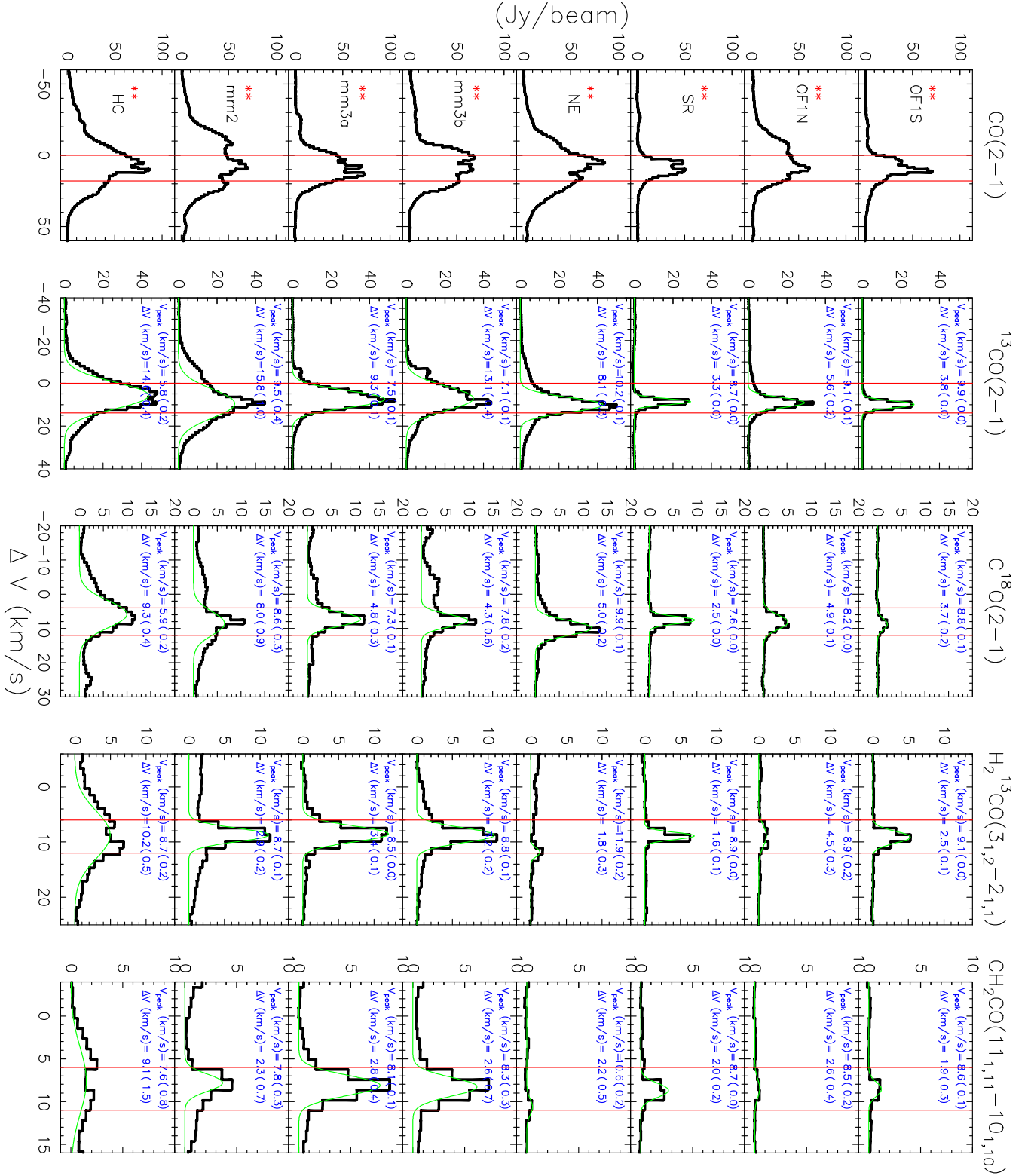
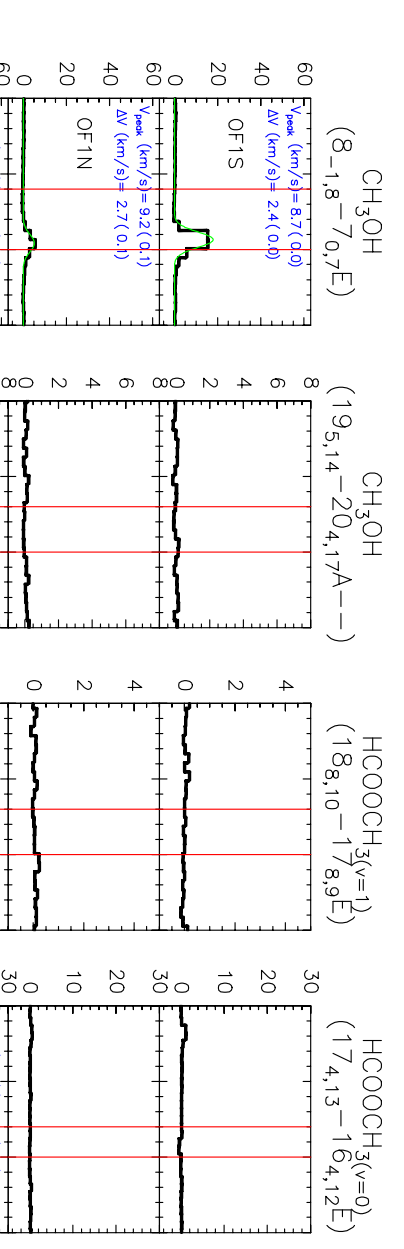


Fig. A3: Line profiles of identified species from each continuum peak. In measuring the main V_{peak} and ΔV of each line at each substructure, lines in green and notes in blue (in the form of “value(error)”) are given by the Gaussian fittings using Gildas software. Multi-Gaussian fittings are used to CH_3CN , $\text{CH}_3^{13}\text{CN}$, HCOOCH_3 ($v=0$), and CH_3COCH_3 due to blending, and to SO_2 , $^{34}\text{SO}_2$, and SO due to the second velocity component (the second velocity component of HNCO measured from multi-Gaussian fittings are given in Figure 7). Single Gaussian fittings are used to the rest lines, while lines whose V_{peak} cannot be measured by Gaussian fittings owing to strong self-absorption are marked with “**”, and non-detections are not marked. Two red vertical lines in each panel mark the velocity range over which the emission from each species is integrated to make the distribution maps shown in Figures 4 and 5.



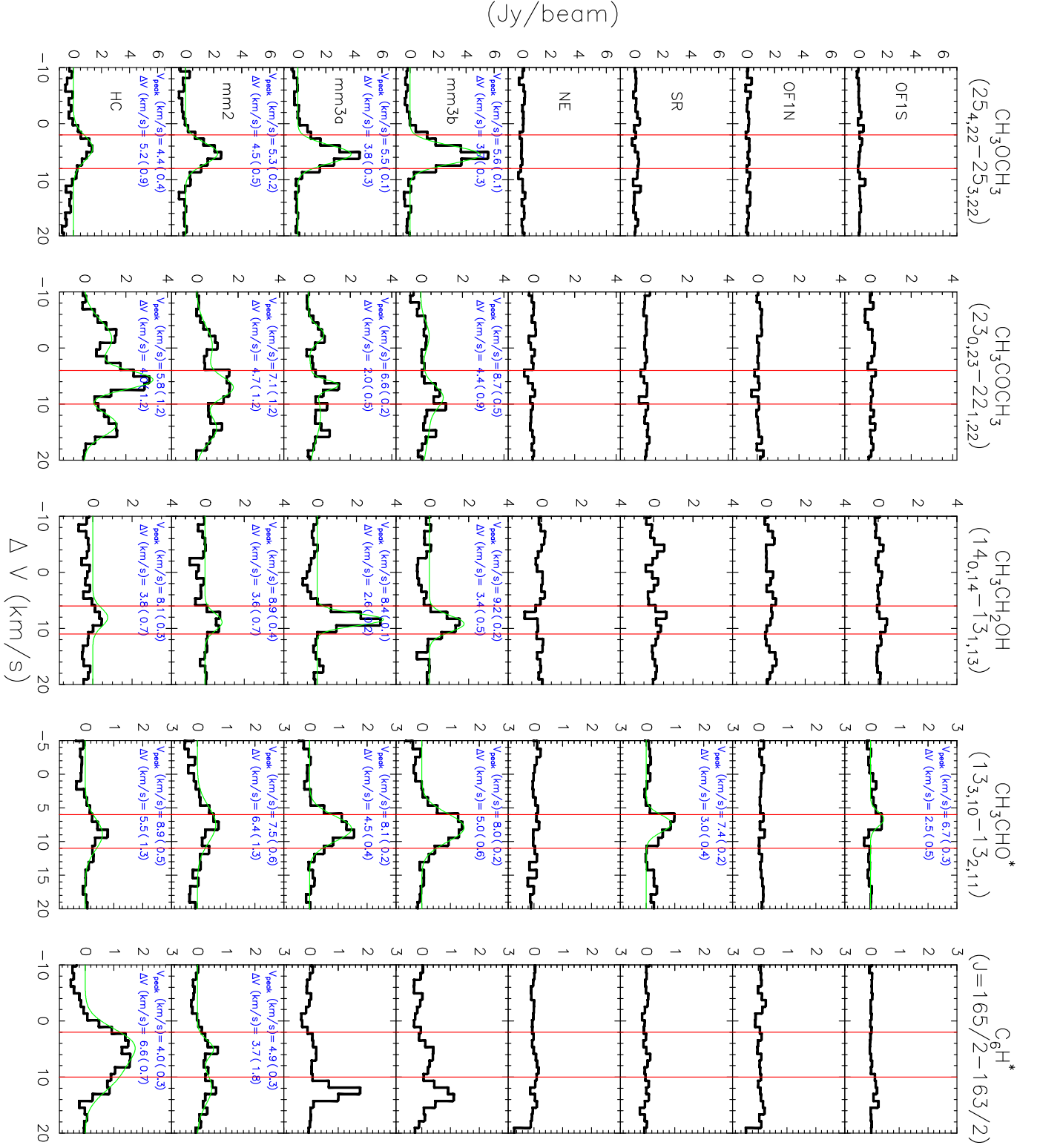


Fig. A3: (continued)

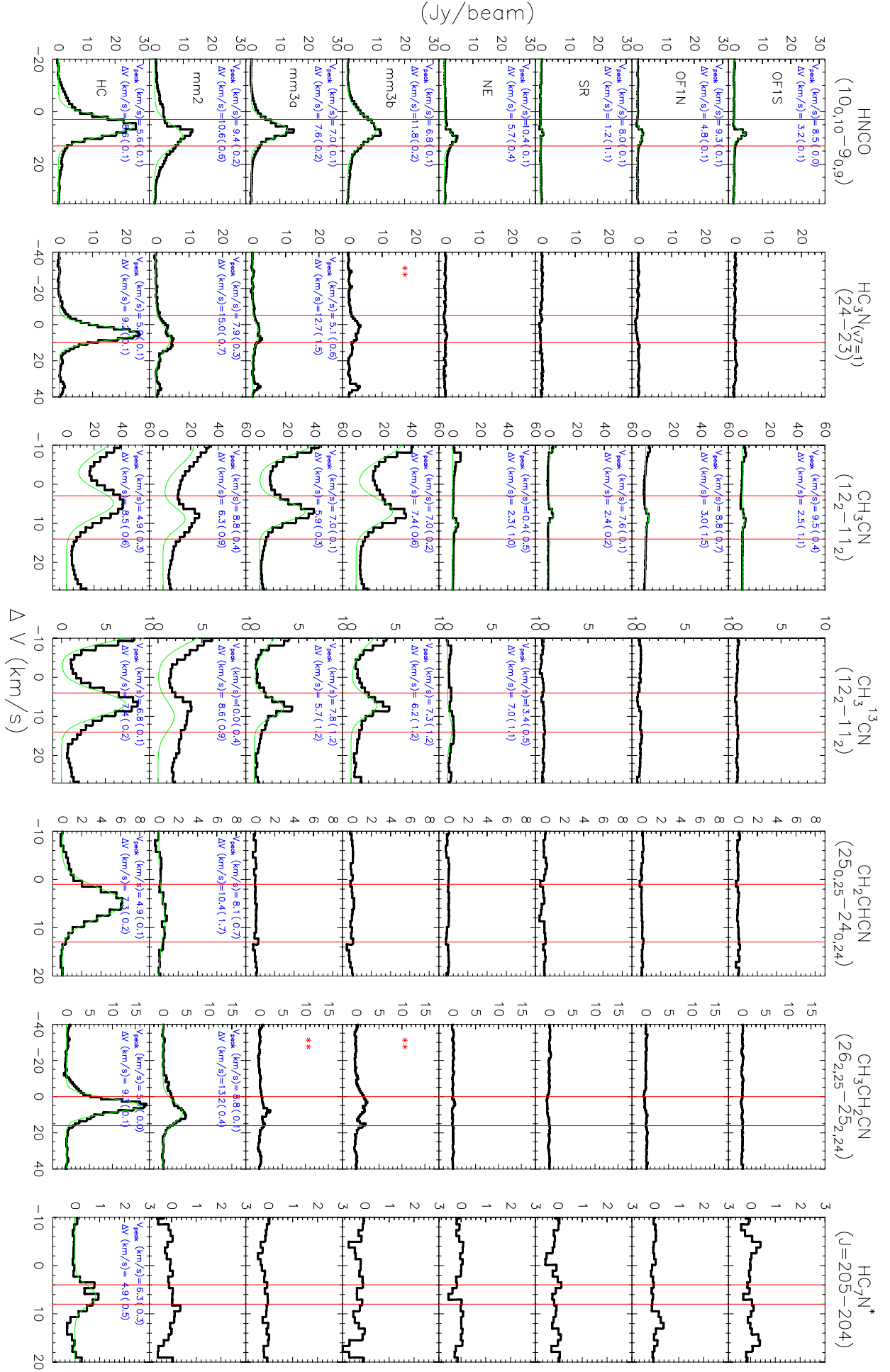


Fig. A3: (continued)

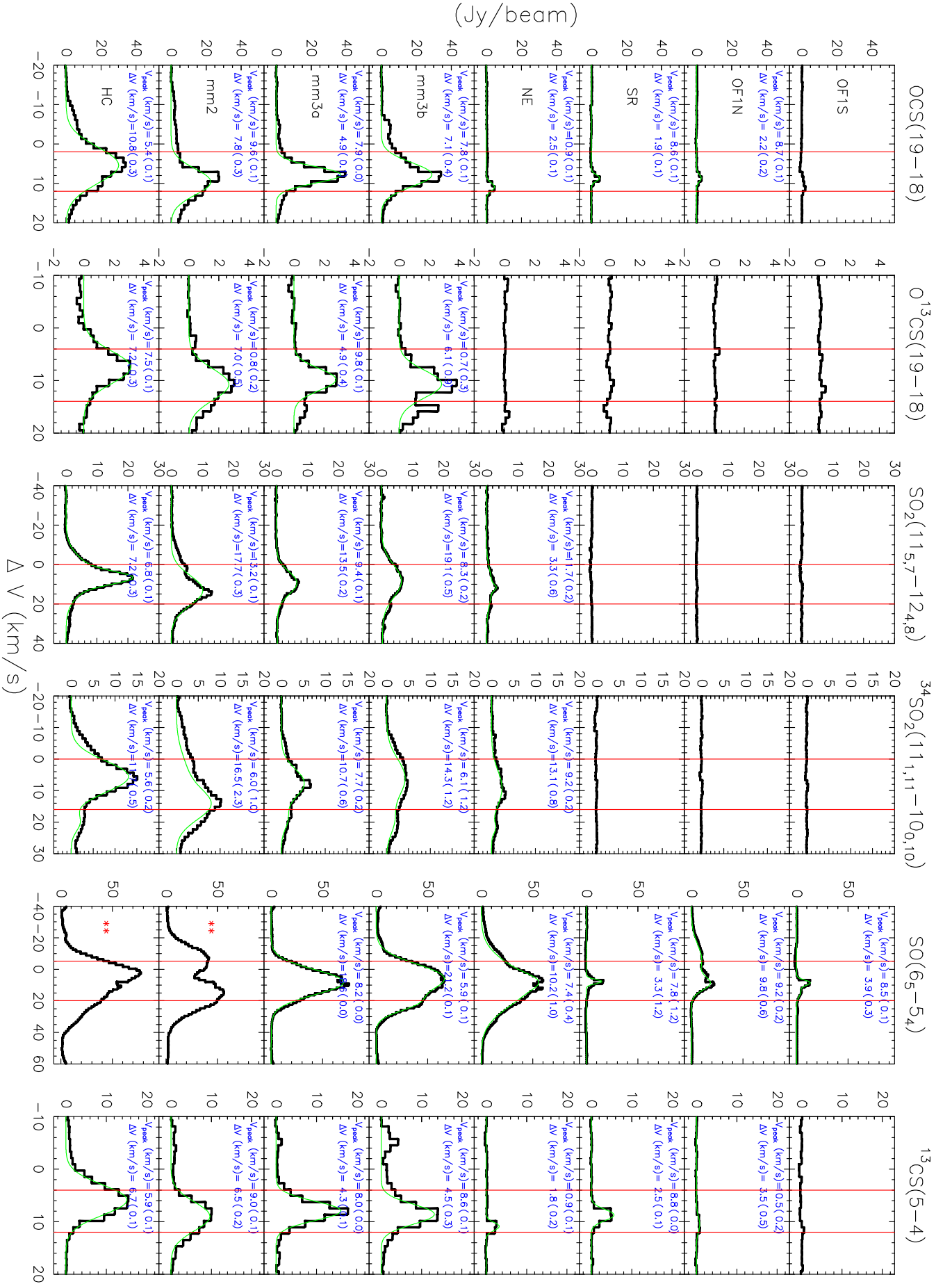


Fig. A3: (continued)

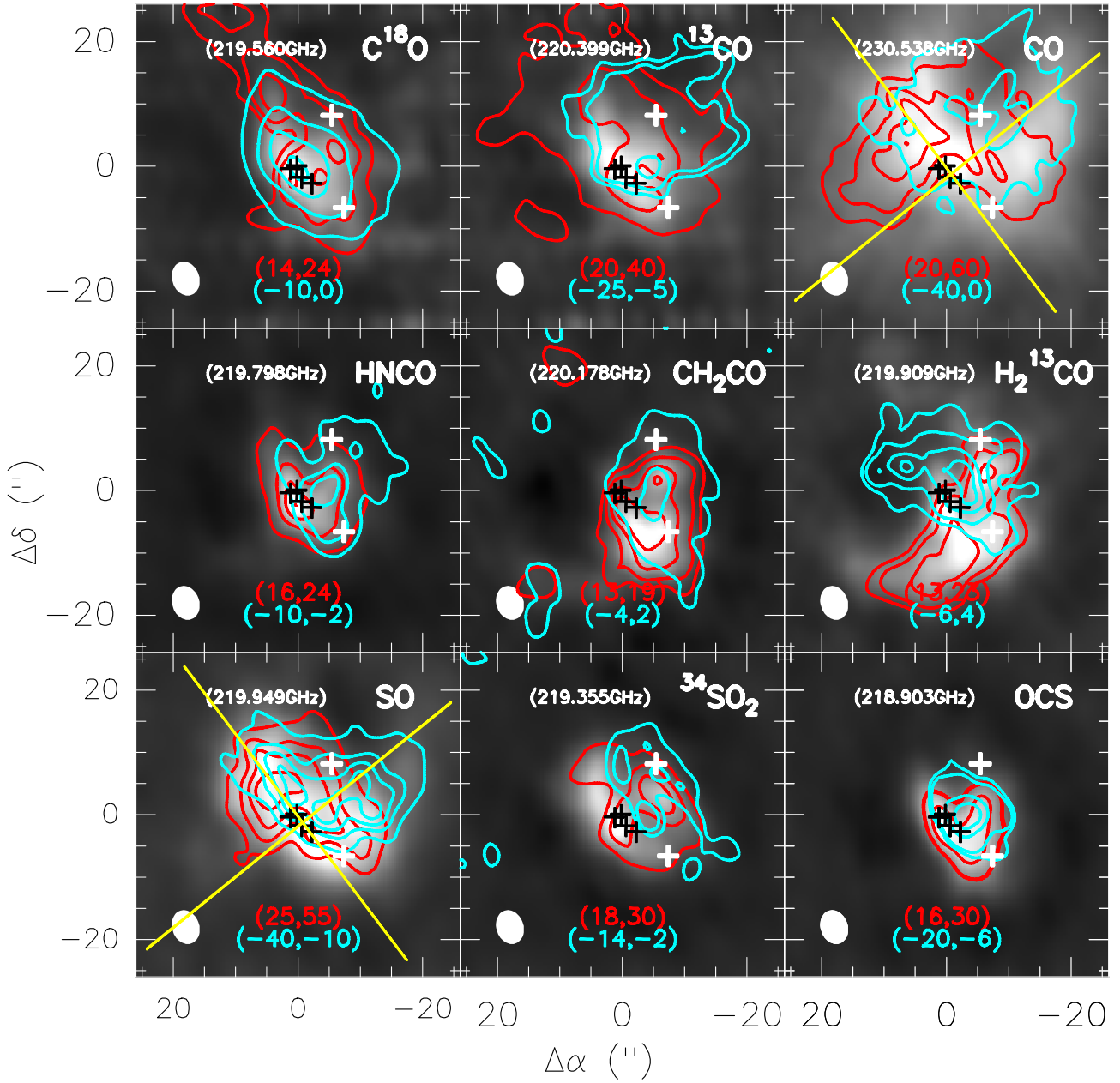


Fig. A4: Line wing flux integration maps from the combined SMA-30 m data at 1.3 mm. The grey maps show the intensity integrated ranging through the main emission of their linewidth in Figure A3. Red and blue contours show the red-shifted and blue-shifted gas, with the intensity integrated as labelled. Yellow lines sketch the outflow directions. Black crosses denote the hotcore, SMA1, Source I, and Source N; white crosses denote the BN object and CR.

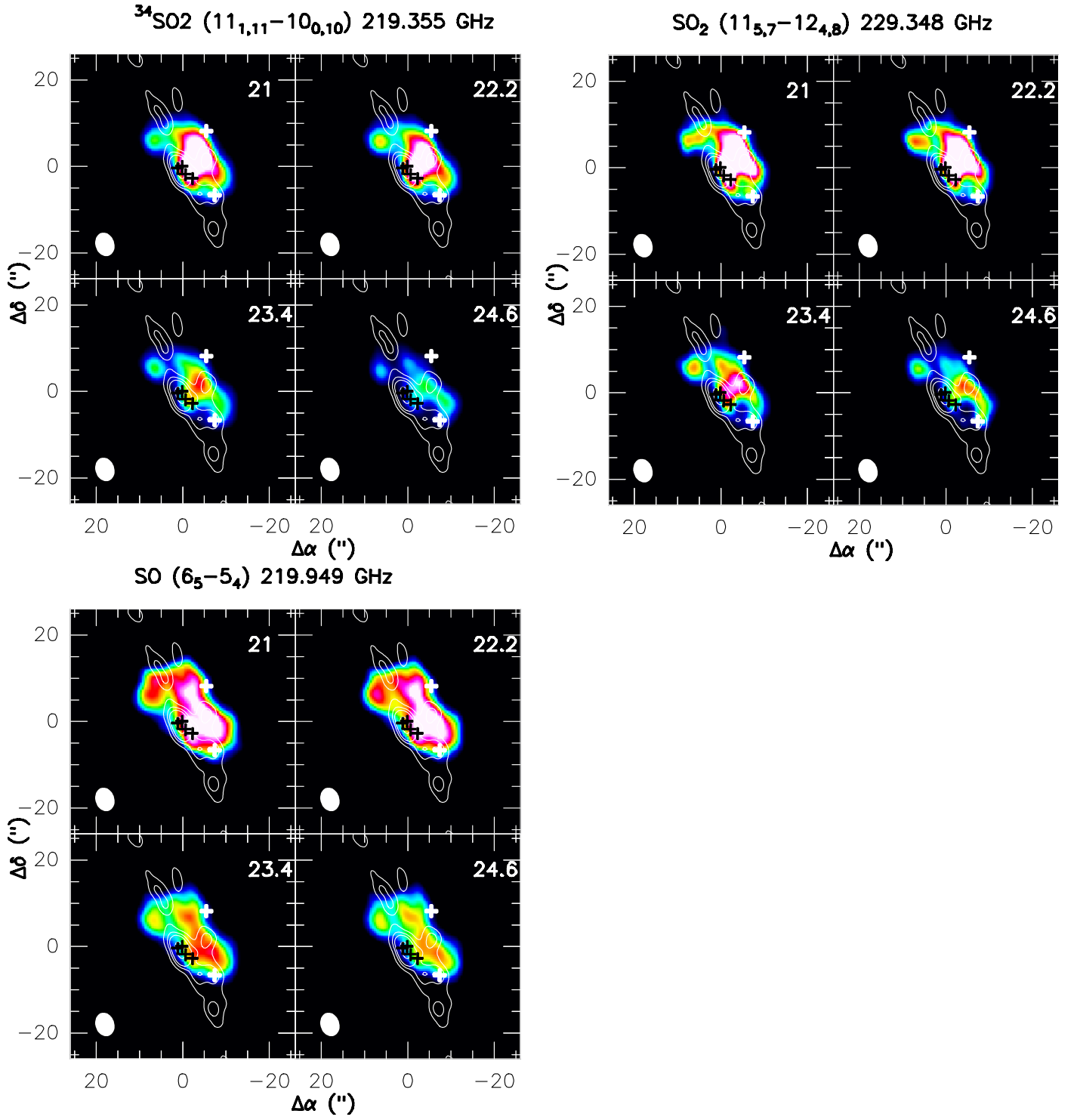


Fig. A5: Channel maps of the second velocity component ($V_{\text{peak}} \sim 22 \text{ km s}^{-1}$) of the strongest unblended $^{34}\text{SO}_2$ and SO_2 line, as well as of $\text{SO}(6_5 \rightarrow 5_4)$.

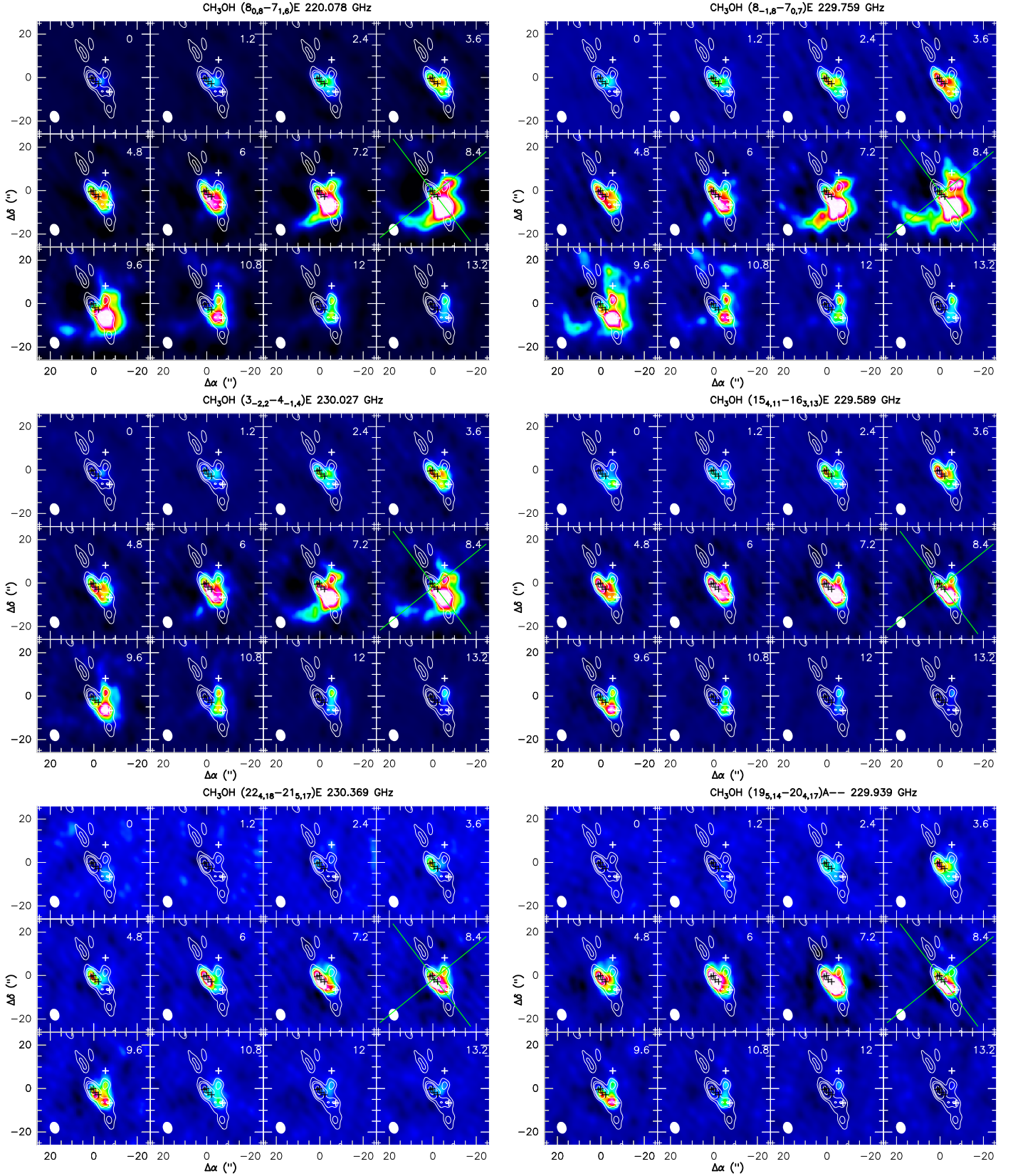


Fig. A6: Channel maps of unblended CH_3OH lines show multiple velocity-dependent emission peaks: $2.4 - 3.6 \text{ km s}^{-1}$ towards SMA1, $\sim 4.8 - 6 \text{ km s}^{-1}$ towards HC, $7.2 - 9.6 \text{ km s}^{-1}$ towards HC/mm3a/mm3b, 10.8 km s^{-1} towards mm3a/mm3b/mm2 and $> 12 \text{ km s}^{-1}$ towards mm2. Green lines sketch the outflow directions. Black crosses denote the hotcore, SMA1, Source I, and Source N; white crosses denote the BN object and the CR.